SPECTROSCOPIC CHARACTERIZATION OF EXOPLANETS: FROM LOUPE TO SINFONI

ISBN: 978-94-6295-791-6

Printed by ProefschriftMaken || www.proefschriftmaken.nl

SPECTROSCOPIC CHARACTERIZATION OF EXOPLANETS: FROM LOUPE TO SINFONI

Proefschrift

ter verkrijging van
de graad van Doctor aan de Universiteit Leiden,
op gezag van Rector Magnificus prof.mr. C.J.J.M. Stolker,
volgens besluit van het College voor Promoties
te verdedigen op donderdag 23 november 2017
klokke 11:15 uur

door

Herman Jens Hoeijmakers

geboren te Zwolle, Nederland
in 1990

Promotiecommissie:

Promotor:	Prof. dr. I.A.G. Snellen	
Co-promotor:	Dr. ir. F. Snik	
Overige leden:	Prof. dr. H. J. A. Röttgering	
	Prof. dr. C. U. Keller	
	Prof. dr. B. R. Brandl	
	Prof. dr. M. R. Hogerheijde	
	Dr. J. L. Birkby	University of Amsterdam
	Dr. C. Lovis	University of Geneva

To my mom, for her kindness, optimism,
endless love and immeasurable strength.

CONTENTS

1 INTRODUCTION

1.1 THE SEARCH FOR EXTRA-SOLAR PLANETS

1.1.1 *Introduction*

Speculations and ideas about the existence of planets in solar systems other than our own can be traced through the scientific and popular literature to decades before the discovery of the first extra-solar planets (*exoplanets*). The first discovery of a planetary mass object outside the solar system was made in 1992, orbiting the pulsar PSR1257+12 (Wolszczan et al., 1992). This object lives in the extreme radiation environment of the pulsar and is believed to have formed from the remnants of the debris disk that that may have formed after the supernova explosion of the progenitor star (Miller et al., 2001; Hansen et al., 2009; Kerr et al., 2015). The discovery of the first exoplanet around a main sequence star is attributed to Mayor et al. (1995), who discovered a planet orbiting around the sun-like star 51 Pegasi in 1995. This planet was discovered via the periodic motion of the star induced by the gravitational pull of the planet. Many times in astronomy, observations are biased towards the most extreme kinds of objects, which are discovered first because they are the easiest to detect. This is certainly true for the detection of the first exoplanets: 51 Pegasi b is a gas giant half as massive as Jupiter, but orbits its star at a distance of 0.052 AU, completing one revolution every 4.2 days (Mayor et al., 1995; Butler et al., 2006; Brogi et al., 2013; Birkby et al., 2017). This planet could be detected because its gravitational influence on the star is relatively large due to its small orbital distance. The gravitational interaction between the planet and the star also induces strong tidal forces that act to circularize the orbit of the planet and synchronize the axial (diurnal) rotation period with the orbital period. The likely consequence is that one hemisphere of the planet always faces the scorching radiation of the nearby star and is heated to temperatures of over 1000 Kelvin, while the other side of the planet perpetually faces towards outer space (Brogi et al., 2013). Clearly, this planet is unlike any of the planets in the solar system, which is why its unexpected discovery has had an enormous impact.

51 Pegasi b was the first of a new class of exoplanets that are nowadays referred to as *hot Jupiters* (see Figure 1.1). Via numerous exoplanet-finding surveys, many planets like it have been discovered since. However as surveys have become more sensitive to smaller and cooler planets, it has become clear that hot Jupiters actually form a small minority in a much larger, di-

verse exoplanet population. At the time of writing, over 3600 planets have been discovered and have been independently followed-up[1]. These planets occupy a broad parameter space, and include rocky planets as well as gas giants orbiting various types of stars over a wide range of orbital distances. Although this entire population has not yet fully been explored, there does not seem to be an indication that any system can be considered to be typical.

Theories of how planets form must explain this diversity in the exoplanet population, including extreme examples like hot Jupiters. 22 years after the discovery of the first exoplanets, the mechanism of planet formation is still not fully understood. Proposed planet formation theories broadly fall into three categories:

1. The core-accretion model (Pollack et al., 1996) describes the gradual coagulation of dust particles into a proto-planetary core, which gravitationally attracts more particles as it grows. When sufficiently massive, it rapidly accretes gas in a runaway fashion until the star-forming disk is cleared by the onset of nuclear fusion in the core of the newborn star.

2. The disk gravitational instability model (Boss, 1997) posits that planets may form from self-gravitating clumps of disk material that are created by dynamical instabilities in the disk.

3. The pre-stellar nebula may fragment into separate clumps at an early stage, in which planets may form in a similar way as binary stars albeit with extreme mass ratios (see e.g. Hennebelle et al., 2008).

It is possible that all these formation pathways take place in nature to some degree. Identifying the dominant formation process then requires the careful study of both planet-forming disks as well as exoplanets themselves, because the present-day state of an exoplanet may in part be determined by its formation scenario (Madhusudhan et al., 2014).

An important factor in all three formation pathways is *planet migration*: During the formative stages the orbit of the planet may evolve, causing it to migrate inwards or outwards. Migration may be caused by the interplay between the planet and the disk material in which it is formed, gravitational interactions with other planets in the system, tidal interactions with the star and stellar encounters (Rasio et al., 1996; Weidenschilling et al., 1996; Ward, 1997; Laughlin et al., 1998; Ida et al., 2000). If a planet retains its primordial atmosphere, its present-day chemical composition may be indicative of its formation environment and therefore shed light on its migration history (Öberg et al., 2011). The realization that planet migration is an important aspect of planet formation has also influenced the way we understand our own solar

1 Exoplanet.eu maintains a database of exoplanet discoveries and candidates (Schneider et al., 2011)

system. It is now suspected that the planets in our solar system underwent some form of migration during their formation, which could help to explain phenomena like the peculiar axial tilt of Uranus and Venus, the catastrophic impact that may have been responsible for the formation of the Moon, the Late Heavy Bombardment and the presence and distribution of planetesimals in the solar system (Thommes et al., 1999; Gomes et al., 2005; Tsiganis et al., 2005; Levison et al., 2008). The study of exoplanets therefore informs existential questions about the solar system, the Earth and the origins of life.

The discovery of a diverse exoplanet population concerns another major question that has insisted on humanity since the dawn of astronomy: *Does life exist on planets elsewhere in the universe?* When overall size and mass are considered, there are many planets that resemble the Earth (a.o. see Petigura et al., 2013; Foreman-Mackey et al., 2014; Silburt et al., 2015; Burke et al., 2015; Coughlin et al., 2016; Kane et al., 2016). A fraction of this population of rocky planets orbits at sufficient distance that the climate may be suspected to be temperate in what is called the *habitable zone*. The understanding that this population of habitable Earth-like planets may be significant in size has pulled the question of extra-terrestrial life out of the realm of science-fiction. The desire to find such Earth-like exoplanets and signatures of extra-terrestrial life is strong, and will likely be the most compelling driver for exoplanet science for decades to come.

However to successfully answer the questions discussed here, astronomers must have the ability to understand in detail the planets that they observe. This thesis is focussed on observational and data analysis methods by which exoplanets can be characterized using their spectral properties.

1.1.2 *How to find exoplanets*

There are several ways to detect planets that orbit other stars. Three of these are relevant to the work described in this thesis, and these have incidentally also been the most successful in yielding exoplanet discoveries.

The most commonly used techniques rely on the indirect effect of the planet on the light that we observe from the system. The radial-velocity method (or Doppler method) makes use of the periodic motion of the star as it orbits around the center of mass of the planetary system, which is not in the exact center of the star. The varying radial velocity of the star causes a corresponding Doppler-shift of the stellar spectrum, which is monitored for multiple orbital periods in order to confirm the gravitational pull of a planet. Because this is a gravitational effect, the amplitude K of the radial-velocity variation of the star depends on the mass of the planet m_p, the mass of the star M_*, the eccentricity e and the orbital distance of the planet which is pro-

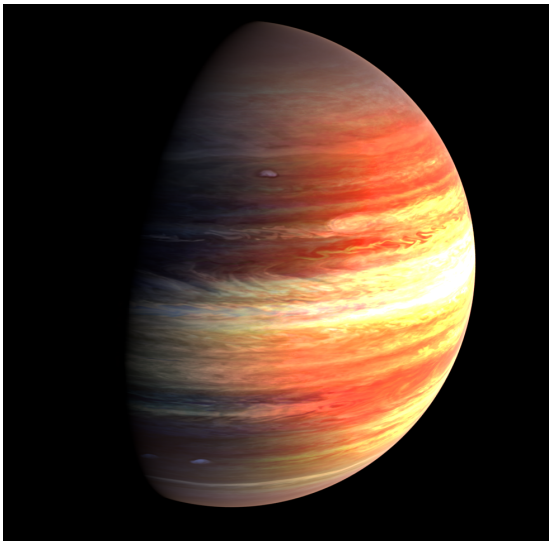

Figure 1.1: Artistic impression of what a hot Jupiter might look like.

portional to the orbital period P. This method is therefore mostly sensitive to massive planets in short-period orbits.

$$K = \left(\frac{2\pi G}{P}\right)^{\frac{1}{3}} \frac{m_p \sin(i)}{m_*^{\frac{2}{3}}} \frac{1}{\sqrt{1-e^2}}$$

The radial velocity method measures the velocity of the star along the line of sight. Velocity components in the plane perpendicular to the line of sight do not cause a Doppler effect, meaning that the radial velocity measurement also depends on the orientation of the orbital plane of the planet with respect to the line of sight. This orientation angle is quantified by the orbital inclination i. The magnitude of the radial velocity effect scales with $\sin i$, and the radial velocity method therefore yields only a lower limit to the mass of the planet.

The second method makes use of the fact that by chance, the orbital plane of some planets is aligned to our line-of-sight to the system (i.e. $i \sim 90°$). In this configuration, the planet passes in front of the stellar disk once during every orbit (see Figure 1.2). During such a transit, the planet blocks a fraction of the starlight, which can be detected in a photometric time-series of the system. The fraction of light blocked ($\frac{\Delta F}{F}$) is equal to the ratio of the projected areas of the disks of the planet and the star:

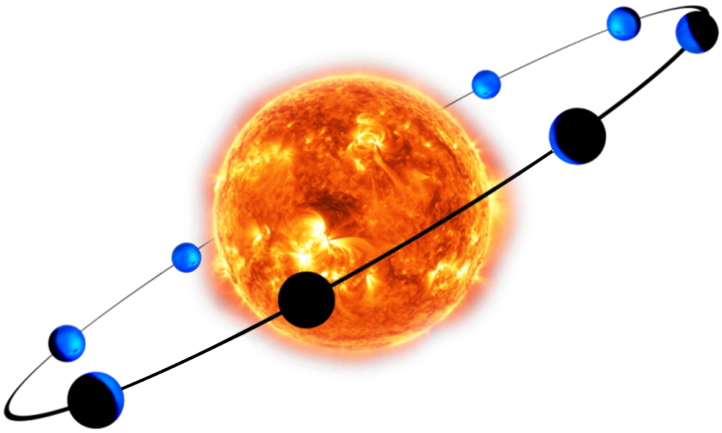

Figure 1.2: A planet in the transiting geometry. The transit occurs when the planet is in front of the star, while the secondary eclipse occurs when the planet moves behind it.

$$\frac{\Delta F}{F} = \frac{{R_p}^2}{{R_*}^2}$$

As such, this method is mostly sensitive to large planets in short orbits because a short orbital period allows for multiple transit events to be combined to increase the signal-to-noise. In addition, the likelihood of a favourable alignment is approximately proportional to the inverse of the orbital distance, which means that short-period planets are more likely to transit than planets further away from the star.

The transit of the planet also breaks the inclination degeneracy of the radial velocity method, allowing the true mass of the planet to be obtained. If the mass and radius of the star can be inferred independently, which is often the case, then the radial velocity and transit methods can be combined to reveal the mean density of the planet, which is a proxy for its composition and internal structure.

High-contrast imaging of an exoplanet system is the most direct way of finding exoplanets, but is often the most challenging. In high-contrast imaging, one tries to discern the point-source signal of the planet that is spatially separated from the much brighter host star. The wave-like nature of light fundamentally limits the spatial resolution of a telescope because it causes the light to diffract as it propagates through the aperture of the optical system. This diffraction pattern has a spatial extent that scales with wavelength and with the inverse of the size of the aperture. This means a point-source object is imaged as an extended Airy pattern on the detector, and that discerning

two closely separated point-sources is easiest for observations with large telescopes at short wavelengths.

In the case of a circular aperture, the diffraction pattern takes the form of an Airy function: A strong central peak surrounded by concentric rings that diminish away from the center. Two point source objects are considered to be resolved when their angular distance θ in radians is greater than $1.22\frac{\lambda}{D}$, where D is the diameter of the aperture.

However besides diffraction, ground-based telescopes are affected by distortion caused by the Earth's atmosphere that is highly variable in time. Visible to the naked eye, the *twinkling* of stars causes their image to be blurred, setting a limit to the angular resolution that can be achieved by ground-based telescopes (called the 'seeing' limit). Most planets are have an angular separation from their host star that is many times smaller than the seeing limit and are consequently masked by the distortion of the Earth's atmosphere. To counter this, ground-based high-contrast imaging instruments employ deformable optics (adaptive optics, AO) to correct for wave-front aberrations caused by atmospheric distortion in real-time (see e.g. Rousset et al., 2003; Beuzit et al., 2008; Jovanovic et al., 2015; Poyneer et al., 2016). High-quality AO systems can restore the image quality close to the diffraction limit, unlocking the full potential of large telescopes that would otherwise not be able to resolve spatial features smaller than the seeing limit.

Because high-contrast imaging works best for planets that are widely separated from their host stars, the sensitivity of this method is currently limited to a select part of the exoplanet population: Massive planets in wide orbits that are self-luminous due to the gradual release of primordial heat left-over from their formation. As such a system gets older, the contrast between the star and the planet increases and the planet becomes harder to observe directly. With current technology, high-contrast imaging is mostly limited to planets in orbits wider than ~ 5 AU in systems younger than ~ 1 Gyr (see e.g. Bowler, 2016). To be able to image cooler planets closer in requires the development of telescopes with large mirrors (needed to reduce the scale of the diffraction limit), combined with high-quality adaptive optics (often dubbed "extreme AO") and superior instrument stability.

1.1.3 *Unveiling the exoplanet population*

Over 25 years of exoplanet surveys have resulted in more than 3600 confirmed detections[2] (see Figure 1.3). Most of these planets were first discovered with the transit method. The most successful transit survey to date has been performed the Kepler Space Telescope, which has observed $\sim 150,000$ stars over a period of four years. It has identified over 4000 exoplanet candidates, of

2 Exoplanet.eu (Schneider et al., 2011)

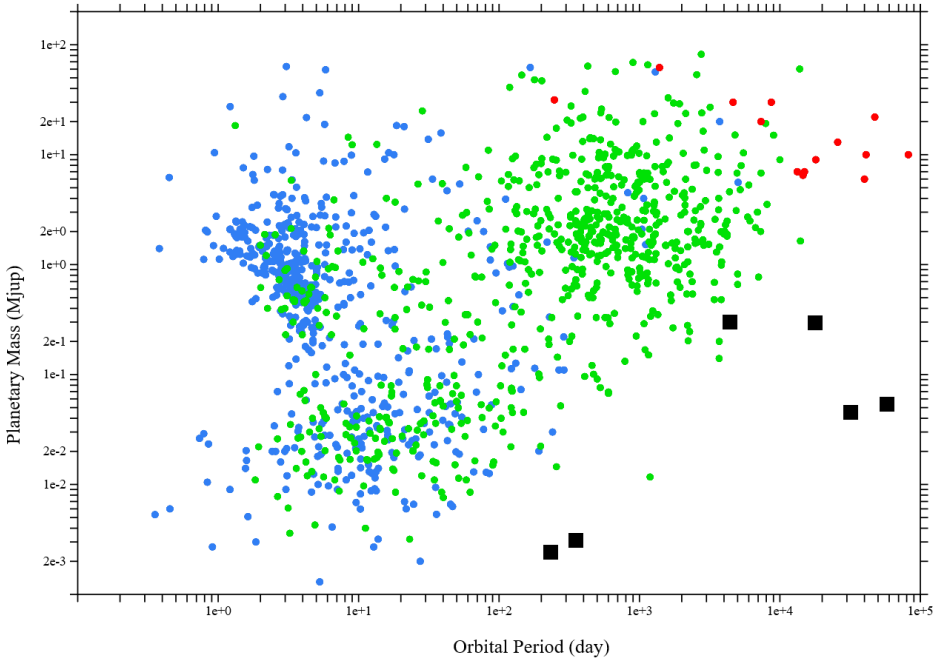

Figure 1.3: Confirmed exoplanet detections as of January 2017. Planets detected via radial velocity, transits an direct imaging are coloured green, blue and red respectively. The black squares indicate the solar system planets. Although the sensitivity of the planet-finding surveys generally decreases towards smaller planets at longer orbital periods, the detection of a large population of short-period rocky planets suggests that rocky planets far outnumber gas giants. Future planet-finding missions such as TESS and PLATO, as well as numerous ground-based transit and radial-velocity campaigns are predicted to better constrain the vast population of longer period rocky exoplanets.

which some 2300 have been independently confirmed[3]. Most of these planets reside in close orbits around their host stars with orbital periods of less than 20 days, and have radii greater than 2 Earth radii, which likely means that they have large gaseous envelopes (Howard et al., 2012; Owen et al., 2013; Fressin et al., 2013; Fulton et al., 2017). A fraction of these are comparable to the size of Jupiter, but most are smaller, and are referred to as warm Neptune analogues.

However, the high sensitivity of the Kepler light curves has also resulted in the discovery of ~ 1100 planets smaller than 2 Earth radii, which are likely to be rocky. This statistic indicates that there is a vast population of rocky

3 See https://www.nasa.gov/kepler/discoveries for the latest planet count.

planets straddling the inner regions of many, if not the majority of planetary systems (Petigura et al., 2013; Silburt et al., 2015; Burke et al., 2015; Mulders et al., 2016).

1.1.4 *Habitability*

A significant fraction of rocky exoplanets is expected to orbit their host stars in the *habitable zone*: at distances where the insolation is comparable to that of Earth so that the chemical environment at the planet surface could be favorable to life (Gaidos, 2013; Burke et al., 2015; Kane et al., 2016). There is no consensus about the extent of the habitable zone, because the amount of insolation that a planet receives is not the only determinant of habitability. The planet mass, size, composition and resulting atmospheric processes are also crucial factors (see e.g. Dole, 1964; Hart, 1979; Kopparapu et al., 2013; Zsom, 2015). The fact that habitability is the result of a complex interplay of processes is well illustrated by the planet Venus: Although similar to Earth in mass and composition and located on or near to the inner edge the habitable zone, the surface of Venus is one of the least hospitable places for life in the solar system because it attains an average surface temperature of 735 K due to the retention of sunlight and the resulting greenhouse effect. Furthermore, some rocky planets currently known are larger than the Earth and therefore significantly more massive. The solar system has no analogues of these *super-Earths*, which makes it even more difficult to predict the potential habitability of such planets.

For Sun-like stars, the habitable zone is roughly located between a distance of 0.5 to 2.5 AU from the Sun. Habitable planets in these systems therefore have orbital periods on the order of hundreds of days, limiting the sensitivity of photometric transit and radial velocity monitoring. This is why the search for habitable Earth-like planets is now focussed on M-dwarfs. Due to their low effective temperature, the habitable zone typically extends from 0.05 to 0.2 AU (Kopparapu, 2013) and therefore such planets have short periods in the order of 10 days. Recent high-profile discoveries of rocky planets around M-dwarfs include the detection of an $m \sin i = 1.3 m_E$ planet orbiting the nearby star Proxima Centauri b (Anglada-Escudé et al., 2016), and the discovery of seven transiting Earth-sized planets in the TRAPPIST-1 system (Gillon et al., 2016; Gillon et al., 2017), three of which are likely located in the habitable zone. Considering the size of the exoplanet population, ongoing and future planet-finding surveys will likely reveal a wealth of similar systems, each with potentially habitable planets.

However, the example of Venus above illustrates another important point: Venus's surface is perpetually covered by a thick cloud deck that hinders remote sensing of the surface below. Before the first radio observations pen-

etrated its dense atmosphere and revealed the extreme nature of the surface environment (Mayer et al., 1958), speculations about a temperate climate, the presence of molecular oxygen, water and even life on Venus were not uncommon (see e.g. Henkel, 1909; St. John et al., 1922; Whipple, 1931; Martz, 1934; Menzel et al., 1954). This demonstrates that planet climates are complex, and that a careful characterization of the atmospheres of Earth-like exoplanets is crucial to correctly assess their habitability.

1.2 SPECTROSCOPIC CHARACTERIZATION

1.2.1 *The spectrum of an exoplanet*

To learn more about a planet than its size and mass, the light of the planet must be studied directly. The spectral properties of the light that originates from the planet are determined by the thermal, chemical and material properties of its outer layers. The spectrum of an exoplanet is made up of two distinct components: Starlight that is reflected or scattered by the planet, and light that is emitted (thermally or otherwise) by the planet itself. Stars generally emit most of their radiation at optical wavelengths. The planet reflects a fraction of this light back into space, and the rest is absorbed and heats the atmosphere (Hansen, 2008). The fraction of all starlight that is not absorbed by the planet is called the *Bond Albedo*. Combined with any heat sources in the interior of the planet, the albedo determines the energy budget of the planet which in turn determines the overall temperature. To first order, the planet re-emits the absorbed starlight like a black-body, so the temperature of the planet can be constrained by measuring the amount of thermal radiation, possibly in multiple bands (see e.g. Charbonneau et al., 2005; Deming et al., 2006; Knutson et al., 2007; Harrington et al., 2007; Machalek et al., 2008; Gillon et al., 2010; Beaulieu et al., 2010; Smith et al., 2011; Demory et al., 2012; Demory et al., 2016).

The transiting geometry offers the possibility of *transmission* spectroscopy: Starlight that passes through the optically thin outer layers of the atmosphere is imprinted with absorption from the chemical constituents of the atmosphere (see e.g. Seager et al., 2000; Brown, 2001; Charbonneau et al., 2002; Tinetti et al., 2007; Barman, 2007; Burrows et al., 2008; Snellen et al., 2008; Désert et al., 2008; Sing et al., 2011). This effect manifests itself as a wavelength-dependence of the effective radius of the planet: At the wavelength of an atmospheric absorption line, the atmosphere is less transparent than at other wavelengths. This means that inside an absorption line, the planet causes a slightly deeper transit and will hence appear to be larger. The fractional increase of the apparent radius due to absorption by an atom or molecule in a layer ΔR above the effective radius R_p of the planet is:

$$\frac{2\Delta R\ R_p}{R_*^2}$$

ΔR is the height of the absorbing layer, and is generally proportional to the scale-height H of the atmosphere:

$$H = \frac{kT}{\mu g}$$

where T is the temperature, μ is the mean molecular weight and g is the surface gravity. This shows that some planets are more accessible to spectroscopic characterization than others, depending on the temperature, the atmospheric composition and the planet radius. This interpretation of the spectrum also indicates that the core of a spectral line represents a large value of ΔR, whereas the wings of the line correspond to smaller values of ΔR. Assuming that the opacity of the atmosphere decreases with altitude, this implies that the core of the line is formed high up in the atmosphere, whereas the wings of the line (in which the atom/molecule has an intrinsically smaller absorption cross-section) originate from deeper layers of the atmosphere. At the same time, the width of a spectral line depends on the local temperature and pressure. As such, the shape of an absorption line can in principle be used to constrain the thermal structure of the atmosphere (see e.g. Sing et al., 2008; Vidal-Madjar et al., 2011; Huitson et al., 2012; Schwarz et al., 2016).

Besides absorption by chemicals, another important source of opacity is scattering by aerosols and the blocking of light by optically thick clouds. Like on Earth, aerosols in the atmosphere tend to scatter radiation at short wavelengths, causing an apparent increase of the radius of a transiting exoplanet towards short wavelengths. The slope of the scattering spectrum can be be used to constrain the local temperature and molecular weight (Lecavelier Des Etangs et al., 2008; Benneke et al., 2012). Such observations have been performed on multiple occasions, mostly using the STIS and WFC3 on the Hubble Space Telescope which have coverage in the UV, optical and NIR. Transmission spectroscopy observations have also revealed that the spectra of many exoplanets are relatively featureless (e.g. Pont et al., 2008; Sing et al., 2009; Deming et al., 2013; Bento et al., 2014; Kreidberg et al., 2014; Nikolov et al., 2014; Sing et al., 2016; Kirk et al., 2017). The interpretation of these observations is that many planets possess cloud decks that make the atmosphere optically thick up to high altitudes, masking the layers that would otherwise produce absorption features.

Observations at infra-red wavelengths are sensitive to the thermally emitted radiation of the planet. This radiation traverses the upper optically thin layers of the atmosphere before being released into space, and may also carry imprints of the chemical species in the atmosphere (Seager et al., 2005;

Richardson et al., 2007). This radiation is most readily measured by observing the secondary eclipse of a transiting planet: Just before and after moving behind the star, the full day-side of the planet is in view. As the planet moves behind the star, this light is blocked, and the total amount of light observed from the system drops by an amount equal to the light emitted by the planet. Observing this difference at various wavelengths then reveals the thermal spectrum of the planet, constraining the dayside temperature and possible emission or absorption from atoms or molecules in the atmosphere. During the rest of the orbit, the observed flux of the system varies depending on what fraction of the day-side is in view, as well as the temperature difference between the day and night sides. Such *phase-curve* and secondary eclipse observations are regularly performed by the IRAC instrument aboard the Spitzer Space Telescope, which observes in two photometric bands at 3.6 μm and 4.5 μm, and until the depletion of its helium reservoir had access to bands at 5.3 μm and 8 μm. These observations have shown that hot Jupiters have strong day-to-night side temperature contrasts, hot-spots that are shifted away from the sub-stellar point by strong equatorial winds, and have even allowed day-side temperature maps to be derived (see e.g. Charbonneau et al., 2005; Deming et al., 2006; Deming et al., 2007; Demory et al., 2007; Charbonneau et al., 2008; Knutson et al., 2008; Gillon et al., 2010; Agol et al., 2010; Madhusudhan et al., 2011; Cowan et al., 2012; Demory et al., 2012; Todorov et al., 2013; Stevenson et al., 2014; Zellem et al., 2014; Demory et al., 2016).

Such observations have indicated that the hottest hot Jupiters may emit excess thermal light above what would be expected from their equilibrium temperature (Haynes et al., 2015; Evans et al., 2017). This has been explained by the presence of emission lines of water. Molecular lines are seen in emission when the layer in which the species is present is hotter than the layers below. This phenomenon is called a *thermal inversion layer*: an atmospheric layer in which the temperature increases with altitude. An inversion layer is caused by heating of the layer due to the presence of some chemical species that efficiently absorbs starlight. In the Earth's atmosphere, the ozone layer causes an inversion layer between altitudes of 10 km to 50 km, and similar processes are expected to occur in the atmospheres of hot Jupiters, albeit caused by different short-wavelength absorbers.

Titanium and vanadium oxide (TiO/VO) have rich optical absorption spectra that dominate the optical spectra of cool dwarf stars. Because the atmospheres of hot Jupiters can reach temperatures equivalent to the photospheres of the coolest stars, TiO and VO were naturally invoked as possible heat sources for inversion layers. The discovery of molecular emission at thermal wavelengths has therefore sparked searches for TiO and VO in transit transmission spectra, but until recently with very limited success (e.g. Désert et al., 2008; Evans et al., 2016).

1.2.2 *Spectral resolving power*

The difficulty in detecting molecular features in the spectra of exoplanets is partly because absorption bands of various molecules may overlap. If unknown quantities of molecular absorbers with overlapping absorption bands are mixed, the resulting absorption spectra can be difficult to interpret (Brogi et al., 2017). However, molecular absorption bands are composed of thousands to millions of individual absorption lines that are closely separated due to the fine structure of the energy levels of the molecule.

The resolving power R of a spectrograph describes the spectral scale $\Delta\lambda$ that can be resolved in a spectrum at wavelength λ:

$$R = \frac{\lambda}{\Delta\lambda}$$

The size and weight of a spectrograph generally increase proportionally with the amount of wavelength-dispersion because of the geometrical path-length required to convert a small dispersion angle to a large dispersion distance on the detector. This means that space-based spectrographs are typically limited to resolving powers of $R \sim 10^2$, at which the overall shape of the exoplanet spectrum can be resolved. In the optical, the spectrum is dominated by scattering by aerosols at blue wavelengths, strong atomic lines by alkali metals and the outlines of molecular absorption bands, but at $R \sim 10^2$, the latter cannot be resolved into individual absorption lines. However ground-based spectrographs can reach higher resolving powers of $R \sim 10^5$ at which individual spectral lines can be separated, allowing different molecular species to be distinguished at high confidence because the spectral fingerprint of each molecule is unique.

From the equation above, the resolving power can also be expressed in terms of the Doppler shift caused by a radial velocity Δv:

$$R = \frac{c}{\Delta v}$$

Current high-dispersion spectrographs can therefore resolve velocities down to a few $\mathrm{km\,s^{-1}}$. This is sufficient to resolve the orbital velocity of most planets, as well as the typical systematic velocity of the system relative to the Sun. This has the advantage that besides robust sensitivity to individual absorption lines, the planet can also be distinguished based on its velocity with respect to the host star and the Earth's atmosphere. High-dispersion observations therefore have the potential to strongly constrain the chemical composition of an exoplanet atmosphere.

1.2.3 *Cross-correlation*

The high dispersion of a high-resolution spectrograph means that the number of photons that is obtained per spectral element $\Delta\lambda$ is limited. For a typical high-dispersion transit observing sequence, the individual absorption lines are embedded in the photon noise of the much brighter star. Cross-correlation techniques can be used to match a model template spectrum to the observed spectrum to extract the planet spectrum from the noise. The cross-correlation $C(x, y)$ effectively measures the degree of similarity between a spectral template x_k and the noisy data y_k:

$$C(x, y) = \frac{\sum_{k=0}^{N}(x_k - \bar{x})(y_k - \bar{y})}{\sqrt{\sum_{k=0}^{N}(x_k - \bar{x})^2 \sum_{k=0}^{N-1}(y_k - \bar{y})^2}}$$

$C(x, y)$ varies between 1.0 (maximum correlation, i.e. when $y = ax + b$ with a and b constants and $a > 0$) and -1.0 (anti-correlation, i.e. when $a < 0$). The cross-correlation C is calculated for a range of radial velocity shifts of the template x. This yields the cross-correlation function $CCF(x, y, v)$, which measures the degree of overlap between the template and the data as a function of radial velocity v. The CCF peaks when the template is shifted to the same radial velocity as the data, and effectively co-adds all the absorption lines that are present in both the template and the data. This integration of the spectrum acts to average out the photon noise that is present at each spectral line, allowing the template spectrum to be detected even if the photon noise is stronger than the individual absorption lines.

The position of the cross-correlation peak in velocity space corresponds to the Doppler shift of the target spectrum at the time of the observations. As such, the CCF can be used to precisely measure the radial velocity of a target object. This technique has been used to detect molecular absorption by CO and H_2O in the day side emission spectra of a number of hot Jupiters (Snellen et al., 2010; Brogi et al., 2012; Brogi et al., 2013; Birkby et al., 2013; de Kok et al., 2013; Brogi et al., 2014; Lockwood et al., 2014; Brogi et al., 2016; Piskorz et al., 2016; Birkby et al., 2017; Piskorz et al., 2017). Also, it has enabled measurements of the instantaneous radial velocity of non-transiting hot Jupiters τ Bootis b, 51 Peg b and HD 179733 b yielding the orbital inclination i and therefore breaking the degeneracy with the planet mass that is inherent to the radial velocity method (Brogi et al., 2012; Brogi et al., 2013; Brogi et al., 2014). In addition, this technique has been used to measure the spin rate of hot giant planets β Pictoris b and GQ Lupi b, because the width of the cross-correlation function is partially due to velocity broadening caused by rotation of the planet (Snellen et al., 2014; Schwarz et al., 2016).

1.2.4 *Spectral dispersion and spatial resolution*

To increase the sensitivity of exoplanet observations, high-dispersion spectroscopy can be combined with high-contrast imaging (Sparks et al., 2002; Snellen et al., 2015). Light that originates from the planet is distinguished from the dominating starlight by simultaneously resolving the planet in the field, as well as using its spectral properties that are different from that of the star. This results in deeper contrast limits compared to traditional direct-imaging methods, especially close to the star where the signal of the planet is hard to distinguish from diffracted starlight (Lovis et al., 2017; Luger et al., 2017; Mawet et al., 2017; Wang et al., 2017).

To achieve this, the spectrograph needs to obtain spectra from a range of directions on the sky. One-dimensional spatial resolution can be achieved using a slit spectrograph: If the planet and the star are oriented parallel to the direction of the slit, the spatial separation between the two can be used to reject a fraction of the stellar spectrum if the planet and the star are resolved (Snellen et al., 2015). However, this requires knowledge about the orientation of the system, and spatial resolution is limited to one spatial dimension.

Integral-field spectrographs (IFS) achieve two-dimensional spatial resolution by dividing the field-of-view into separate sub-fields each of which is independently dispersed. This can be done using an image-slicer, which slices the field into multiple sub-slits (see Figure 1.4), or with an array of micro-lenses, each of which images a different part of the field of view. The data-reduction pipeline of an integral-field spectrograph typically produces a three-dimensional *data cube* from each science observation. Two axes of the cube represent the spatial dimensions on the sky, while the third dimension covers wavelength (see Figure 1.5). The addition of this third dimension of information means that a trade-off must be made between spatial and spectral resolution and coverage, because all the information needs to be contained on a two-dimensional detector. This trade-off is driven by the science-case for which the instrument is designed (see Chapter 3).

Integral-field spectrographs therefore have fewer detector pixels available for capturing spectral information compared to their high-dispersion counterparts. Both the VLT and Keck telescopes have near-infrared IFS's (SINFONI and OSIRIS) that can be operated in combination with their respective AO systems, making these instruments suitable for high-contrast imaging of hot young gas giants. The spectral resolving power lies in the range of $R \sim 3000$ to $R \sim 5000$, equivalent to radial velocities of 100 to 60 km s^{-1}. Such resolving power is not sufficient to resolve the orbital velocity of a planet or individual absorption lines, but the cross-correlation may still provide significant contrast enhancement (see Chapter 5).

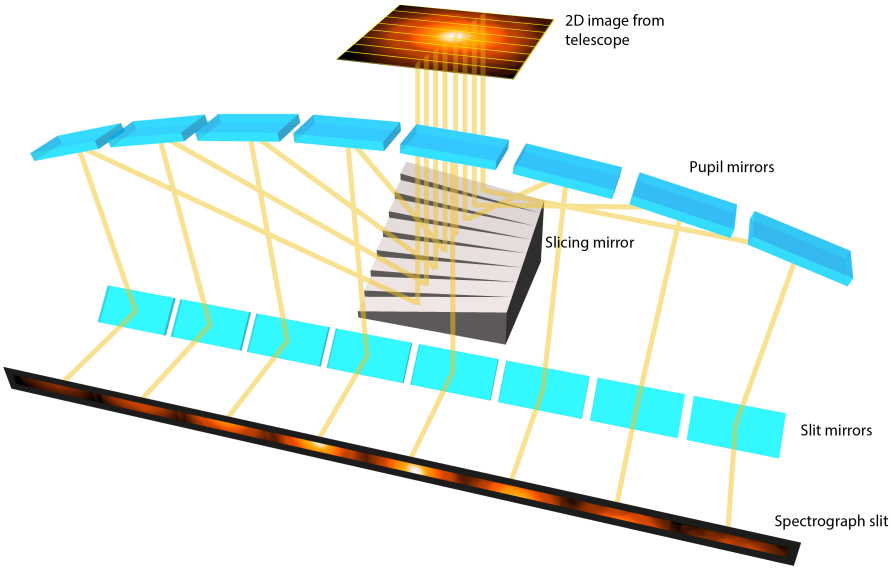

Figure 1.4: Conceptual representation of an image slicer used for integral-field slit-spectroscopy. The 2D image formed by the telescope is cut into a number of sub-slits which are re-imaged onto the entrance slit of the spectrograph side-by-side. These are then spectrally dispersed and imaged onto a two-dimensional CCD.

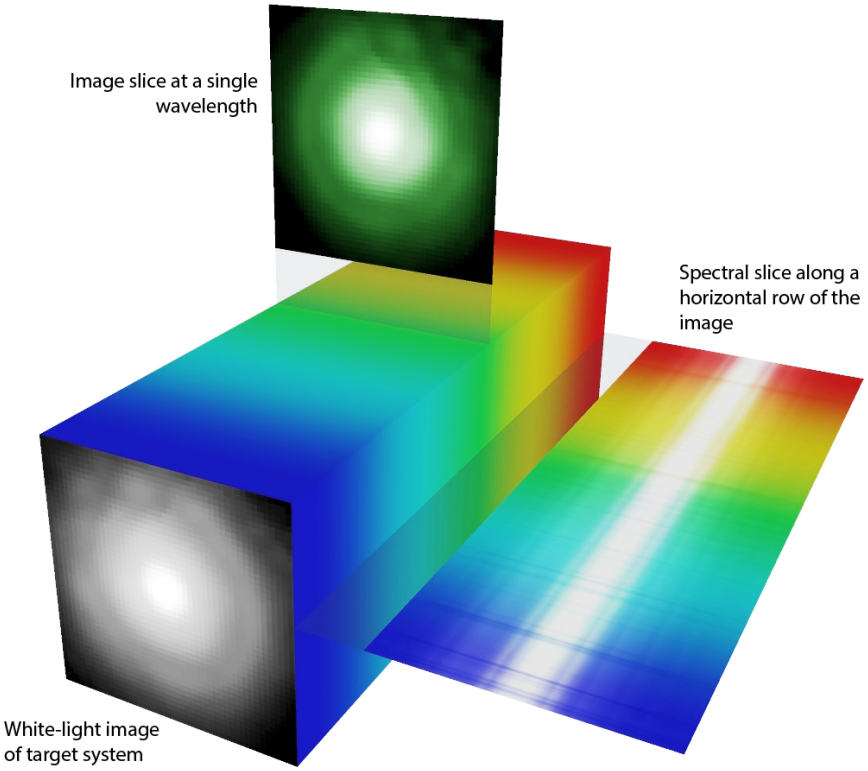

Figure 1.5: Graphical representation of a 3-dimensional data cube of an integral-field observation of an exoplanet system.

1.2.5 *Spectropolarimetry*

Light can be described as the propagation of a transversal wave in the electric and magnetic field according to the equations of Maxwell. The electric and magnetic fields oscillate in perpendicular planes and the spatial orientation of these planes together with the phase of the oscillation are referred to as the *polarization state* of light.

Thermal radiation is caused by the random motion of an ensemble of charged particles. Because of this random nature, thermal radiation has no preferred orientation on average, and the observed electric field vector oscillates randomly in all directions. Starlight is therefore *unpolarized*. However, this symmetry is broken upon reflection off a surface: Depending on the geometry and the properties of the medium, the wave that oscillates in the plane that is perpendicular to the surface of the medium will be attenuated. This means that starlight that is scattered by the atmosphere or surface of an exoplanet may be polarized by tens of percent, and this degree of polarization holds information about the scattering material. Polarization observations of exoplanets may therefore provide additional diagnostics of their atmospheres and surfaces (see e.g. Stam et al., 2004; Stam, 2008; Karalidi et al., 2012). In addition to preferentially selecting one polarization direction, some modes of scattering may also induce a phase delay between the polariation directions. This causes the field vector to rotate around the axis of propagation, and is referred to as circular polarization. Circular polarization occurs rarely in astronomical sources, and is mainly associated with complex organic molecules and biological processes (Sparks et al., 2009; Sparks et al., 2012).

Measurements of the polarization state of the exoplanet spectrum may unlock such observables in future observations of exoplanets. However, these observations will be challenging because absolute calibration of polarization measurements is technologically difficult and because the global appearance of such biomarkers on exoplanets are not yet experimentally corroborated (see Chapter 3).

1.3 THIS THESIS

If astronomers want to fully understand and characterize exoplanets, astronomical observations must overcome extreme contrasts and reliably measure the intensity and polarization over large ranges of the electromagnetic spectrum at high spectral and spatial resolving power. The work presented in this thesis aims to contribute to this endeavour by applying and developing new ways to perform and analyse exoplanet observations. As larger, more sensitive facilities are being developed, these techniques may be used in the

future to characterize the surface environments of exoplanets, to assess their habitability and potentially to aid in the discovery of extra-terrestrial life.

Chapter 2 describes the application of the cross-correlation method to search for gaseous TiO in the atmosphere of hot Jupiter HD 209458 b, potentially associated with a thermal inversion layer. The data was obtained by the high-dispersion spectrograph (HDS) on the Subaru telescope, and spans one transit of HD 209458 b at optical wavelengths. The TiO molecule has millions of absorption lines throughout the optical. We find that this dataset can be used to discern the presence of TiO in the atmosphere in HD 209458 b down to volume mixing ratios below 10^{-9}. However, the theoretical line-lists that are used to model the template spectrum needed to cross-correlate the data with, are inaccurate at high spectral resolution, hampering application of cross-correlation. This paper therefore advocates for more precise modelling of the energy levels of TiO and other relevant molecules, or spectroscopic measurements in the laboratory. This work has previously appeared in A&A (Hoeijmakers et al., 2015).

Chapter 3 presents a prototype for the Lunar Observatory for Unresolved Polarimetry of Earth (LOUPE). This instrument is designed to observe the Earth from the surface of the Moon and characterize its optical linear polarization spectrum as if it was an exoplanet. These data are needed to benchmark future polarization observations of potentially habitable exoplanets. We show that such an instrument can be small, robust and fully solid-state, which is essential for application and reliable operation in space. This work has been published in Optics Express (Hoeijmakers et al., 2016).

Chapter 4 presents an analysis of over 2000 archival high-resolution optical spectra of the τ Boötis system to search for the reflected light of the non-transiting hot Jupiter τ Boötis b. This data was obtained by various spectrographs between 1998 and 2011, and when combined provides a 1σ sensitivity to the reflected stellar spectrum of 5.0×10^{-6} times the brightness of the star. The planet is not detected however, which means that it likely has an albedo $p < 0.11$. Although low, such albedo values are not uncommon for hot Jupiters as evidenced by phase-curve observations by space telescopes.

Chapter 5 presents the first application of the cross-correlation technique to high-contrast imaging observations of the young gas giant β Pictoris b, obtained by the SINFONI integral-field spectrograph at the VLT in K-band. We successfully remove the stellar flux from the data and reveal the planet by cross-correlating with model spectra of CO and H_2O. The

cross-correlation function produces *molecule maps* of the system, which provide an alternative to established high-contrast imaging methods that suffer from residual starlight, especially at small angular distances from the star. We show that this technique has significant potential when applied with data of NIRSpec, MIRI and HARMONI; upcoming medium-resolution integral-field spectrographs on the James Webb Space Telescope and the ELT.

BIBLIOGRAPHY

Agol, E. et al. (2010). „The Climate of HD 189733b from Fourteen Transits and Eclipses Measured by Spitzer." In: *ApJ* 721, pp. 1861–1877. DOI: 10.1088/0004-637X/721/2/1861. arXiv: 1007.4378 [astro-ph.EP].

Anglada-Escudé, G. et al. (2016). „A terrestrial planet candidate in a temperate orbit around Proxima Centauri." In: *Nature* 536, pp. 437–440. DOI: 10.1038/nature19106. arXiv: 1609.03449 [astro-ph.EP].

Barman, T. (2007). „Identification of Absorption Features in an Extrasolar Planet Atmosphere." In: *ApJ* 661, pp. L191–L194. DOI: 10.1086/518736. arXiv: 0704.1114.

Beaulieu, J. P. et al. (2010). „Water in the atmosphere of HD 209458b from 3.6-8 μm IRAC photometric observations in primary transit." In: *MNRAS* 409, pp. 963–974. DOI: 10.1111/j.1365-2966.2010.16516.x. arXiv: 0909.0185 [astro-ph.EP].

Benneke, B. and S. Seager (2012). „Atmospheric Retrieval for Super-Earths: Uniquely Constraining the Atmospheric Composition with Transmission Spectroscopy." In: *ApJ* 753, 100, p. 100. DOI: 10.1088/0004-637X/753/2/100. arXiv: 1203.4018 [astro-ph.EP].

Bento, J. et al. (2014). „Optical transmission photometry of the highly inflated exoplanet WASP-17b." In: *MNRAS* 437, pp. 1511–1518. DOI: 10.1093/mnras/stt1979. arXiv: 1310.3893 [astro-ph.EP].

Beuzit, J.-L. et al. (2008). „SPHERE: a 'Planet Finder' instrument for the VLT." In: *Ground-based and Airborne Instrumentation for Astronomy II*. Vol. 7014. Proc. SPIE, p. 701418. DOI: 10.1117/12.790120.

Birkby, J. L. et al. (2013). „Detection of water absorption in the day side atmosphere of HD 189733 b using ground-based high-resolution spectroscopy at 3.2 μm." In: *MNRAS* 436, pp. L35–L39. DOI: 10.1093/mnrasl/slt107. arXiv: 1307.1133 [astro-ph.EP].

Birkby, J. L. et al. (2017). „Discovery of Water at High Spectral Resolution in the Atmosphere of 51 Peg b." In: *AJ* 153, 138, p. 138. DOI: 10.3847/1538-3881/aa5c87. arXiv: 1701.07257 [astro-ph.EP].

Boss, A. P. (1997). „Giant planet formation by gravitational instability." In: *Science* 276, pp. 1836–1839. DOI: 10.1126/science.276.5320.1836.

Bowler, B. P. (2016). „Imaging Extrasolar Giant Planets." In: *PASP* 128.10, p. 102001. DOI: 10.1088/1538-3873/128/968/102001. arXiv: 1605.02731 [astro-ph.EP].

Brogi, M. et al. (2012). „The signature of orbital motion from the dayside of the planet τ Boötis b." In: *Nature* 486, pp. 502–504. DOI: 10.1038/nature11161. arXiv: 1206.6109 [astro-ph.EP].

Brogi, M. et al. (2013). „Detection of Molecular Absorption in the Dayside of Exoplanet 51 Pegasi b?" In: *ApJ* 767, 27, p. 27. DOI: 10.1088/0004-637X/767/1/27. arXiv: 1302.6242 [astro-ph.EP].

Brogi, M. et al. (2014). „Carbon monoxide and water vapor in the atmosphere of the non-transiting exoplanet HD 179949 b." In: *A&A* 565, A124, A124. DOI: 10.1051/0004-6361/201423537. arXiv: 1404.3769 [astro-ph.EP].

Brogi, M. et al. (2016). „Rotation and Winds of Exoplanet HD 189733 b Measured with High-dispersion Transmission Spectroscopy." In: *ApJ* 817, 106, p. 106. DOI: 10.3847/0004-637X/817/2/106. arXiv: 1512.05175 [astro-ph.EP].

Brogi, M. et al. (2017). „A Framework to Combine Low- and High-resolution Spectroscopy for the Atmospheres of Transiting Exoplanets." In: *ApJ* 839, L2, p. L2. DOI: 10.3847/2041-8213/aa6933. arXiv: 1612.07008 [astro-ph.EP].

Brown, T. M. (2001). „Transmission Spectra as Diagnostics of Extrasolar Giant Planet Atmospheres." In: *ApJ* 553, pp. 1006–1026. DOI: 10.1086/320950. eprint: astro-ph/0101307.

Burke, C. J. et al. (2015). „Terrestrial Planet Occurrence Rates for the Kepler GK Dwarf Sample." In: *ApJ* 809, 8, p. 8. DOI: 10.1088/0004-637X/809/1/8. arXiv: 1506.04175 [astro-ph.EP].

Burrows, A., J. Budaj, and I. Hubeny (2008). „Theoretical Spectra and Light Curves of Close-in Extrasolar Giant Planets and Comparison with Data." In: *ApJ* 678, 1436-1457, pp. 1436–1457. DOI: 10.1086/533518. arXiv: 0709.4080.

Butler, R. P. et al. (2006). „Catalog of Nearby Exoplanets." In: *ApJ* 646, pp. 505–522. DOI: 10.1086/504701. eprint: astro-ph/0607493.

Charbonneau, D. et al. (2002). „Detection of an Extrasolar Planet Atmosphere." In: *ApJ* 568, pp. 377–384. DOI: 10.1086/338770. eprint: astro-ph/0111544.

Charbonneau, D. et al. (2005). „Detection of Thermal Emission from an Extrasolar Planet." In: *ApJ* 626, pp. 523–529. DOI: 10.1086/429991. eprint: astro-ph/0503457.

Charbonneau, D. et al. (2008). „The Broadband Infrared Emission Spectrum of the Exoplanet HD 189733b." In: *ApJ* 686, 1341-1348, pp. 1341–1348. DOI: 10.1086/591635. arXiv: 0802.0845.

Coughlin, J. L. et al. (2016). „Planetary Candidates Observed by Kepler. VII. The First Fully Uniform Catalog Based on the Entire 48-month Data Set (Q1-Q17 DR24)." In: *ApJ* 224, 12, p. 12. DOI: 10.3847/0067-0049/224/1/12. arXiv: 1512.06149 [astro-ph.EP].

Cowan, N. B. et al. (2012). „Thermal Phase Variations of WASP-12b: Defying Predictions." In: *ApJ* 747, 82, p. 82. DOI: 10.1088/0004-637X/747/1/82. arXiv: 1112.0574 [astro-ph.EP].

de Kok, R. J. et al. (2013). „Detection of carbon monoxide in the high-resolution day-side spectrum of the exoplanet HD 189733b." In: *A&A* 554, A82, A82. DOI: 10.1051/0004-6361/201321381. arXiv: 1304.4014 [astro-ph.EP].

Deming, D. et al. (2006). „Strong Infrared Emission from the Extrasolar Planet HD 189733b." In: *ApJ* 644, pp. 560–564. DOI: 10.1086/503358. eprint: astro-ph/0602443.

Deming, D. et al. (2007). „Spitzer Transit and Secondary Eclipse Photometry of GJ 436b." In: *ApJ* 667, pp. L199–L202. DOI: 10.1086/522496. arXiv: 0707.2778.

Deming, D. et al. (2013). „Infrared Transmission Spectroscopy of the Exoplanets HD 209458b and XO-1b Using the Wide Field Camera-3 on the Hubble Space Telescope." In: *ApJ* 774, 95, p. 95. DOI: 10.1088/0004-637X/774/2/95. arXiv: 1302.1141 [astro-ph.EP].

Demory, B.-O. et al. (2007). „Characterization of the hot Neptune GJ 436 b with Spitzer and ground-based observations." In: *A&A* 475, pp. 1125–1129. DOI: 10.1051/0004-6361:20078354. arXiv: 0707.3809.

Demory, B.-O. et al. (2012). „Detection of Thermal Emission from a Super-Earth." In: *ApJ* 751, L28, p. L28. DOI: 10.1088/2041-8205/751/2/L28. arXiv: 1205.1766 [astro-ph.EP].

Demory, B.-O. et al. (2016). „A map of the large day-night temperature gradient of a super-Earth exoplanet." In: *Nature* 532, pp. 207–209. DOI: 10.1038/nature17169. arXiv: 1604.05725 [astro-ph.EP].

Désert, J.-M. et al. (2008). „TiO and VO broad band absorption features in the optical spectrum of the atmosphere of the hot-Jupiter HD 209458b." In: *A&A* 492, pp. 585–592. DOI: 10.1051/0004-6361:200810355. arXiv: 0809.1865.

Dole, S. H. (1964). *Habitable planets for man*.

Evans, T. M. et al. (2016). „Detection of H_2O and Evidence for TiO/VO in an Ultra-hot Exoplanet Atmosphere." In: *ApJ* 822, L4, p. L4. DOI: 10.3847/2041-8205/822/1/L4. arXiv: 1604.02310 [astro-ph.EP].

Evans, T. M. et al. (2017). „An ultrahot gas-giant exoplanet with a stratosphere." In: *Nature* 548, pp. 58–61. DOI: 10.1038/nature23266. arXiv: 1708.01076 [astro-ph.EP].

Foreman-Mackey, D., D. W. Hogg, and T. D. Morton (2014). „Exoplanet Population Inference and the Abundance of Earth Analogs from Noisy, Incomplete Catalogs." In: *ApJ* 795, 64, p. 64. DOI: 10.1088/0004-637X/795/1/64. arXiv: 1406.3020 [astro-ph.EP].

Fressin, F. et al. (2013). „The False Positive Rate of Kepler and the Occurrence of Planets." In: *ApJ* 766, 81, p. 81. DOI: 10.1088/0004-637X/766/2/81. arXiv: 1301.0842 [astro-ph.EP].

Fulton, B. J. et al. (2017). „The California-Kepler Survey. III. A Gap in the Radius Distribution of Small Planets." In: *ArXiv e-prints*. arXiv: 1703.10375 [astro-ph.EP].

Gaidos, E. (2013). „Candidate Planets in the Habitable Zones of Kepler Stars." In: *ApJ* 770, 90, p. 90. DOI: 10.1088/0004-637X/770/2/90. arXiv: 1301.2384 [astro-ph.EP].

Gillon, M. et al. (2010). „The thermal emission of the young and massive planet CoRoT-2b at 4.5 and 8 μm." In: *A&A* 511, A3, A3. DOI: 10.1051/0004-6361/200913507. arXiv: 0911.5087 [astro-ph.EP].

Gillon, M. et al. (2016). „Temperate Earth-sized planets transiting a nearby ultracool dwarf star." In: *Nature* 533, pp. 221–224. DOI: 10.1038/nature17448. arXiv: 1605.07211 [astro-ph.EP].

Gillon, M. et al. (2017). „Seven temperate terrestrial planets around the nearby ultracool dwarf star TRAPPIST-1." In: *Nature* 542, pp. 456–460. DOI: 10.1038/nature21360. arXiv: 1703.01424 [astro-ph.EP].

Gomes, R. et al. (2005). „Origin of the cataclysmic Late Heavy Bombardment period of the terrestrial planets." In: *Nature* 435, pp. 466–469. DOI: 10.1038/nature03676.

Hansen, B. M. S. (2008). „On the Absorption and Redistribution of Energy in Irradiated Planets." In: *ApJ* 179, 484-508, pp. 484–508. DOI: 10.1086/591964. arXiv: 0801.2972.

Hansen, B. M. S., H.-Y. Shih, and T. Currie (2009). „The Pulsar Planets: A Test Case of Terrestrial Planet Assembly." In: *ApJ* 691, pp. 382–393. DOI: 10.1088/0004-637X/691/1/382. arXiv: 0908.0736 [astro-ph.EP].

Harrington, J. et al. (2007). „The hottest planet." In: *Nature* 447, pp. 691–693. DOI: 10.1038/nature05863.

Hart, M. H. (1979). „Habitable Zones about Main Sequence Stars." In: *Icarus* 37, pp. 351–357. DOI: 10.1016/0019-1035(79)90141-6.

Haynes, K. et al. (2015). „Spectroscopic Evidence for a Temperature Inversion in the Dayside Atmosphere of Hot Jupiter WASP-33b." In: *ApJ* 806, 146, p. 146. DOI: 10.1088/0004-637X/806/2/146. arXiv: 1505.01490 [astro-ph.EP].

Henkel, F. W. (1909). „Venus as the Abode of Life." In: *Popular Astronomy* 17, pp. 412–417.

Hennebelle, P. and G. Chabrier (2008). „Analytical Theory for the Initial Mass Function: CO Clumps and Prestellar Cores." In: *ApJ* 684, 395-410, pp. 395–410. DOI: 10.1086/589916. arXiv: 0805.0691.

Hoeijmakers, H. J. et al. (2015). „A search for TiO in the optical high-resolution transmission spectrum of HD 209458b: Hindrance due to inaccuracies in the line database." In: *A&A* 575, A20, A20. DOI: 10.1051/0004-6361/201424794. arXiv: 1411.6017 [astro-ph.EP].

Hoeijmakers, H. J. et al. (2016). „Design trade-off and proof of concept for LOUPE, the Lunar Observatory for Unresolved Polarimetry of Earth." In: *Optics Express* 24, p. 21435. DOI: 10.1364/OE.24.021435.

Howard, A. W. et al. (2012). „Planet Occurrence within 0.25 AU of Solar-type Stars from Kepler." In: *ApJ* 201, 15, p. 15. DOI: 10.1088/0067-0049/201/2/15. arXiv: 1103.2541 [astro-ph.EP].

Huitson, C. M. et al. (2012). „Temperature-pressure profile of the hot Jupiter HD 189733b from HST sodium observations: detection of upper atmo-

spheric heating." In: *MNRAS* 422, pp. 2477–2488. DOI: 10.1111/j.1365-2966.2012.20805.x. arXiv: 1202.4721 [astro-ph.EP].

Ida, S., J. Larwood, and A. Burkert (2000). „Evidence for Early Stellar Encounters in the Orbital Distribution of Edgeworth-Kuiper Belt Objects." In: *ApJ* 528, pp. 351–356. DOI: 10.1086/308179. eprint: astro-ph/9907217.

Jovanovic, N. et al. (2015). „The Subaru Coronagraphic Extreme Adaptive Optics System: Enabling High-Contrast Imaging on Solar-System Scales." In: *PASP* 127, p. 890. DOI: 10.1086/682989. arXiv: 1507.00017 [astro-ph.IM].

Kane, S. R. et al. (2016). „A Catalog of Kepler Habitable Zone Exoplanet Candidates." In: *ApJ* 830, 1, p. 1. DOI: 10.3847/0004-637X/830/1/1. arXiv: 1608.00620 [astro-ph.EP].

Karalidi, T. and D. M. Stam (2012). „Modeled flux and polarization signals of horizontally inhomogeneous exoplanets applied to Earth-like planets." In: *A&A* 546, A56, A56. DOI: 10.1051/0004-6361/201219297. arXiv: 1210.3198 [astro-ph.EP].

Kerr, M. et al. (2015). „Limits on Planet Formation Around Young Pulsars and Implications for Supernova Fallback Disks." In: *ApJ* 809, L11, p. L11. DOI: 10.1088/2041-8205/809/1/L11. arXiv: 1507.06982 [astro-ph.HE].

Kirk, J. et al. (2017). „Rayleigh scattering in the transmission spectrum of HAT-P-18b." In: *MNRAS* 468, pp. 3907–3916. DOI: 10.1093/mnras/stx752. arXiv: 1611.06916 [astro-ph.EP].

Knutson, H. A. et al. (2007). „A map of the day-night contrast of the extrasolar planet HD 189733b." In: *Nature* 447, pp. 183–186. DOI: 10.1038/nature05782. arXiv: 0705.0993.

Knutson, H. A. et al. (2008). „The 3.6-8.0 μm Broadband Emission Spectrum of HD 209458b: Evidence for an Atmospheric Temperature Inversion." In: *ApJ* 673, 526-531, pp. 526–531. DOI: 10.1086/523894. arXiv: 0709.3984.

Kopparapu, R. K. (2013). „A Revised Estimate of the Occurrence Rate of Terrestrial Planets in the Habitable Zones around Kepler M-dwarfs." In: *ApJ* 767, L8, p. L8. DOI: 10.1088/2041-8205/767/1/L8. arXiv: 1303.2649 [astro-ph.EP].

Kopparapu, R. K. et al. (2013). „Habitable Zones around Main-sequence Stars: New Estimates." In: *ApJ* 765, 131, p. 131. DOI: 10.1088/0004-637X/765/2/131. arXiv: 1301.6674 [astro-ph.EP].

Kreidberg, L. et al. (2014). „Clouds in the atmosphere of the super-Earth exoplanet GJ1214b." In: *Nature* 505, pp. 69–72. DOI: 10.1038/nature12888. arXiv: 1401.0022 [astro-ph.EP].

Laughlin, G. and F. C. Adams (1998). „The Modification of Planetary Orbits in Dense Open Clusters." In: *ApJ* 508, pp. L171–L174. DOI: 10.1086/311736.

Lecavelier Des Etangs, A. et al. (2008). „Rayleigh scattering by H_2 in the extrasolar planet HD 209458b." In: *A&A* 485, pp. 865–869. DOI: 10.1051/0004-6361:200809704. arXiv: 0805.0595.

Levison, H. F. et al. (2008). „Origin of the structure of the Kuiper belt during a dynamical instability in the orbits of Uranus and Neptune." In: *Icarus* 196, pp. 258–273. DOI: 10.1016/j.icarus.2007.11.035. arXiv: 0712.0553.

Lockwood, A. C. et al. (2014). „Near-IR Direct Detection of Water Vapor in Tau Boötis b." In: *ApJ* 783, L29, p. L29. DOI: 10.1088/2041-8205/783/2/L29. arXiv: 1402.0846 [astro-ph.EP].

Lovis, C. et al. (2017). „Atmospheric characterization of Proxima b by coupling the SPHERE high-contrast imager to the ESPRESSO spectrograph." In: *A&A* 599, A16, A16. DOI: 10.1051/0004-6361/201629682. arXiv: 1609.03082 [astro-ph.EP].

Luger, R. et al. (2017). „The Pale Green Dot: A Method to Characterize Proxima Centauri b Using Exo-Aurorae." In: *ApJ* 837, 63, p. 63. DOI: 10.3847/1538-4357/aa6040. arXiv: 1609.09075 [astro-ph.EP].

Machalek, P. et al. (2008). „Thermal Emission of Exoplanet XO-1b." In: *ApJ* 684, 1427-1432, pp. 1427–1432. DOI: 10.1086/590140. arXiv: 0805.2418.

Madhusudhan, N., M. A. Amin, and G. M. Kennedy (2014). „Toward Chemical Constraints on Hot Jupiter Migration." In: *ApJ* 794, L12, p. L12. DOI: 10.1088/2041-8205/794/1/L12. arXiv: 1408.3668 [astro-ph.EP].

Madhusudhan, N. et al. (2011). „A high C/O ratio and weak thermal inversion in the atmosphere of exoplanet WASP-12b." In: *Nature* 469, pp. 64–67. DOI: 10.1038/nature09602. arXiv: 1012.1603 [astro-ph.EP].

Martz Jr., E. P. (1934). „Venus and life." In: *Popular Astronomy* 42, p. 165.

Mawet, D. et al. (2017). „Observing Exoplanets with High-dispersion Coronagraphy. II. Demonstration of an Active Single-mode Fiber Injection Unit." In: *ApJ* 838, 92, p. 92. DOI: 10.3847/1538-4357/aa647f. arXiv: 1703.00583 [astro-ph.EP].

Mayer, C. H., T. P. McCullough, and R. M. Sloanaker (1958). „Observations of Venus at 3.15-CM Wave Length." In: *ApJ* 127, p. 1. DOI: 10.1086/146433.

Mayor, M. and D. Queloz (1995). „A Jupiter-mass companion to a solar-type star." In: *Nature* 378, pp. 355–359. DOI: 10.1038/378355a0.

Menzel, D. H. and F. L. Whipple (1954). „The case for H2O clouds on Venus." In: *AJ* 59, p. 329. DOI: 10.1086/107037.

Miller, M. C. and D. P. Hamilton (2001). „Implications of the PSR 1257+12 Planetary System for Isolated Millisecond Pulsars." In: *ApJ* 550, pp. 863–870. DOI: 10.1086/319813. eprint: astro-ph/0012042.

Mulders, G. D. et al. (2016). „A Super-solar Metallicity for Stars with Hot Rocky Exoplanets." In: *AJ* 152, 187, p. 187. DOI: 10.3847/0004-6256/152/6/187. arXiv: 1609.05898 [astro-ph.EP].

Nikolov, N. et al. (2014). „Hubble Space Telescope hot Jupiter transmission spectral survey: a detection of Na and strong optical absorption in HAT-P-1b." In: *MNRAS* 437, pp. 46–66. DOI: 10.1093/mnras/stt1859. arXiv: 1310.0083 [astro-ph.SR].

Öberg, K. I., R. Murray-Clay, and E. A. Bergin (2011). „The Effects of Snowlines on C/O in Planetary Atmospheres." In: *ApJ* 743, L16, p. L16. DOI: 10.1088/2041-8205/743/1/L16. arXiv: 1110.5567.

Owen, J. E. and Y. Wu (2013). „Kepler Planets: A Tale of Evaporation." In: *ApJ* 775, 105, p. 105. DOI: 10.1088/0004-637X/775/2/105. arXiv: 1303.3899 [astro-ph.EP].

Petigura, E. A., A. W. Howard, and G. W. Marcy (2013). „Prevalence of Earth-size planets orbiting Sun-like stars." In: *Proceedings of the National Academy of Science* 110, pp. 19273–19278. DOI: 10.1073/pnas.1319909110. arXiv: 1311.6806 [astro-ph.EP].

Piskorz, D. et al. (2016). „Evidence for the Direct Detection of the Thermal Spectrum of the Non-Transiting Hot Gas Giant HD 88133 b." In: *ApJ* 832, 131, p. 131. DOI: 10.3847/0004-637X/832/2/131. arXiv: 1609.09074 [astro-ph.EP].

Piskorz, D. et al. (2017). „Detection of Water Vapor in the Thermal Spectrum of the Non-transiting Hot Jupiter Upsilon Andromedae b." In: *AJ* 154, 78, p. 78. DOI: 10.3847/1538-3881/aa7dd8. arXiv: 1707.01534 [astro-ph.EP].

Pollack, J. B. et al. (1996). „Formation of the Giant Planets by Concurrent Accretion of Solids and Gas." In: *Icarus* 124, pp. 62–85. DOI: 10.1006/icar.1996.0190.

Pont, F. et al. (2008). „Detection of atmospheric haze on an extrasolar planet: the 0.55-1.05 μm transmission spectrum of HD 189733b with the HubbleSpaceTelescope." In: *MNRAS* 385, pp. 109–118. DOI: 10.1111/j.1365-2966.2008.12852.x. arXiv: 0712.1374.

Poyneer, L. A. et al. (2016). „Performance of the Gemini Planet Imager's adaptive optics system." In: *Ap. Opt.* 55, p. 323. DOI: 10.1364/AO.55.000323.

Rasio, F. A. and E. B. Ford (1996). „Dynamical instabilities and the formation of extrasolar planetary systems." In: *Science* 274, pp. 954–956. DOI: 10.1126/science.274.5289.954.

Richardson, L. J. et al. (2007). „A spectrum of an extrasolar planet." In: *Nature* 445, pp. 892–895. DOI: 10.1038/nature05636. eprint: astro-ph/0702507.

Rousset, G. et al. (2003). „NAOS, the first AO system of the VLT: on-sky performance." In: *Adaptive Optical System Technologies II*. Ed. by P. L. Wizinowich and D. Bonaccini. Vol. 4839. Proc. SPIE, pp. 140–149. DOI: 10.1117/12.459332.

Schneider, J. et al. (2011). „Defining and cataloging exoplanets: the exoplanet.eu database." In: *A&A* 532, A79, A79. DOI: 10.1051/0004-6361/201116713. arXiv: 1106.0586 [astro-ph.EP].

Schwarz, H. et al. (2016). „The slow spin of the young substellar companion GQ Lupi b and its orbital configuration." In: *A&A* 593, A74, A74. DOI: 10.1051/0004-6361/201628908. arXiv: 1607.00012 [astro-ph.EP].

Seager, S. and D. D. Sasselov (2000). „Theoretical Transmission Spectra during Extrasolar Giant Planet Transits." In: *ApJ* 537, pp. 916–921. DOI: 10.1086/309088. eprint: astro-ph/9912241.

Seager, S. et al. (2005). „On the Dayside Thermal Emission of Hot Jupiters." In: *ApJ* 632, pp. 1122–1131. DOI: 10.1086/444411. eprint: astro-ph/0504212.

Silburt, A., E. Gaidos, and Y. Wu (2015). „A Statistical Reconstruction of the Planet Population around Kepler Solar-type Stars." In: *ApJ* 799, 180, p. 180. DOI: 10.1088/0004-637X/799/2/180. arXiv: 1406.6048 [astro-ph.EP].

Sing, D. K. et al. (2008). „Determining Atmospheric Conditions at the Terminator of the Hot Jupiter HD 209458b." In: *ApJ* 686, 667-673, pp. 667–673. DOI: 10.1086/590076. arXiv: 0803.1054.

Sing, D. K. et al. (2009). „Transit spectrophotometry of the exoplanet HD 189733b. I. Searching for water but finding haze with HST NICMOS." In: *A&A* 505, pp. 891–899. DOI: 10.1051/0004-6361/200912776. arXiv: 0907.4991 [astro-ph.EP].

Sing, D. K. et al. (2011). „Gran Telescopio Canarias OSIRIS transiting exoplanet atmospheric survey: detection of potassium in XO-2b from narrowband spectrophotometry." In: *A&A* 527, A73, A73. DOI: 10.1051/0004-6361/201015579. arXiv: 1008.4795 [astro-ph.EP].

Sing, D. K. et al. (2016). „A continuum from clear to cloudy hot-Jupiter exoplanets without primordial water depletion." In: *Nature* 529, pp. 59–62. DOI: 10.1038/nature16068. arXiv: 1512.04341 [astro-ph.EP].

Smith, A. M. S. et al. (2011). „Thermal emission from WASP-33b, the hottest known planet." In: *MNRAS* 416, pp. 2096–2101. DOI: 10.1111/j.1365-2966.2011.19187.x. arXiv: 1101.2432 [astro-ph.EP].

Snellen, I. A. G. et al. (2008). „Ground-based detection of sodium in the transmission spectrum of exoplanet HD 209458b." In: *A&A* 487, pp. 357–362. DOI: 10.1051/0004-6361:200809762. arXiv: 0805.0789.

Snellen, I. A. G. et al. (2010). „The orbital motion, absolute mass and high-altitude winds of exoplanet HD209458b." In: *Nature* 465, pp. 1049–1051. DOI: 10.1038/nature09111. arXiv: 1006.4364 [astro-ph.EP].

Snellen, I. A. G. et al. (2014). „Fast spin of the young extrasolar planet β Pictoris b." In: *Nature* 509, pp. 63–65. DOI: 10.1038/nature13253.

Snellen, I. et al. (2015). „Combining high-dispersion spectroscopy with high contrast imaging: Probing rocky planets around our nearest neighbors." In: *A&A* 576, A59, A59. DOI: 10.1051/0004-6361/201425018. arXiv: 1503.01136 [astro-ph.EP].

Sparks, W. B. and H. C. Ford (2002). „Imaging Spectroscopy for Extrasolar Planet Detection." In: *ApJ* 578, pp. 543–564. DOI: 10.1086/342401. eprint: astro-ph/0209078.

Sparks, W. B. et al. (2009). „Detection of circular polarization in light scattered from photosynthetic microbes." In: *Proceedings of the National Academy*

of Science 106, pp. 7816–7821. DOI: 10.1073/pnas.0810215106. arXiv: 0904.4646 [astro-ph.EP].

Sparks, W. et al. (2012). „Remote sensing of chiral signatures on Mars." In: *Planet. Space Sci.* 72, pp. 111–115. DOI: 10.1016/j.pss.2012.08.010. arXiv: 1209.0671 [astro-ph.EP].

St. John, C. E. and S. B. Nicholson (1922). „The Absence of Oxygen and Water-Vapor Lines in the Spectrum of Venus." In: *ApJ* 56, p. 380. DOI: 10.1086/142712.

Stam, D. M. (2008). „Spectropolarimetric signatures of Earth-like extrasolar planets." In: *A&A* 482, pp. 989–1007. DOI: 10.1051/0004-6361:20078358. arXiv: 0707.3905.

Stam, D. M., J. W. Hovenier, and L. B. F. M. Waters (2004). „Using polarimetry to detect and characterize Jupiter-like extrasolar planets." In: *A&A* 428, pp. 663–672. DOI: 10.1051/0004-6361:20041578.

Stevenson, K. B. et al. (2014). „Deciphering the Atmospheric Composition of WASP-12b: A Comprehensive Analysis of its Dayside Emission." In: *ApJ* 791, 36, p. 36. DOI: 10.1088/0004-637X/791/1/36. arXiv: 1406.7567 [astro-ph.EP].

Thommes, E. W., M. J. Duncan, and H. F. Levison (1999). „The formation of Uranus and Neptune in the Jupiter-Saturn region of the Solar System." In: *Nature* 402, pp. 635–638. DOI: 10.1038/45185.

Tinetti, G. et al. (2007). „Water vapour in the atmosphere of a transiting extrasolar planet." In: *Nature* 448, pp. 169–171. DOI: 10.1038/nature06002.

Todorov, K. O. et al. (2013). „Warm Spitzer Photometry of Three Hot Jupiters: HAT-P-3b, HAT-P-4b and HAT-P-12b." In: *ApJ* 770, 102, p. 102. DOI: 10.1088/0004-637X/770/2/102. arXiv: 1305.0833 [astro-ph.EP].

Tsiganis, K. et al. (2005). „Origin of the orbital architecture of the giant planets of the Solar System." In: *Nature* 435, pp. 459–461. DOI: 10.1038/nature03539.

Vidal-Madjar, A. et al. (2011). „The upper atmosphere of the exoplanet HD 209458b revealed by the sodium D lines: temperature-pressure profile, ionization layer and thermosphere (Corrigendum)." In: *A&A* 533, C4, p. C4. DOI: 10.1051/0004-6361/201015698e. arXiv: 1110.5750 [astro-ph.EP].

Wang, J. et al. (2017). „Observing Exoplanets with High Dispersion Coronagraphy. I. The Scientific Potential of Current and Next-generation Large Ground and Space Telescopes." In: *AJ* 153, 183, p. 183. DOI: 10.3847/1538-3881/aa6474. arXiv: 1703.00582 [astro-ph.EP].

Ward, W. R. (1997). „Protoplanet Migration by Nebula Tides." In: *Icarus* 126, pp. 261–281. DOI: 10.1006/icar.1996.5647.

Weidenschilling, S. J. and F. Marzari (1996). „Gravitational scattering as a possible origin for giant planets at small stellar distances." In: *Nature* 384, pp. 619–621. DOI: 10.1038/384619a0.

Whipple, F. J. W. (1931). „Meteorological conditions on Venus." In: *The Observatory* 54, pp. 86–87.

Wolszczan, A. and D. A. Frail (1992). „A planetary system around the millisecond pulsar PSR1257 + 12." In: *Nature* 355, pp. 145–147. DOI: 10.1038/355145a0.

Zellem, R. T. et al. (2014). „The 4.5 μm Full-orbit Phase Curve of the Hot Jupiter HD 209458b." In: *ApJ* 790, 53, p. 53. DOI: 10.1088/0004-637X/790/1/53. arXiv: 1405.5923 [astro-ph.EP].

Zsom, A. (2015). „A Population-based Habitable Zone Perspective." In: *ApJ* 813, 9, p. 9. DOI: 10.1088/0004-637X/813/1/9. arXiv: 1510.06885 [astro-ph.EP].

2

A SEARCH FOR TIO IN THE OPTICAL HIGH-RESOLUTION TRANSMISSION SPECTRUM OF HD 209458 B: HINDRANCE DUE TO INACCURACIES IN THE LINE DATABASE

The spectral signature of an exoplanet can be separated from the spectrum of its host star using high-resolution spectroscopy. During these observations, the radial component of the planet's orbital velocity changes, resulting in a significant Doppler shift that allows its spectral features to be extracted. In this work, we aim to detect TiO in the optical transmission spectrum of HD 209458 b. Gaseous TiO has been suggested as the cause of the thermal inversion layer invoked to explain the dayside spectrum of this planet. We used archival data from the 8.2-m Subaru Telescope taken with the High Dispersion Spectrograph of a transit of HD 209458 b in 2002. We created model transmission spectra that include absorption by TiO, and cross-correlated them with the residual spectral data after removal of the dominating stellar absorption features. We subsequently co-added the correlation signal in time, taking the change in Doppler shift due to the orbit of the planet into account. We detect no significant cross-correlation signal due to TiO, though artificial injection of our template spectra into the data indicates a sensitivity down to a volume-mixing ratio of $\sim 10^{-10}$. However, cross-correlating the template spectra with a HARPS spectrum of Barnard's star yields only a weak wavelength-dependent correlation, even though Barnard's star is an M4V dwarf that exhibits clear TiO absorption. We infer that the TiO line list poorly matches the real positions of TiO lines at spectral resolutions of $\sim 100,000$. Similar line lists are also used in the PHOENIX and Kurucz stellar atmosphere suites and we show that their synthetic M dwarf spectra also correlate poorly with the HARPS spectra of Barnard's star and five other M dwarfs. We conclude that the lack of an accurate TiO line list is currently critically hampering this high-resolution retrieval technique.

Hoeijmakers, de Kok, Snellen et al.
A&A, **575**, A20 (2015)

2.1 INTRODUCTION

Recently, carbon monoxide has been identified in the transmission spectrum of the exoplanet HD 209458 b (Snellen et al., 2010). During transit, the radial velocity of the hot Jupiter changes by a few tens of $\mathrm{km\,s^{-1}}$, resulting in a changing Doppler shift that is measurable at a resolution of $R \sim 10^5$. This time variation of the planet's spectral signature provides a powerful tool to distinguish between the planet and the overwhelmingly bright host star, because the absorption features in the stellar spectrum are quasi-invariant on these time scales (see Figure 2.1). Furthermore, because the orbital period of the planet is well known, its radial velocity is known at all times and so the Doppler shift of the planets' absorption features can be targeted specifically.

This technique has also been successfully applied in other parts of the orbit, where direct thermal emission of the planet is probed. Absorption in the dayside spectra of both transiting and non-transiting hot Jupiters has been observed: CO and H_2O absorption in the atmospheres of τ Boötes b, HD 189733 b, 51 Peg b and HD 179733 b (Birkby et al., 2013; Brogi et al., 2012; Brogi et al., 2013; Brogi et al., 2014; de Kok et al., 2013; Lockwood et al., 2014; Rodler et al., 2013). In the case of the non-transiting planets, this has allowed for their previously unknown orbital inclinations to be determined as $44.5° \pm 1.5°$ for τ Boötes b (Brogi et al., 2012), which is consistent with the measurement of Rodler et al. (2012), $79.6° - 82.2°$ for 51 Peg b (Brogi et al., 2013), and $67.7° \pm 4.3°$ for HD 179733 b (Brogi et al., 2014), which in turn lead to a determination of their masses.

HD 209458 b is a well-studied exoplanet. It orbits a solar-type star once every 3.5 days and is located 47 pc from the Sun (see Table 2.1 for the physical properties of the system). Using the Spitzer Space Telescope Knutson et al. (2008) found evidence for H_2O emission in the IRAC bands at 4.5 μm and 5.8 μm, which is indicative of a thermal inversion layer in the atmosphere of the planet. A temperature inversion is caused by the absorption of incident starlight in a high-altitude layer of the atmosphere. On Earth, solar UV radiation is absorbed in the oxygen-ozone cycle, effectively absorbing all sunlight short of 350 nm, heating the atmosphere and forming the stratosphere between 10 and 50 km altitude (see e.g. Portmann et al., 2007, and references therein). In the atmospheres of hot Jupiters, similar processes may occur, albeit in different chemical environments.

A number of compounds have been proposed to be capable of causing the inversion layer in the atmosphere of HD 209458 b, one of which is TiO (Hubeny et al., 2003; Burrows et al., 2007), a diatomic molecule that is known to cause major absorption features throughout the optical and near-infrared spectra of M dwarfs. An atmosphere containing a strong optical absorber like TiO would furthermore be consistent with HD 209458 b's low albedo (Rowe et al., 2006). Désert et al. (2008) report a tentative detection of TiO absorption

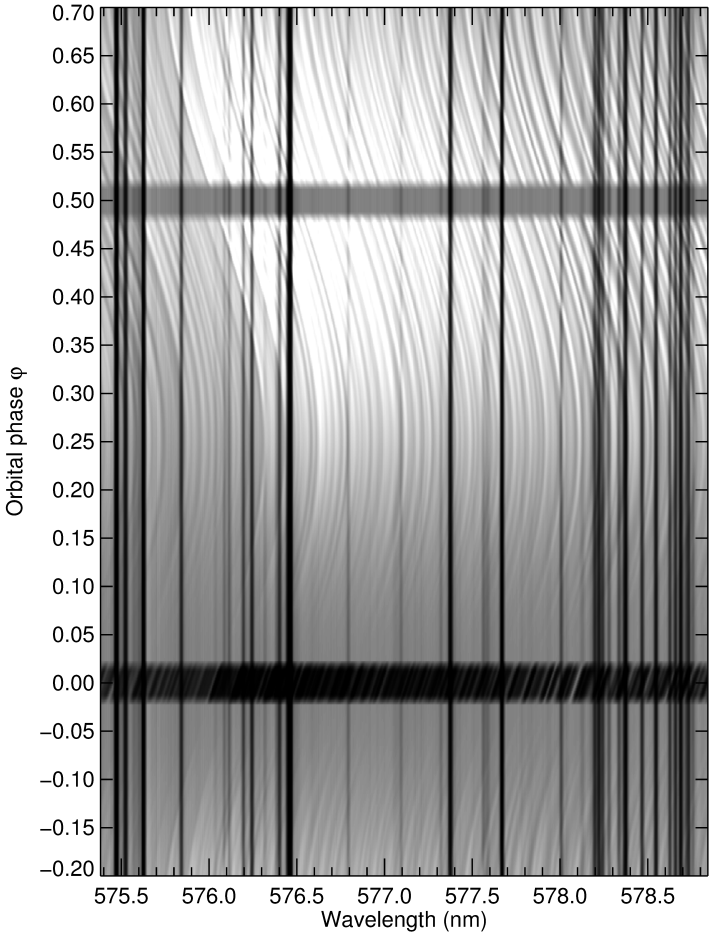

Figure 2.1: Toy model of the phase-dependent Doppler shift of TiO lines along the orbit of HD 209458 b. The white curves represent TiO-emission features owing to the inversion layer (greatly enhanced for visual purposes). During transit around $\phi = 0$, TiO produces slanted absorption lines (black). The black vertical lines are stellar absorption lines, which are stable in time. This difference in the behaviour of stellar and planetary features provides a means of contrast between star and planet.

in the transmission spectrum of HD 209458 b, though more recent broadband studies seem to support a lack of TiO absorption in the transmission spectra of other hot Jupiters (see e.g. Huitson et al., 2013; Sing et al., 2013; Gibson et al., 2013; Bento et al., 2014). Also, models of hot Jupiter atmospheres suggest that maintaining a significant gaseous TiO concentration at high altitudes is difficult because of the condensation of TiO either at depth or on the night side (Spiegel et al., 2009; Burrows et al., 2009; Fortney et al., 2010; Parmentier et al., 2013). More recent observations of the day-side emission spectrum of HD 209458 b, call the existence of the inversion layer into question (Zellem et al., 2014; Diamond-Lowe et al., 2014). Interestingly, Stevenson et al. (2014) observed molecular absorption features in the near-infrared dayside spectrum of Wasp-12b, possibly attributable to TiO. This contrasts with the optical transmission spectra of the same planet, as put forth by Sing et al. (2013). Thus, it is as yet unclear whether TiO is an important chemical component of hot Jupiter atmospheres.

In this study we apply a cross-correlation-based retrieval method to search for TiO in the transmission spectrum of HD 209458 b at high spectral resolution. Section 2.2 describes our dataset and the application of the method. Section 2.3 discusses our results, followed by our conclusions in Section 2.4.

2.2 OBSERVATIONS AND DATA REDUCTION

2.2.1 *Subaru data of HD 209458*

The data used in this analysis were taken on October 25, 2002 using the High Dispersion Spectrograph (HDS) on the Subaru 8.2-m telescope. The observations were performed by Narita et al. (2005) and were originally aimed at detecting absorption of sodium and a number of other atomic species in the transmission spectrum of HD 209458 b. These were later used by Snellen et al. (2008) who did indeed detect sodium. The data consist of 31 exposures with a mean exposure time of 500 sec and cover one 3h transit, plus 1.5h and 0.5h of baseline before and after, respectively. The spectrum is observed over 20 echelle orders, covering a wavelength range between 554 nm and 682 nm at a spectral resolution of $R \sim 45,000$ (6.7 km s^{-1} resolution). Each spectral order is sampled at 0.9 km s^{-1} per pixel over 4100 pixels. The basic data reduction (such as bias subtraction, flat fielding and 1D spectral extraction) were performed by Snellen et al. (2008) and are described therein in detail.

2.2.2 *HARPS data of M dwarfs*

Our analysis relies on cross-correlating the transmission spectra of HD 209458 b with high-resolution template spectra of TiO-bearing models of HD 209458

Parameter	Symbol	Value
Visible magnitude	V	7.67 ± 0.01
Distance (pc)	d	47.4 ± 1.6
Effective temperature (K)	T_{eff}	6065 ± 50
Luminosity ($L_\odot$)	L_*	$1.622^{+0.097}_{-0.10}$
Mass ($M_\odot$)	M_*	1.119 ± 0.033
Radius ($R_\odot$)	R_*	$1.155^{+0.014}_{-0.016}$
Systemic velocity (kms^{-1})[a]	γ	-14.7652 ± 0.0016
Metallicity (dex)	[F/H]	0.00 ± 0.05
Age (Gyr)		$3.1^{+0.8}_{-0.7}$
Orbital period (days)[b]	P	3.52474859
		± 0.00000038
Semi-major axis (AU)	a	$0.04707^{+0.00046}_{-0.00047}$
Inclination (deg)	i	86.71 ± 0.05
Eccentricity[c]	$e \cos \omega$	0.00004 ± 0.00033
Impact parameter	b	0.507 ± 0.005
Transit central time (HJD)[b]	t_c	$2,452,826.628521$
		± 0.000087
Transit duration (min)[d]	t_T	183.89 ± 3.17
Mass (M_J)	M_p	$0.685^{+0.015}_{-0.014}$
Radius (R_J)	R_p	$1.359^{+0.016}_{-0.019}$
Density (g cm^{-3})	ρ_p	$0.338^{+0.016}_{-0.014}$
Equilibrium temperature (K)	T_{eq}	1449 ± 12

Table 2.1: Properties of HD 209458 (upper part) and HD 209458 b (lower part), adopted from Torres et al. (2008).
a : Adopted from Mazeh et al. (2000).
b : Adopted from Knutson et al. (2007).
c : Adopted from Crossfield et al. (2012).
d : Adopted from the Exoplanet Orbit Database (Wright et al., 2011).

Name	Spectral type	PID (ESO)	PI
Proxima Centauri	M6.0V	183.C-0437(A)	Bonfils
GJ402	M5.0V	183.C-0437(A)	Bonfils
GJ9066	M4.5V	072.C-0488(E)	Mayor
GJ876	M5.0V	183.C-0437(A)	Bonfils
Barnard's star	M4.0V	072.C-0488(E)	Mayor

Table 2.2: Overview of the archival M dwarf spectra used in this work, obtained using the HARPS-south instrument.

b's absorption spectrum which rely on line lists published by Freedman et al. (2008, see sections 2.2.3 and 2.2.4). The optical spectra of M dwarfs are dominated by TiO absorption features and are therefore natural benchmarks against which we tested the accuracy of these TiO templates. Many nearby M dwarfs have been observed extensively at high spectral resolution in order to detect the radial velocity signature induced by potential orbiting companions. We downloaded high-resolution spectra of five different M dwarfs from the ESO data archive. These spectra were obtained by the HARPS spectrograph at ESO's 3.6m La Silla telescope, between 500 nm and 691 nm at resolutions of $R = 115,000$. Information about the five stars is shown in Table 2.2. Barnard's star is used throughout this work as the primary example, and is shown in the top panel of Figure 2.2 before the removal of all broadband features using a high-pass filter (the spectra of the other M dwarfs were filtered in the same way), and after correcting for its radial velocity of -110.51 km s^{-1} (Nidever et al., 2002).

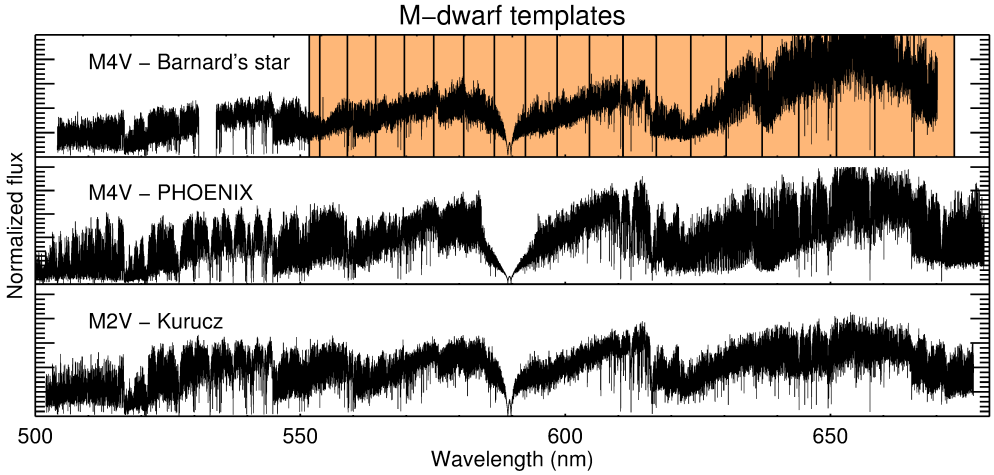

Figure 2.2: Top panel: Archival HARPS spectrum of Barnard's star at a resolution of $R = 115,000$. Middle panel: A PHOENIX model of a generic M4V dwarf. Bottom panel: Kurucz model of Gliese 411, a standard M2V dwarf. These three templates contain strong broadband features, which are removed by applying a high-pass filter later in the analysis (not shown). The orange region in the top panel covers the approximate extent of the spectral orders of the HDS Subaru dataset, which are delimited by the solid vertical lines.

2.2.3 *Post-processing and cross-correlation*

The analysis of the high dispersion transmission spectra of HD 209458 b differs at several points from that of infrared data used in previous high-dispersion spectroscopy studies by our group (see Birkby et al., 2013; Brogi et al., 2012; Brogi et al., 2013; Brogi et al., 2014; de Kok et al., 2013), which are dominated by time-dependent telluric absorption features, mainly due to variations in airmass. In the optical, the atmosphere presents no significant absorption features except in some specific wavelength ranges. Rather, the spectrum is dominated by stellar absorption lines. Assuming that the stellar spectrum is stable during the transit, it can be removed by dividing each of the individual spectra in the time series with the time-averaged stellar spectrum. In principle, this operation does not affect the planet signal because it significantly shifts in wavelength during the observations owing to the change in the radial component of the orbital velocity during transit (from -15 km s^{-1} to $+15$ km s^{-1}).

The full sequence of processing steps is summarized below. Intermediate data products are shown in Figure 2.3.

1 **Broadband removal and normalization:** To remove strong broadband components such as the stellar continuum and the spectrograph's blaze function, the brightest exposure of each spectral order was divided into 50 wavelength regions. A seventh order polynomial was fit through the maximum of each part to obtain the continuum level. This fit was removed from all other exposures through division, removing the strongest broadband features. Subsequently, the continuum of each of the exposures was obtained by dividing each exposure into the same 50 regions as above and again finding the maximum of each part. These continua were interpolated, and removed through division. This acts to remove residual broad-band variations not removed by the seventh-order polynomial fit, and normalizes the continuum of each exposure to unity. At this stage there were still significant residual broad-band variations, which were removed at a later stage (see step 7).

2 **Alignment of spectra:** The spectra slowly drift in wavelength because of both the change in radial velocity of the observatory during the observations and instrumental instability. These misalignments are approximately a pixel and would adversely affect the removal of the time-average stellar spectrum if left untreated. In each spectral order, a dozen strong stellar absorption lines were identified by eye. To these lines in each of the 31 exposures, Gaussian profiles were fitted to obtain the position of each line centre. A linear fit through the misalignments of the different absorption lines was used to align the spectra to a common reference frame (a higher order fit was not warranted because the scatter in the determination of the line centroids was too high to identify higher order components).

3 **Wavelength solution:** Because HD 209458 is a close solar analogue, we matched our time-averaged spectrum (see next step) of the HD 209458 system to a model solar spectrum (adopted from the Kurucz stellar atmosphere atlas) in a step-wise fashion. The strongest stellar absorption lines were identified and matched by eye. This produced a crude wavelength solution that was subsequently used to identify 30 - 40 less prominent lines in each order. We subsequently fitted Gaussian profiles to the cores of these lines in both the data and the solar template, producing a wavelength solution with a standard deviation of 1.7×10^{-3} nm $\pm$ 0.7×10^{-3}, corresponding to 0.83 ± 0.36 km s^{-1} or $\sim$ 12% of the spectral resolution. Because the solar spectrum is synthesized at rest, the wavelength solution is calibrated to the rest frame of HD 209458, so the mean radial velocity with respect to the observatory on Earth is automatically corrected for. Any time-dependent Doppler shifts had already been corrected in step 2. Therefore, each exposure is now in the rest frame of the host star.

4 **Removal of stellar spectrum:** Each pixel in each spectral order was time-averaged by taking the median of the aligned spectra, which corresponds to taking the median of each of the columns of the array in panel 2 of Figure 2.3. This average contains all time-constant stellar features, but only a small part of the time-varying planet signal, since it is shifted to a different column in each exposure. It is removed from each exposure through division. The width of planetary absorption lines is limited to 6.7 km s^{-1}, which is the resolution of the instrument. Between exposures, the planet signal is shifted by $\sim$ 1.8 km s^{-1}. Therefore, the planet signal is present in no more than four exposures per pixel column. These four exposures are part of a median with 27 other exposures that do not contain the planet signal. Therefore, we expect that up to $10\% - 15\%$ of the planet signal is removed along with the median stellar spectrum. This is not important for the rest of the analysis, because we measure the significance of any TiO detection by our ability to retrieve injected model spectra, which suffer in the same way from this degradation (see section 2.3).

5 **Removal of bad pixels and cosmics:** The resulting residuals contain bad pixels and cosmic rays. All pixels deviating by more than 4σ from the mean were reset to the mean, removing all significant bad pixels and cosmic rays. As a result, 0.21% of all pixel values were affected.

6 **Normalization by signal to noise:** The noise in the residual spectrum varies with pixel position owing to the presence of deep stellar absorption lines up until step 4. We divide each pixel in the residual spectrum by the variance of that pixel value (variance of each column of panel 3, Figure 2.2.3) to weigh down such pixels. Low S/R regions would otherwise add a significant amount of noise to the cross-correlation function.

7 **Suppression of broadband residuals:** The residuals feature broadband variations due to imperfect removal of instrumental effects and broad stellar lines. Latent broadband variations were characterized by smoothing each exposure with a Gaussian with a width of 40px (36 km s^{-1},) and were divided out of the data. The last panel of Figure 2.3 shows the residual of this final processing step, before the cross-correlation is performed.

8 **Cross-correlation:** The planet's potential absorption features were extracted by cross-correlating the residual spectra with template spectra of TiO (see section 2.2.4) across the full wavelength range of the data, so between $\sim$ 554 and $\sim$ 682 nm. The templates were Doppler-shifted to velocities ranging between $\pm$150 km s^{-1} relative to the star, in steps of 1 km s^{-1} (which roughly corresponds to the sampling rate of the data,

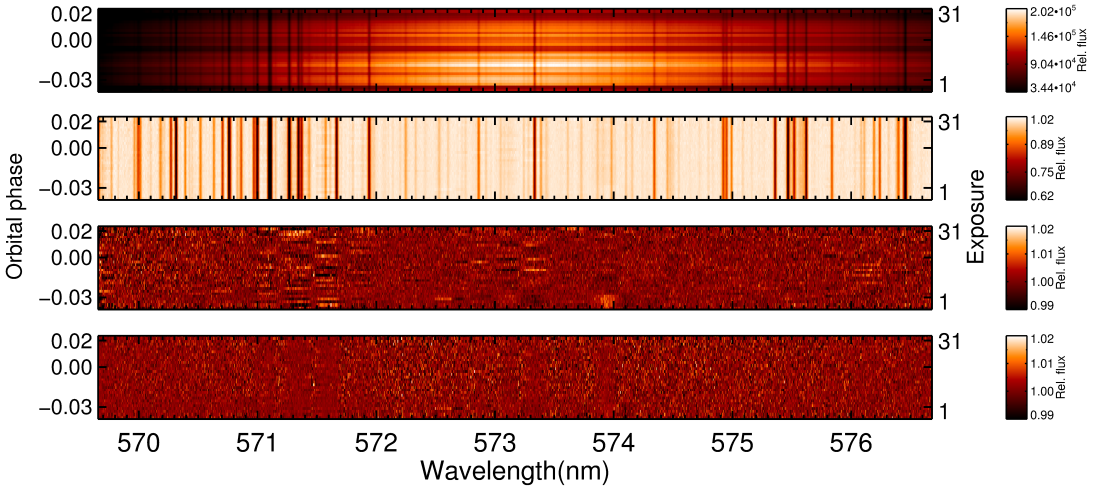

Figure 2.3: Major post processing steps of echelle order 17 before cross-correlation. The top panel shows the initial state of the spectral order, arranged such that all exposures in this order are stacked vertically. The result of the removal of the blaze pattern and the alignment of the individual exposures (which cannot be seen by eye because the misalignments are on a sub-pixel level) is shown in the second panel. The third panel shows the residuals after dividing through the time-averaged spectrum (i.e. the average of the spectrum obtained by averaging each column in the second panel). The fourth panel shows the same residuals after removing 4σ outliers, removing latent broadband features and weighing down noisy columns. The average standard deviation of the residuals at this stage is 0.45%. Only the lower two panels are scaled to the same colour range.

0.9 km s^{-1} per pixel). At the Doppler shift equal to the radial velocity of the planet, the cross-correlation effectively co-adds all of the individual absorption lines of the molecule.

2.2.4 *Model spectra*

For the purpose of applying the cross-correlation method to the case of TiO in the atmosphere of HD 209458 b (see below), we generated several model transmission spectra of atmospheres containing various concentrations of TiO, at a sampling resolution of $R = 240,000$. The line database stems from Freedman et al. (2008), who present a modified line list based on the one published by Schwenke (1998). The model atmosphere has a temperature-pressure profile as shown in Figure 2.4, and includes H_2 scattering and molecular absorption due to TiO with volume mixing ratios (VMR) of 10^{-7}, 10^{-8},

10^{-9}, 10^{-10} and 10^{-11}. The solar photospheric abundance of titanium is $10^{-7.1}$ (Asplund et al., 2006), so the transmission spectrum of TiO is modelled between ~ 1 and $\sim 10^{-4}$ times the solar abundance of Ti. These mixing ratios were assumed to be uniform throughout the atmosphere. As such, no chemistry, phase changes or dynamics were taken into account. The atmosphere was assumed to have a temperature inversion as displayed in the right-hand panel of Figure 2.4 (adopted from Burrows et al., 2007), but because the background continuum originates in a star with an effective temperature of 6065 K, the assumption of a particular T-P-profile does not significantly influence the template spectrum. To confirm the robustness of the template to a temperature mismatch, we also modelled a TiO-bearing atmosphere at a constant temperature of 3000 K and cross-correlated it with the template shown in Figure 2.4. The result is shown in Figure 2.6, and discussed in more detail in section 2.3.1.

For benchmark purposes (see section 2.2.2), we also cross-correlated with synthetic M dwarf spectra originating in the Kurucz and PHOENIX stellar atmosphere model suites which necessarily include models of the TiO molecule. Both models use a line list calculated by Plez (1998). The Kurucz model is a template spectrum of the M2V dwarf GL411 at a resolution of $R = 100,000$ (Castelli et al., 2003) and the PHOENIX model, a template of a generic M4V dwarf ($T_{eff} = 3100$K, $\log g = 5.0$, $Fe/H = +0.5$, obtained from the PHOENIX online database as presented by Husser et al. (2013)) at a resolution of $R = 125,000$. They are shown together with the HARPS spectrum of Barnard's star in Figure 2.2.

2.3 RESULTS AND DISCUSSION

The left-hand panels of Figure 2.5 show the correlations between the HDS spectra of HD 209458 b and our TiO template at five modelled VMRs (see section 2.2.4). The correlation coefficients are plotted as a function of the radial velocity to which the template is shifted (horizontal axis) for every individual exposure (i.e. time, vertical axis).

To assess the ability of the cross-correlation procedure to retrieve the template spectra from real data, we inject the templates into the data prior to cross-correlation using the known orbital velocity of HD 209458 b, between steps 3 and 4 in section 2.2.3, similar to Snellen et al. (2010). Prior to injection, we convolve the template with a Gaussian to match the spectral resolution of the data $(45,000)$, and convolve again with a box function to account for the widening of the planetary absorption lines due to the changing Doppler shift during the 500s exposures. This gives rise to the middle panels in Figure 2.5. Injection of a TiO-bearing template at a VMR greater than 10^{-10} clearly pro-

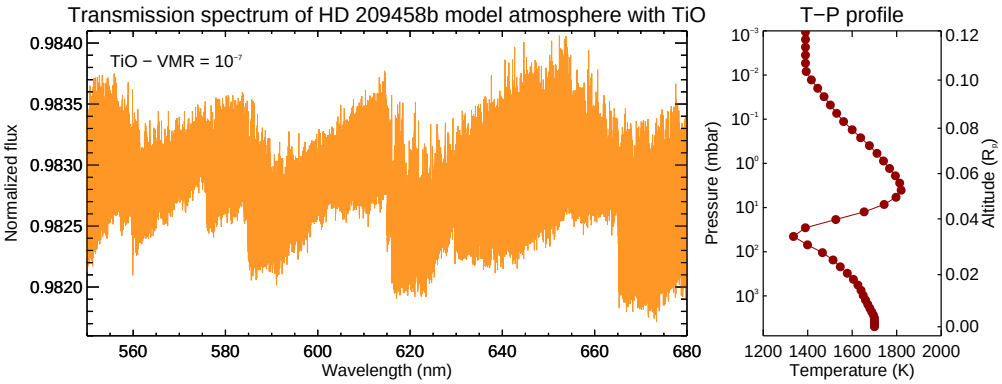

Figure 2.4: Left panel: one of our model absorption spectra of HD 209458 b containing TiO at a VMR of 10^{-7}, normalized to the brightness of the system out of transit and according to the temperature-pressure profile shown on the right, along with the corresponding altitude in units of the planet radius. Throughout this work, we employ this spectrum as a template in various cross-correlation analyses, as well as four similar templates at lower VMRs; and one template at a constant temperature of 3000 K. Note that the form of the assumed T-P profile does not significantly impact the correlation because the effective temperature of the star is ~ 6065 K.

duces a slanted feature, whose gradient is a measure of the orbital velocity of the planet at which the template was injected.

Given that the radial velocity of the planet is known at all times, each exposure (i.e. row in Figure 2.5) can be shifted to the rest frame of the planet. This allows for co-addition of all exposures, the result of which is shown in the right-hand panels in Figure 2.5. The S/N of the observed correlation peak is indicative of the significance at which the template would be retrieved, had it been identically present in the residuals. Evidently, the peak correlation strength decreases with decreasing VMR, hence the VMR at which the correlation peaks at the 3σ level, which we consider to be the theoretical limiting VMR at which TiO would be retrievable by applying the current analysis on this data.

It is clear from the left-hand panels of Figure 2.5 that the residuals do not correlate with our TiO templates. This non-detection is significant down to VMRs of 10^{-10}, as shown by the successful retrieval of our templates after having artificially injected them into the data. This sensitivity limit corresponds to 10^{-3} times the solar abundance of Ti (Asplund et al., 2006). The models of the atmosphere of HD 209458 b are greatly simplified approximations of the real physical environment. The assumption of a uniform VMR across the entire atmosphere is especially questionable, because the atmosphere is not expected to be homogeneous. However, by extending the ab-

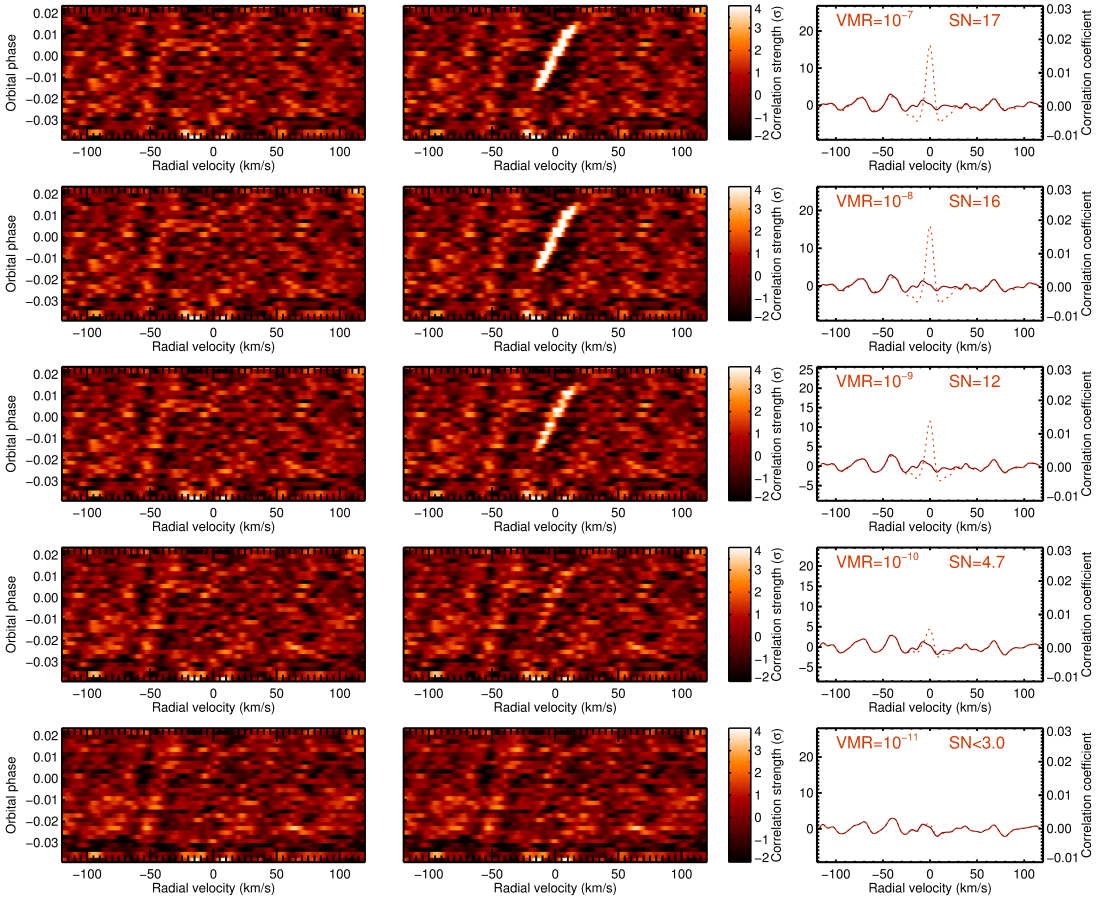

Figure 2.5: Strength of the cross-correlation signature as a function of radial velocity and orbital phase. Each row of panels shows the cross-correlation with model atmospheres with different VMR's of TiO (left panels, ranging from 10^{-7} (top) to 10^{-11} (bottom) by factors of 10). The models are also injected into the data prior to cross-correlation (middle panels) to probe the sensitivity of the procedure. Co-addition of all exposures (right panels) is achieved by shifting each exposure (i.e. each row in the middle and left panels) to the rest-frame of the planet and averaging them in time. The dashed lines are the co-added correlation strength of the residuals, after having injected them with the model template with which the cross-correlation is performed. The solid lines are the co-added correlation strengths of the residuals without prior injection of the template. The S/N of the correlation peak is calculated by taking the peak correlation, and dividing it through the standard deviation of the cross-correlation response, excluding a range of ± 20 km s^{-1} in which the correlation peak itself resides. Clearly, the presence of TiO would be convincingly retrieved at the ppb level, provided that the line database is accurate.

sorbing TiO layer uniformly throughout the atmosphere, the TiO absorption at that VMR is maximized. The limiting VMR of 10^{-10} is therefore a true lower limit: If TiO were only present at a VMR of 10^{-10} in parts of the atmosphere, it would not be retrieved in this analysis.

Before invoking a plethora of reasons for this non-detection of TiO that include hazes, obscuring clouds, screening by other species, cold-traps or destructive chemistry, it should be noted that the sensitivity of the cross-correlation procedure critically depends on the accuracy of the line positions in the template spectrum. If the wavelength positions of the lines are inaccurate, the cross-correlation procedure may not add their contributions constructively. As shown below, this is a real concern.

2.3.1 *Evaluation of template spectra*

Because TiO absorption visibly dominates M dwarf optical spectra, a high-resolution optical spectrum of Barnard's star can be used to test the accuracy of our TiO template. Their mutual correlation should be very clear.

Figure 2.6 shows the cross-correlation between our TiO template at different temperatures, the stellar atmosphere models and the HARPS-spectrum of Barnard's star. The TiO-bearing model of HD 209458 b (VMR=10^{-7}, T-P profile as shown in Figure 2.4) shows a correlation peak of 0.35 with the stellar atmosphere models. The cross-correlation between our TiO templates at 3000 K and $\sim$ 1500 K peaks at 0.9. M dwarf transmission spectra feature a host of other optical absorbers, which decrease the correlation between an M dwarf spectrum and a pure-TiO template. We regard this as the main reason for the poor correlation between our TiO template and the stellar atmosphere models, rather than a mismatch of the T-P profile associated with the template.

In contrast to the stellar atmosphere models, a marginal correlation peak of only 0.1 is observed between the TiO template and the HARPS spectrum. From this we may conclude that our TiO-bearing model spectra do not accurately reproduce real-world TiO absorption at high resolution.

To test the extent to which stellar atmosphere models and real M dwarf spectra match each other at high resolution, we cross-correlated Barnard's star's spectrum with the spectra of five other M dwarfs and with the PHOENIX M4V model. This is shown in Figure 2.7. Regardless of differences in effective temperature, metallicity, and S/N, real M dwarf spectra correlate strongly with each other; with a peak of >0.75 in all cases. However, as is the case with the TiO template, the PHOENIX model correlates at less than 0.15 with all of the M dwarf spectra. This strengthens our conclusion that the modelled spectrum of TiO is not representative of real TiO. The high correlation between the TiO template and the PHOENIX and Kurucz models, suggests

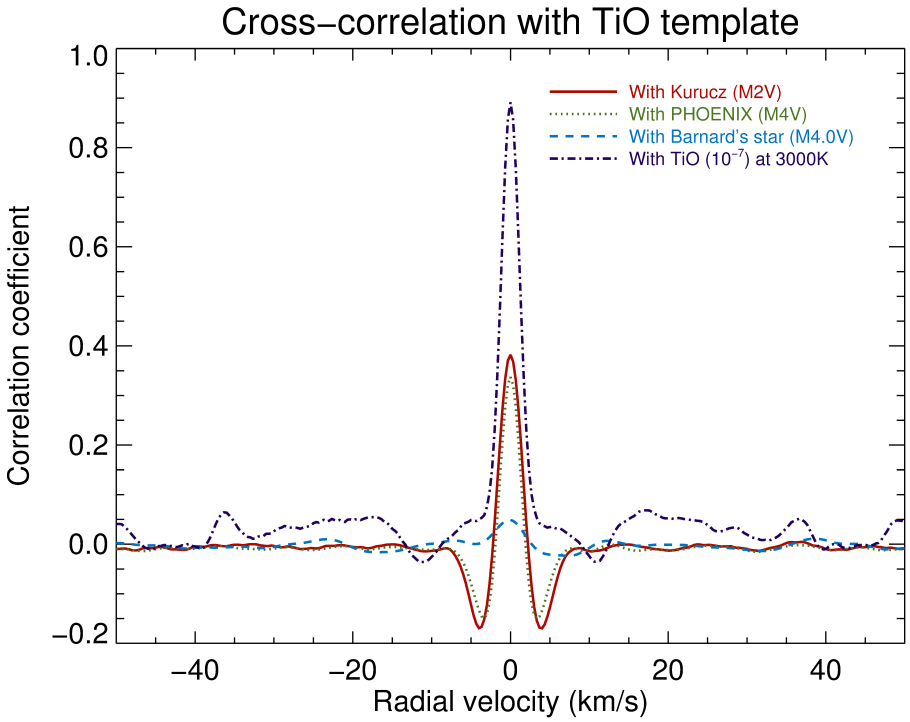

Figure 2.6: Correlation of our TiO template (at T ~ 1500 K), as shown in Figure 2.4, with the PHOENIX M4V model (green), the Kurucz model of GL411 (red), Barnard's star's optical spectrum (light blue) and the TiO template modelled at a temperature of 3000 K (dark blue). All modelled spectra correlate strongly with our TiO template, while Barnard's star's spectrum does not. The high peak correlation between the two templates at different temperatures suggests that the assumption of an inaccurate T-P profile has little effect on the templates.

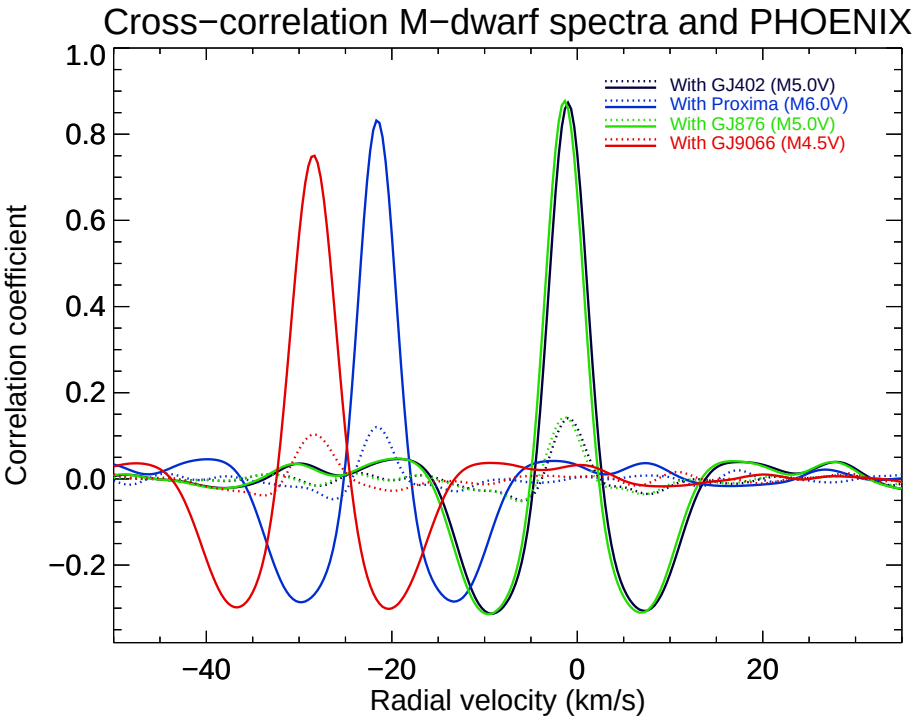

Figure 2.7: Correlation of several M dwarf spectra (see Table 2.2) with Barnard's star (solid lines) and with the PHOENIX M4V model (dashed lines). The cross-correlation procedure retrieves the Doppler shifts of the other M dwarfs, since we did not shift these to their own rest frames, for the sake of clarity. All M dwarfs correlate by more than 0.75 with Barnard's star, while correlation with the model absorption spectrum never exceeds 0.15.

that the TiO line lists have a common source, and the same uncertainties in the line positions seem to have persisted in the works of both Plez (1998) and Schwenke (1998). A visual comparison of the models and the spectrum of Barnard's star, shows strong similarity between all three models at high resolution, but a severe mismatch with the HARPS data (Figure 2.8).

Although the TiO models do not match the HARPS data well, our TiO template is able to partially retrieve the presence of TiO in the Barnard's star spectrum. The extent of the inaccuracies of the models, as shown in Figure 2.8 near 530 nm, raises the suspicion that the marginal correlation with Barnard's star is not due to the haphazard alignment of model absorption lines. Instead, it is possible that certain absorption bands are modelled more accurately than others. To test the hypothesis that inaccuracies are only associated with certain absorption bands only, we divide the available 130 nm range of our

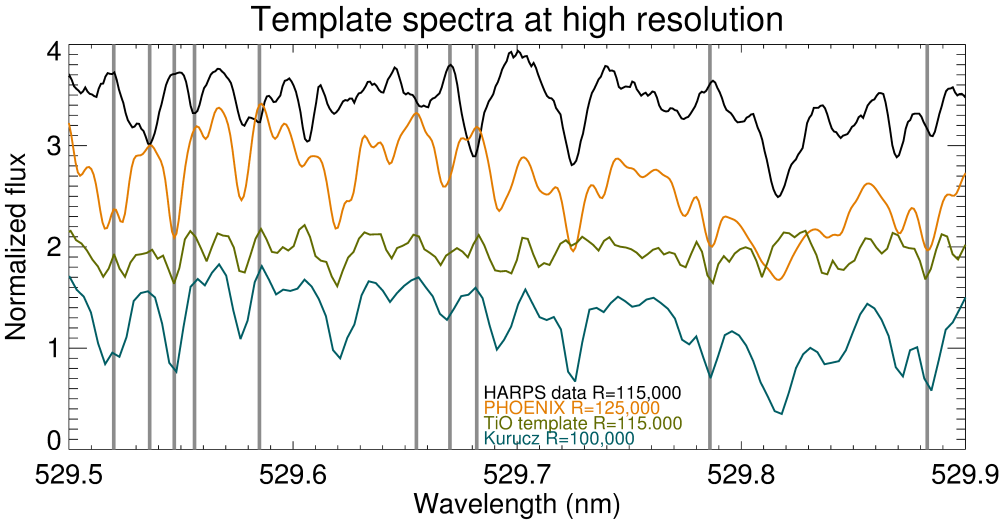

Figure 2.8: Visual comparison of the three TiO-bearing model atmospheres and the HARPS-spectrum of Barnard's star. The spectra are vertically offset for clarity. Although some broad absorption lines of the stellar models seem to line up with the HARPS-data, most narrow-band features (the majority of them are due to TiO) are clearly misplaced. Some obvious mismatches are indicated by the gray vertical lines.

HARPS data into smaller sections and again cross-correlate our model of HD 209458 b with each section separately. The result is shown in Figure 2.9.

Over most of the wavelength range, our model does not correlate with the TiO spectrum. However above 630 nm, the TiO template appears to match the data better, increasing in correlation toward longer wavelengths (a trend that may continue further toward the near infrared). The four sections shown in Figure 2.9 correlate most at slightly different radial velocity shifts (few km/s), meaning that ensembles of lines are collectively offset. This specifically indicates inaccuracies in the calculated values of the energy levels of the TiO molecule.

2.3.2 *Alternative template spectra*

As shown above, the cross-correlation procedure is very sensitive to species with rich optical absorption spectra in the HDS residuals. As for TiO, the sensitivity reaches down to VMRs below the ppb level. Although we have also shown that the line lists that are the basis of our TiO (and others) model spectra display extensive inaccuracies, the template is able to partially retrieve TiO features from Barnard's star's optical spectrum at wavelengths longward of ~ 640 nm and is thus to a certain extent useful for probing the atmosphere of HD 209458 b for the presence of TiO. We therefore cross-correlate the residuals with the TiO template at a VMR of 10^{-7}, using only wavelengths between 640 nm $-$ 682 nm, the result of which is shown in the top row of figure 2.10.

Injecting the template into the residuals like before reveals a theoretical sensitivity of 7.6σ (top right panel of Figure 2.10). However, because the line list is only partially accurate at these wavelengths, this is only an upper limit: That is, if this line list was perfect, the presence of TiO in the atmosphere of HD 209458 b at a volume-mixing ratio of 10^{-7} would have been retrieved with a significance of 7.6σ. Though since the line list suffers from unknown inaccuracies, the true limiting VMR is not determined.

Earlier it was shown (Figure 2.6) that if the temperature-pressure environment of the TiO template does not match that of the data, the correlation is not strongly affected. Therefore, although the temperature of the photosphere of Barnard's star is some 1500K higher than the atmosphere of HD 209458 b in the terminator region, the TiO absorption present in the spectra of M dwarfs may also be useful for identifying TiO absorption in exoplanet atmospheres at high resolution. As shown before (Figure 2.7), the presence of noise in a cross-correlation template does not destroy the cross-correlation at high-resolution, and thus we propose to use the HARPS spectrum of Barnard's star as a template for cross-correlation with the HDS data of HD 209458 b.

Injecting the absorption spectrum of Barnard's star into the residuals of the HDS data does not provide a physically meaningful sensitivity. Although

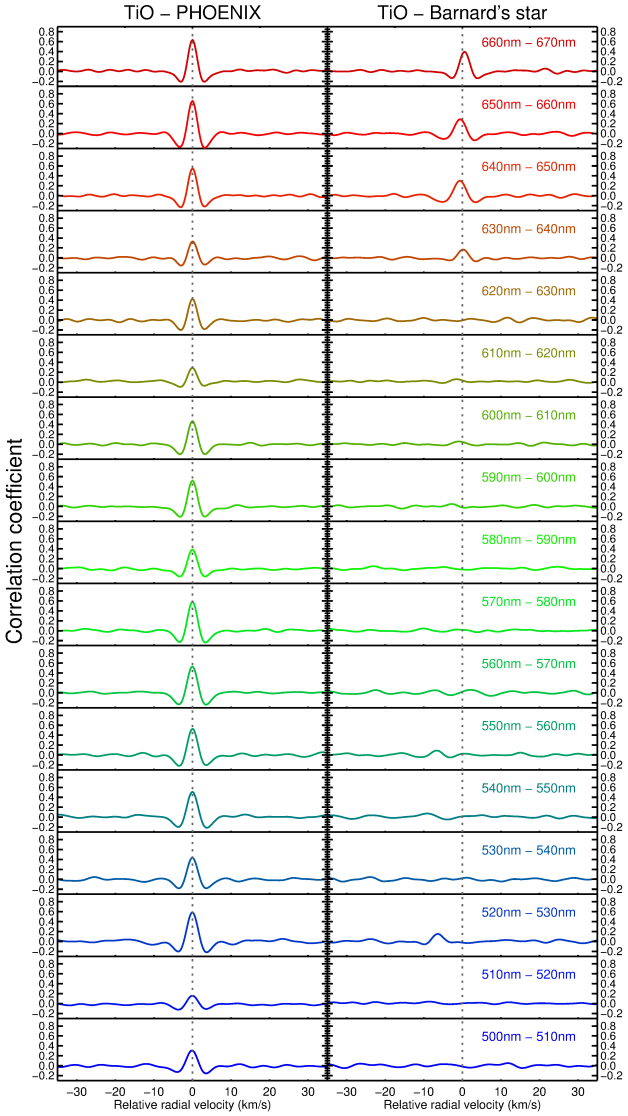

Figure 2.9: Cross-correlation of sections of the TiO template with the PHOENIX model (left column) and with the Barnard's star spectrum (right column), at different wavelengths. The TiO template correlates strongly almost everywhere between 500 nm and 670 nm, while the correlation between the template and the TiO-dominated spectrum of Barnard's star is absent across most of the wavelength range, and less than 0.4 in the best case. We also note that maximum correlation occurs at slightly different radial velocities (an extreme feature is observed between 520 nm and 530 nm). This is explicitly indicative of wavelength-offsets of entire TiO bands (and thus inaccuracies in the determination of the energy levels of the TiO molecule).

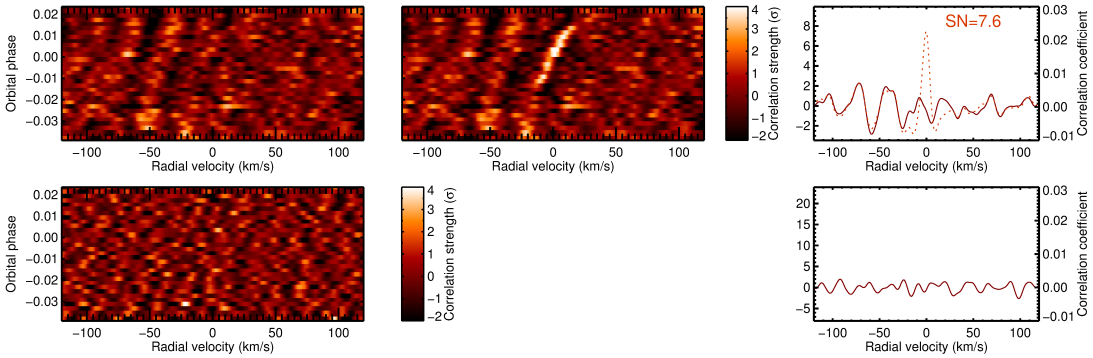

Figure 2.10: Top panels: Correlation coefficients for cross-correlation with the TiO template (VMR $= 10^{-7}$) between 640 nm and 670 nm, with and without injecting the template into the data prior to cross-correlation (middle and left panel, dashed and solid lines respectively). Restricting the wavelength range has reduced the signal-to-noise at which this template is retrieved after injection by over 9σ (compare to Figure 2.5), but it is not clear to what extent persistent inaccuracies still adversely affect the sensitivity of this restricted template. Bottom row: Correlation coefficients for cross-correlation with Barnard's star's optical spectrum. No enhanced correlation is observed. Given that the injection of the stellar absorption spectrum into the planetary transmission spectrum is not physically meaningful, the sensitivity of this non-detection can't straightforwardly be expressed in physical quantities like the limiting VMR.

our template at ~ 1500K correlates significantly with the stellar atmosphere models, the absorption spectrum of an M dwarf is not a good model for the absorption spectrum of the upper atmosphere of HD 209458 b during transit, because the underlying physical parameters are very different. In addition to the different temperature-pressure environments, the presence of other species in an M dwarf's photosphere and the different continuum level (HD 209458 is a solar type star) make it difficult to adjust Barnard's star's absorption spectrum to form a template from which parameters such as the limiting VMR can be derived as before. Extracting a physically meaningful TiO absorption spectrum from real-world absorption spectra of M dwarfs would require more work and is beyond the scope of this study. For now, we only use Barnard's star's spectrum to qualitatively probe for the presence of TiO absorption in the HDS dataset. The resulting cross-correlation is shown in Figure 2.10. Again, no significant correlation is detected.

2.4 CONCLUSION

We have probed the optical transmission spectrum of HD 209458 b for TiO absorption using the time-dependent radial velocity of the planet, which can be spectrally resolved at high resolution. At first glance our null-result seems to in contrast with the possible detection of TiO by Désert et al. (2008) and to be in line with more recent observations of hot Jupiters and models. Injection of model TiO spectra into the data shows that our cross-correlation retrieval method is sensitive to volume-mixing ratios down to 10^{-10}, and is thus theoretically capable of ruling out the presence of TiO at a stringent level.

However, this method relies on the accuracy of template spectra of TiO at resolutions of $R \sim 10^5$. Although such templates are available in the literature, we observe that the line databases used to synthesize these spectra are based on model calculations of the TiO molecule that display widespread inaccuracies. We infer that the energy levels of the TiO molecule are not determined well enough to accurately synthesize absorption spectra at these resolutions. Nonetheless, we have found that the TiO line list used to generate our template spectrum is accurate to some extent at wavelengths between 640 nm and 670 nm and that the spectra of M dwarfs can also serve as cross-correlation templates. However, using a high-resolution spectrum of Barnard's star and restricting our template to the aforementioned wavelength range do not result in a significant correlation. It would therefore seem that the presence of a high concentration of TiO in the upper atmosphere of HD 209458 b in the terminator region is unlikely. However, owing to the uncertainties regarding the physical meaning of these template models, such a conclusion is tentative.

The lack of an accurate TiO line list is thus a critical hindrance to applying this retrieval technique to search for the presence of TiO in the optical trans-

mission spectrum of HD 209458 b. Also, since the TiO molecule is among the best characterized molecules in astrophysics, we suspect that the absorption spectra of less common and more complicated species are likely to be even less accurately characterized. Furthermore, inaccuracies in the calculations of line positions not only severely hinder the application of high-resolution retrieval techniques like the one employed in this work, but they also pervade widely used stellar atmosphere models. Modern-day stellar atmosphere codes apply highly advanced modelling techniques to poor line databases, which is over a decade old in the case of TiO.

Therefore we conclude that an increasing community of observational and theoretical astronomers would benefit from an immediate and extensive effort to improve the quality of the absorption spectra of molecules like TiO, either through more sophisticated theoretical calculations or by means of direct measurements in the laboratory.

ACKNOWLEDGEMENTS

This work is part of the research programmes PEPSci and VICI 639.043.107, which are financed by the Netherlands Organisation for Scientific Research (NWO), and was also supported by the Leiden Observatory Huygens Fellowship. This work was performed in part under contract with the California Institute of Technology (Caltech)/Jet Propulsion Laboratory (JPL) funded by NASA through the Sagan Fellowship Program executed by the NASA Exoplanet Science Institute. Support for this work was provided in part by NASA through Hubble Fellowship grant HST-HF2-51336 awarded by the Space Telescope Science Institute. Also, this research has made use of the Exoplanet Orbit Database and the Exoplanet Data Explorer at exoplanets.org. Finally, we would like to thank Leigh Fetcher, Jaemin Lee and Patrick Irwin for providing the TiO line-list needed to perform this analysis.

BIBLIOGRAPHY

Asplund, M., N. Grevesse, and A. Jacques Sauval (2006). „The solar chemical composition." In: *Nuclear Physics A* 777, pp. 1–4. DOI: 10.1016/j.nuclphysa.2005.06.010. eprint: astro-ph/0410214.

Bento, J. et al. (2014). „Optical transmission photometry of the highly inflated exoplanet WASP-17b." In: *MNRAS* 437, pp. 1511–1518. DOI: 10.1093/mnras/stt1979. arXiv: 1310.3893 [astro-ph.EP].

Birkby, J. L. et al. (2013). „Detection of water absorption in the day side atmosphere of HD 189733 b using ground-based high-resolution spectroscopy at 3.2 μm." In: *MNRAS* 436, pp. L35–L39. DOI: 10.1093/mnrasl/slt107. arXiv: 1307.1133 [astro-ph.EP].

Brogi, M. et al. (2012). „The signature of orbital motion from the dayside of the planet τ Boötis b." In: *Nature* 486, pp. 502–504. DOI: 10.1038/nature11161. arXiv: 1206.6109 [astro-ph.EP].

Brogi, M. et al. (2013). „Detection of Molecular Absorption in the Dayside of Exoplanet 51 Pegasi b?" In: *ApJ* 767, 27, p. 27. DOI: 10.1088/0004-637X/767/1/27. arXiv: 1302.6242 [astro-ph.EP].

Brogi, M. et al. (2014). „Carbon monoxide and water vapor in the atmosphere of the non-transiting exoplanet HD 179949 b." In: *A&A* 565, A124, A124. DOI: 10.1051/0004-6361/201423537. arXiv: 1404.3769 [astro-ph.EP].

Burrows, A. and G. Orton (2009). „Giant Planet Atmospheres and Spectra." In: *ArXiv e-prints*. arXiv: 0910.0248 [astro-ph.EP].

Burrows, A. et al. (2007). „Theoretical Spectral Models of the Planet HD 209458b with a Thermal Inversion and Water Emission Bands." In: *ApJ* 668, pp. L171–L174. DOI: 10.1086/522834. arXiv: 0709.3980.

Castelli, F. and R. L. Kurucz (2003). „New Grids of ATLAS9 Model Atmospheres." In: *Modelling of Stellar Atmospheres*. Ed. by N. Piskunov, W. W. Weiss, and D. F. Gray. Vol. 210. IAU Symposium, 20P.

Crossfield, I. J. M. et al. (2012). „Spitzer/MIPS 24 μm Observations of HD 209458b: Three Eclipses, Two and a Half Transits, and a Phase Curve Corrupted by Instrumental Sensitivity Variations." In: *ApJ* 752, 81, p. 81. DOI: 10.1088/0004-637X/752/2/81. arXiv: 1202.1562 [astro-ph.EP].

de Kok, R. J. et al. (2013). „Detection of carbon monoxide in the high-resolution day-side spectrum of the exoplanet HD 189733b." In: *A&A* 554, A82, A82. DOI: 10.1051/0004-6361/201321381. arXiv: 1304.4014 [astro-ph.EP].

Désert, J.-M. et al. (2008). „TiO and VO broad band absorption features in the optical spectrum of the atmosphere of the hot-Jupiter HD 209458b." In: *A&A* 492, pp. 585–592. DOI: 10.1051/0004-6361:200810355. arXiv: 0809.1865.

Diamond-Lowe, H. et al. (2014). „New Analysis Indicates No Thermal Inversion in the Atmosphere of HD 209458b." In: *ArXiv e-prints*. arXiv: 1409.5336 [astro-ph.EP].

Fortney, J. J. et al. (2010). „Transmission Spectra of Three-Dimensional Hot Jupiter Model Atmospheres." In: *ApJ* 709, pp. 1396–1406. DOI: 10.1088/0004-637X/709/2/1396. arXiv: 0912.2350 [astro-ph.EP].

Freedman, R. S., M. S. Marley, and K. Lodders (2008). „Line and Mean Opacities for Ultracool Dwarfs and Extrasolar Planets." In: *ApJ* 174, pp. 504–513. DOI: 10.1086/521793. arXiv: 0706.2374.

Gibson, N. P. et al. (2013). „The optical transmission spectrum of the hot Jupiter HAT-P-32b: clouds explain the absence of broad spectral features?" In: *MNRAS* 436, pp. 2974–2988. DOI: 10.1093/mnras/stt1783. arXiv: 1309.6998 [astro-ph.EP].

Hubeny, I., A. Burrows, and D. Sudarsky (2003). „A Possible Bifurcation in Atmospheres of Strongly Irradiated Stars and Planets." In: *ApJ* 594, pp. 1011–1018. DOI: 10.1086/377080. eprint: arXiv:astro-ph/0305349.

Huitson, C. M. et al. (2013). „An HST optical-to-near-IR transmission spectrum of the hot Jupiter WASP-19b: detection of atmospheric water and likely absence of TiO." In: *MNRAS* 434, pp. 3252–3274. DOI: 10.1093/mnras/stt1243. arXiv: 1307.2083 [astro-ph.EP].

Husser, T.-O. et al. (2013). „A new extensive library of PHOENIX stellar atmospheres and synthetic spectra." In: *A&A* 553, A6, A6. DOI: 10.1051/0004-6361/201219058. arXiv: 1303.5632 [astro-ph.SR].

Knutson, H. A. et al. (2007). „Using Stellar Limb-Darkening to Refine the Properties of HD 209458b." In: *ApJ* 655, pp. 564–575. DOI: 10.1086/510111. eprint: arXiv:astro-ph/0603542.

Knutson, H. A. et al. (2008). „The 3.6-8.0 μm Broadband Emission Spectrum of HD 209458b: Evidence for an Atmospheric Temperature Inversion." In: *ApJ* 673, pp. 526–531. DOI: 10.1086/523894. arXiv: 0709.3984.

Lockwood, A. C. et al. (2014). „Near-IR Direct Detection of Water Vapor in Tau Boötis b." In: *ApJ* 783, L29, p. L29. DOI: 10.1088/2041-8205/783/2/L29. arXiv: 1402.0846 [astro-ph.EP].

Mazeh, T. et al. (2000). „The Spectroscopic Orbit of the Planetary Companion Transiting HD 209458." In: *ApJ* 532, pp. L55–L58. DOI: 10.1086/312558. eprint: arXiv:astro-ph/0001284.

Narita, N. et al. (2005). „Subaru HDS Transmission Spectroscopy of the Transiting Extrasolar Planet HD 209458b." In: *PASJ* 57, pp. 471–480. eprint: arXiv:astro-ph/0504540.

Nidever, D. L. et al. (2002). „Radial Velocities for 889 Late-Type Stars." In: *ApJ* 141, pp. 503–522. DOI: 10.1086/340570. eprint: astro-ph/0112477.

Parmentier, V., A. P. Showman, and Y. Lian (2013). „3D mixing in hot Jupiters atmospheres. I. Application to the day/night cold trap in HD 209458b."

In: *A&A* 558, A91, A91. DOI: 10.1051/0004-6361/201321132. arXiv: 1301.4522 [astro-ph.EP].

Plez, B. (1998). „A new TiO line list." In: *A&A* 337, pp. 495–500.

Portmann, R. W. and S. Solomon (2007). „Indirect radiative forcing of the ozone layer during the 21st century." In: *Geophys. Res. Lett.* 34, p. 2813. DOI: 10.1029/2006GL028252.

Rodler, F., M. Kürster, and J. R. Barnes (2013). „Detection of CO absorption in the atmosphere of the hot Jupiter HD 189733b." In: *MNRAS* 432, pp. 1980–1988. DOI: 10.1093/mnras/stt462.

Rodler, F., M. Lopez-Morales, and I. Ribas (2012). „Weighing the Non-transiting Hot Jupiter τ Boo b." In: *ApJ* 753, L25, p. L25. DOI: 10.1088/2041-8205/753/1/L25. arXiv: 1206.6197 [astro-ph.EP].

Rowe, J. F. et al. (2006). „An Upper Limit on the Albedo of HD 209458b: Direct Imaging Photometry with the MOST Satellite." In: *ApJ* 646, pp. 1241–1251. DOI: 10.1086/504252. eprint: astro-ph/0603410.

Schwenke, D. W. (1998). „Opacity of TiO from a coupled electronic state calculation parametrized by AB initio and experimental data." In: *Faraday Discussions* 109, p. 321. DOI: 10.1039/a800070k.

Sing, D. K. et al. (2013). „HST hot-Jupiter transmission spectral survey: evidence for aerosols and lack of TiO in the atmosphere of WASP-12b." In: *MNRAS* 436, pp. 2956–2973. DOI: 10.1093/mnras/stt1782. arXiv: 1309.5261 [astro-ph.EP].

Snellen, I. A. G. et al. (2008). „Ground-based detection of sodium in the transmission spectrum of exoplanet HD 209458b." In: *A&A* 487, pp. 357–362. DOI: 10.1051/0004-6361:200809762. arXiv: 0805.0789.

Snellen, I. A. G. et al. (2010). „The orbital motion, absolute mass and high-altitude winds of exoplanet HD209458b." In: *Nature* 465, pp. 1049–1051. DOI: 10.1038/nature09111. arXiv: 1006.4364 [astro-ph.EP].

Spiegel, D. S., K. Silverio, and A. Burrows (2009). „Problems with the TiO Hypothesis for Thermal Inversions in Hot Jupiter Atmospheres." In: *AAS/Division for Planetary Sciences Meeting Abstracts 41*. Vol. 41. AAS/Division for Planetary Sciences Meeting Abstracts, p. 68.03.

Stevenson, K. B. et al. (2014). „Transmission Spectroscopy of the Hot Jupiter WASP-12b from 0.7 to 5 μm." In: *AJ* 147, 161, p. 161. DOI: 10.1088/0004-6256/147/6/161. arXiv: 1305.1670 [astro-ph.EP].

Torres, G., J. N. Winn, and M. J. Holman (2008). „Improved Parameters for Extrasolar Transiting Planets." In: *ApJ* 677, pp. 1324–1342. DOI: 10.1086/529429. arXiv: 0801.1841.

Wright, J. T. et al. (2011). „The Exoplanet Orbit Database." In: *PASP* 123, pp. 412–422. DOI: 10.1086/659427. arXiv: 1012.5676 [astro-ph.SR].

Zellem, R. T. et al. (2014). „The 4.5 μm Full-orbit Phase Curve of the Hot Jupiter HD 209458b." In: *ApJ* 790, 53, p. 53. DOI: 10.1088/0004-637X/790/1/53. arXiv: 1405.5923 [astro-ph.EP].

3

DESIGN TRADE-OFF AND PROOF OF CONCEPT FOR LOUPE, THE LUNAR OBSERVATORY FOR UNRESOLVED POLARIMETRY OF EARTH

We provide a proof of the technical feasibility of LOUPE: the first integral-field snapshot spectropolarimeter, designed to monitor the reflected flux- and polarization spectrum of Earth. These are to be used as benchmark data for the retrieval of biomarkers, atmospheric and surface characteristics from future direct observations of exoplanets. We perform a design trade-off for an implementation in which LOUPE performs snapshot integral field spectropolarimetry at visible wavelengths. We used off-the-shelf optics to construct a polarization modulator, in which polarization information is encoded into the spectrum as a wavelength-dependent modulation, while spatial resolution is maintained using a micro-lens array. The performance of this design concept is validated in a laboratory setup. Our proof-of-concept is capable of measuring a grid of 50 $\times$ 50 polarization spectra between 610 and 780 nm of a mock target planet - proving the merit of this design. The measurements are affected by systematic noise on the percent level; and we discuss how to mitigate this in future iterations. We conclude that LOUPE can be small and robust while meeting the science goals of this particular space-application, and note the many potential applications that may benefit from our concept for doing snapshot integral-field spectro-polarimetry.

Hoeijmakers, Arts, Snik et al.
Optics Express, **24**, 21435 - 21453 (2016)

3.1 INTRODUCTION

3.1.1 *Multi-dimensional remote-sensing*

When obtaining spectra of extended objects we need to record light intensity as a function of image position and wavelength. This is challenging because it requires that three dimensions of information are captured on a detector that is generally 2D. This has led to the development of e.g. scanning slit spectrographs (in which one spatial direction is scanned in time), and integral-field units (in which the field of view is cropped into smaller sections, each of which is spectrally dispersed and imaged onto the detector using image slicers or fibers). For a review about the development of spectroscopy, see Hagen et al. (2013). When measuring polarization or polarization-spectra, this

problem is aggravated by the need to capture two additional quantities that describe the polarization state, which amounts to a 5-dimensional measurement. Therefore, imaging polarimeters or spectro-polarimeters generally require moving parts to scan through polarization directions or wavelength in time, or multiple beams, each with their own optics and detectors.

Implementations using moving-parts or multiple beams lead to non-common path errors and are not always desirable when complexity needs to be low. In recent years, several novel design concepts have been proposed to overcome these limitations, to allow for instantaneous imaging spectroscopy (e.g Dereniak, 2005), imaging-polarimetry (e.g. Kudenov et al., 2009; Kudenov et al., 2011) or imaging spectro-polarimetry (e.g. Kudenov et al., 2012)). These devices exploit the wavelength-dependent properties of polarization optics to encode polarization information in the spectral dimension (i.e. spectral modulation, as first proposed by Oka et al. (1999)), and collapse the remaining dimensions onto the detector plane using interferometric or tomographic methods.

Snik et al. (2009) presents a spectral modulator that performs snapshot spectro-polarimetry and is optimized for measuring linear polarization. The intensity spectrum is modulated by a sinusoidal modulation that encodes for the linear polarization fraction and angle. In the current work, we present a new design concept that combines this spectral modulation with a micro-lens array. This results in a spectro-polarimetric integral-field unit that obtains the linear polarization spectrum of a grid of independent field-points, in a single exposure without moving parts.

We present this design in the context of an ongoing challenge in astronomy: The search for habitable planets around other stars and the signatures of extra-terrestrial life. However, polarization measurements are important in a wide range of fields, including medical, defense, surveillance, climate and environment, and we expect that this type of device can find many applications outside astronomy as well.

The scientific background is expanded upon in the remainder of this section. Section 3.2.3 explains the science requirements and the working principles of our design. Section 3.3 introduces a laboratory proof-of-concept, followed by a discussion of its performance in section 3.4. Finally, section 3.5 describes the steps that we still need to take to optimize this instrument for a real-world application as part of a space-mission.

3.1.2 *Polarization of (exo)planets*

Polarimetry is widely used in astronomical observations, for example to study the planets in our solar system, interstellar dust-grains, circumstellar material and the magnetic fields of stars (see Tinbergen (1996) and Hough (2006) or

Snik et al. (2013) for comprehensive reviews). An enduring and important challenge in astronomy is the search for habitable planets that orbit other stars (extra-solar planets or 'exoplanets', in short). Much effort is directed at finding these exoplanets and studying their characteristics after having been discovered. The latter is especially problematic because planets are tiny compared to stars and they emit or reflect very little light compared to their host stars. The main challenge of exoplanet astronomy is thus to develop methods to increase the contrast between a star and its accompanying exoplanet. The fact that the contrast ratio (at visible wavelengths) between the brightness of the Sun and the Earth as seen by an interstellar observer amounts to 10^{-10}, shows that finding and studying an Earth-like exoplanet is a formidable challenge.

The light reflected by an exoplanet may be significantly polarized, depending on the scattering geometry (i.e. the illumination angle or 'phase' of the exoplanet) and the composition and structure of the planet's atmosphere and/or surface. This means that exoplanet observations may benefit from polarimetry. Firstly because the contrast between the bright star and the much fainter exoplanet is enhanced by filtering out the unpolarized starlight. Secondly, because the angle of linear polarization is determined by the on-sky position of the planet with respect to the star (position angle), a polarimeter filters all possible noise sources that emanate from directions other than the physical location of the planet. Thirdly, because the scattering, absorption and reflection properties of materials are wavelength-dependent, spectropolarimetric information provides additional diagnostics of an exoplanet's atmosphere and surface (Stam et al., 2004; Karalidi et al., 2012a). A good example of the use of polarization in planetary science is provided by Hansen et al. (1974), who used the polarization spectrum of Venus to determine that its upper cloud deck is composed of sulfuric acid. This could not have been derived from flux measurements of Venus. Also in the case of climate research, polarization information is essential to determine the properties of the different types of aerosols in the Earth's atmosphere (see e.g. Mishchenko et al., 2007).

As bigger telescopes and more advanced instruments are being constructed, the field of exoplanet research is focusing on establishing whether particular exoplanets satisfy minimal conditions for being habitable, and on the search for so-called 'biomarkers': observables that are uniquely indicative of extraterrestrial life. An example of a biomarker is the spectral absorption band of molecular oxygen (O_2) between 759 and 770 nm. Molecular oxygen is regarded a biomarker because the presence of oxygen in the Earth's atmosphere is the result of organic photosynthesis. Photosynthesis causes the atmosphere to be in chemical *disequilibrium* and without a constant supply of oxygen from biological sources, the Earth's atmospheric oxygen would be lost to chemical and surface reactions on time-scales of 10^6 years (Duursma

et al., 1994). Oxygen absorption in the spectrum of an exoplanet therefore indirectly reveals the presence of extra-terrestrial organisms (though in certain cases, abiotic sources of oxygen may exist (Narita et al., 2015)). Vegetation also directly contributes to the reflection spectrum of an exoplanet. Chlorophyll -a family of biomolecules responsible for the absorption of sunlight in the process of photosynthesis- reflects sunlight at green wavelengths between 500 and 600 nm and in the near-infrared beyond 700 nm. These spectral features are called the 'green bump' and the 'red edge', are observable in the Earth's spectrum due to the planet-wide presence of photosynthetic organisms (Seager et al., 2005; Briot et al., 2014). It was shown by Sparks et al. (2009) that chlorophyll in photosynthetic microbes and plant-leaves induces circular polarization upon reflection. This is attributed to the fact that chlorophyll (like many other biological compounds) exhibit *homochirality*: The preferential occurrence of one particular configuration of an asymmetric molecule. It is believed that homochirality is a necessary attribute of the information-replicating processes which make life possible and it may even be a defining aspect of life itself (Carroll, 2009). Although multiple scattering of light by aerosol and cloud particles, and single scattering by some types of aerosol particles, are known to produce circular polarization as well, the spectral properties of homochiral biomatter are so distinctive that circular polarization can be concluded to be a powerful biomarker.

3.1.3 *Earth as a model exoplanet*

Future (polarization) observations of Earth-size exoplanets will necessarily be disk-integrated, because the spatial resolution of even the largest telescopes currently conceived is insufficient to resolve them. To assess the habitability of such planets, these observations will be compared to disk-integrated models of the Earth, which represent observations of Earth as if it was observed from far away. At the same time, we need to understand how different surface components contribute to the Earth's total polarization spectrum, so that a variety of distributions of Earth-like surface types can be matched to observations. To reliably retrieve habitability-indicators from future spectropolarimetric data, versatile and well-tested benchmarks of the Earth must thus be available.

Stam (2008) calculated the Earth's disk-integrated polarization spectrum for different diurnal phases (i.e. with major landmasses, the pacific ocean or clouds dominating the spectrum); as well as the disk-integrated polarization strength as a function of illumination angle (phase). They confirm that the polarization spectrum provides an extra dimension along which to discern clouds from liquid oceans from landmasses - the latter two being especially difficult to discern by the shape of the disk-integrated spectrum alone. An-

other important prediction is the visibility of the polarization of the rainbow at $\sim 30^\circ$, caused by high-altitude water droplets. As such, the polarization phase-curve can reveal the presence of water vapour, a very important ingredient of an Earth-like biosphere (Karalidi et al., 2012a).

Attempts at measuring the Earth's polarization spectrum have been made before. One technique is to use Earth-shine: Sunlight that is reflected by the dayside of the Earth, onto the dark side of the Moon, into a telescope on the night-side of the Earth. Excitingly, Earthshine measurements have revealed that the Earth's vegetation leaves strong biomarkers in the global reflection spectrum of Earth (Pallé, 2010) and it might also leave a trace in the global polarization spectrum (Sterzik et al., 2012). However, Earthshine suffers from a number of drawbacks:

- Any telescope can only see the Earth-shine coming from the hemisphere it is located on. That means that in order to measure the Earth's globally averaged polarization spectrum, Earth-shine observations need to be performed with telescopes spread out over the world. Measurements taken with various instruments under various circumstances would need to be combined, introducing systematic errors.

- Earthshine is observed on the un-illuminated side of the Moon. Therefore, the range of Earth's phase angles accessible to Earthshine observations is limited, because near full-Moon and new-Moon, Earthshine can never be observed.

- When Earth-shine is reflected off the lunar surface, it partly de-polarizes. This depolarization has a spectral dependence, varies across the lunar surface and is generally not well understood. The de-polarizing behaviour of the lunar surface can not be measured by mapping the polarization of sunlight reflected from the Moon. This is because polarization and de-polarization constitute different elements of the Mueller matrix. In the case of polarization, part of Stokes-I is transferred to Stokes-Q and U. However, in the case of de-polarization, part of Stokes-Q and U leak back into Stokes-I. See Bazzon et al. (2013) for an attempt at taking lunar de-polarization into account.

Besides Earthshine, the POLDER and PARASOL instruments produced polarization maps of the Earth's surface in the context of climate science (Parol et al., 2004; Tanré et al., 2011). These instruments however, are in low-Earth orbit and see only a small part of the Earth at any given instance of time. They therefore can't provide a measurement that integrates the light reflected off the entire planet in a single observation (Pallé et al., 2009). Also, these observations were exclusively broad-band, so only limited spectral information has been obtained from orbit.

A common orbit further away from Earth is geostationary orbit, 35,786 km above the surface. From this distance, the Earth has an angular diameter of 21° and can be imaged in one frame. However, the instrument would always see the same hemisphere of Earth, per definition of geostationary orbit. There are currently no spectro-polarimeters in geostationary orbit, and to observe the Earth as if it would be an exoplanet, the instrument should be located still further away.

3.1.4 *LOUPE: Spectropolarimetry from the lunar surface*

Karalidi et al. (2012b) propose to observe the Earth with a space-based spectropolarimeter, using the lunar surface as a sufficiently distant platform to produce disk-integrated polarization spectra. The surface of the Moon provides a stable vantage point from which the Lunar Observatory for Unresolved Polarimetry of Earth (LOUPE) can observe the Earth at all times. The Moon is tidally locked to the Earth, which means that the same side of the Moon always faces the Earth, and from any point on the Earth-facing side of the Moon, the Earth is always at approximately the same position in the sky. The diurnal rotation of the Earth allows the entire Earth's surface to be observed every 24 hours, and all phase-angles are scanned during each lunar orbit.

From the lunar surface, the instrument will thus produce a full set of benchmark data after one month of observations, covering all configurations at which the Earth could be observed if it had been an exoplanet in an edge-on orbit (note that an exoplanet in an inclined orbit will show a limited range of phase angles). A lifetime in the order of a few years would additionally make these observations sensitive to the effect of seasonal variations.

Karalidi et al. (2012b) formulate conceptual requirements that these observations should minimally fulfil to produce the necessary scientific output, and propose four possible implementations of LOUPE to accomplish this, either by measuring only linear polarization or the full Stokes vector; and with or without spatial resolution (i.e. imaging capability). In this paper, we present the development of a laboratory prototype of LOUPE that performs linear spectro-polarimetry with imaging capability. Although spatially resolved observations of exoplanets will not be possible in the foreseeable future, this implementation of LOUPE will allow the disk-integrated polarization spectrum to be obtained while simultaneously measuring local reflection properties. This information can be used to understand the individual contributions of the Earth's major surface features to the globally averaged polarization spectrum, and make the benchmark observations more flexible when applied to Earth-like exoplanets with different surface distributions. We constructed a proof-of-concept using off-the-shelf optics and demonstrate that

the instrument can be small, robust, and fully solid-state; and we conclude that this instrument can be a valuable addition to any lunar mission without having a large impact to the resources and complexity of the payload.

3.2 DESIGN OF LOUPE

3.2.1 *Science-derived instrumental requirements*

An outline of the scientific requirements of LOUPE were listed by Karalidi et al. (2012b). These are adapted and expanded below to illustrate the driving factors behind the design of our proof-of-concept for LOUPE.

1. Observations capture the entire disk of the Earth at any time.
2. Observations cover all diurnal phases and all phase angles of Earth. From the lunar surface, this translates to an instrument lifetime in excess of 1 month, with an observing frequency of more than once per hour to resolve the Earth's rotation.
3. Observations minimally cover known biomarker signatures in the optical part of the spectrum: The green bump between $500-600$ nm, the vegetation red edge between $700-760$ nm and the O_2A band between $750-770$ nm.
4. The spectral resolution for polarimetry is 20 nm.
5. Considering that we wish to observe features at the level of the variations predicted by the polarization models of Earth as shown by Stam (2008), the fraction of linear polarization P_L is measured at every wavelength with a sensitivity in the order of 0.1% and an absolute accuracy of 1%.
6. The instrument leaves a small footprint on the resource budget of the lander vehicle, such as size, mass, power consumption, data transfer bandwidth. The quantification of such parameters is beyond the scope of this paper.

Although the Earth is always visible from any point on the Earth-facing side of the Moon, the non-zero eccentricity of the lunar orbit does cause the Earth *librate* over the course of the orbit, with a projected extent of $\pm 8°$. Assuming a low level of mechanical complexity of the LOUPE instrument, we discard active pointing of the instrument to track the motion of the Earth on sky. This means that a field of view of at least $\sim 20°$ by $\sim 20°$ is needed to have the Earth (which itself has a diameter of 2°) in view at all times. This field could be integrated as a whole, but only if the Earth is not close to the

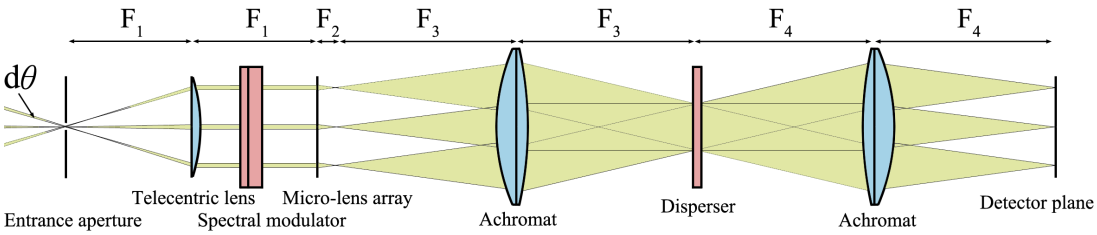

Figure 3.1: Schematic layout of LOUPE. Light enters through the aperture on the left. The three different beams are three examples of the $N \times N$ beams generated by the MLA, each of which will see a slightly different direction on the sky. Spectral dispersion is not shown.

horizon, and when the Sun is not in the field-of-view (at phase-angles clouse to 180°). Given that the parameters of the lunar mission of which LOUPE will take part are not yet known (the lunar horizon would likely be in view on a mission to the lunar polar regions), and that we wish to observe the Earth's polarization spectrum also at large phase angles when the angular distance between the Earth and the Sun is small, leads us to develop a solution with imaging capability. This has the major benefit that spatial resolution enables the independent characterization of the Earth's major surface features. By sampling the field of view with a grid of $\sim 50 \times 50$ spatial elements, the angular resolution of LOUPE is $\sim 0.4°$, equivalent to the angular scale of Earth's continents as seen from the Moon. For each such spatial point we then obtain a polarization spectrum, and any spatial point that sees the lunar horizon, the Sun or black space, will in principle not affect the measurement of Earth's disk.

3.2.2 *IFU design*

Our design is shown schematically in Fig. 3.1. The field-of-view is determined by an entrance aperture in the focus of a telecentric lens. This aperture is small compared to the focal length F_1 of the lens, so all rays passing through the aperture exit the lens in parallel. The parallel beam then passes through the polarization modulation optics described in section 3.2.3 below.

To achieve imaging capability, we place a micro-lens array (MLA) at the back focus of the telecentric lens. An MLA is a two-dimensional grid of $N \times N$ lenslets, each of which sees a different part of the field of view and creates its own image of the entrance aperture a focal distance F_2 away from the array. The image plane of the MLA thus consists of a grid of $N \times N$ micro-images of the entrance aperture, referred to as *micro-apertures*. This grid of micro-apertures is subsequently imaged onto a detector using a pair of achromats with focal lengths F_3 and F_4 so the detector sees a grid of $N \times N$ images of

the entrance pupil. The FOV is determined by F_1, the magnification of the field is determined by the ratio of F_3 and F_4, and the magnification of each micro-pupil is determined by the ratio of F_2 and F_3. We place a dispersion element in the middle of the 4f re-imaging system to spectrally disperse each of the $N \times N$ micro-pupils into a *micro-spectrum*.

3.2.3 *Spectral polarization modulation*

We use polarization modulation to simultaneously encode the intensity and polarization measurement along the wavelength axis of the spectrum. This can be accomplished by exploiting the strong wavelength-dependence of some polarization optics, which cause a sinusoidal intensity modulation to be imprinted on top of the intensity spectrum. The idea of encoding the full Stokes vector into the spectral dimension of a spectrograph was first described by Oka et al. (1999) and Jones et al. (2004). Snik et al. (2009) proposed to use a polarization modulator (sometimes referred to as a *channelled spectro-polarimeter* in the literature) that only measures the linear polarization spectrum, to detect and characterize the atmospheres of solar system planets. Since then, this scheme has also been used in iSPEX, a citizen science project aimed at measuring aerosols in the Earth's atmosphere using smartphones (Snik et al., 2014), and we use the same concept as the basis for our proposed implementation of LOUPE.

Polarization modulation works by stacking a $\frac{\lambda}{4}$-plate (QWP), a multiple-order retarder with retardance $\delta(\lambda)$ and a linear polarizer such that either axis of the QWP is aligned with the linear polarizer, while the axis of the multiple-order retarder is at a 45° angle with the other two. A linearly polarized input spectrum $S_0(\lambda)$ will receive a modulation that is sinusoidal in frequency (see Eq. 3.1). The amplitude of the modulation scales with the polarization fraction P_L, while the phase scales with the polarization angle, ϕ_L. Both can be obtained by fitting a curve to the modulated spectrum (Snik et al., 2009).

$$S_{\pm}(\lambda) = \frac{1}{2} S_0(\lambda) \times \left[1 \pm P_L(\lambda) \cos\left(\frac{2\pi\delta(\lambda)}{\lambda} + 2\phi_L(\lambda) \right) \right] \tag{3.1}$$

Depending whether the linear polarizer is aligned with either the fast or the slow axis of the QWP, the modulation shifts by 180°. If both these channels are obtained, they can be added to yield the original intensity spectrum without the modulation. The modulation itself is recovered by subtracting the two channels and normalizing it with the intensity-spectrum:

$$S_+ + S_- = S_0(\lambda) \tag{3.2}$$

$$\frac{S_+ - S_-}{S_+ + S_-} = P_L(\lambda)\cos\left(\frac{2\pi\delta(\lambda)}{\lambda} + 2\pi\phi_L(\lambda)\right) \tag{3.3}$$

Light enters the polarization modulation optics through the entrance aperture and the telecentric lens, which together generate the desired field-of-view. As mentioned before, all rays passing through the aperture exit the lens and pass through the polarization modulation optics in parallel. This is important because the retardance of waveplates depends on incident angle. Also, polarization-active optics should be as close to the front of the instrument as possible to reduce instrumental polarization induced by preceding optics. When exiting the polarization modulation optics, the beam continues to the MLA, where it is split up into micro-images of the aperture, each of which is then individually re-imaged and dispersed.

3.2.4 *Optical configuration*

The MLA can be rotated around its optical axis such that the dispersion direction is at an angle α with respect to the micro-pupil grid (see Fig. 3.2). A proper choice of α stacks the micro-spectra onto the detector in such a way that cross-talk between adjacent spectra is minimized, while maximizing the number of detector pixels that can be used effectively. The optimal choice for α depends on the length, width and number of micro-spectra. This means that there is a trade-off between spectral range, spectral resolution, spatial resolution, field of view and light-gathering power. The available detector pixels have to be divided over the $N \times N$ micro-spectra, so a higher spatial resolution (larger value of N) or a larger field-of-view necessarily decrease the spectral performance. Conversely, a larger spectral range and higher spectral resolution require the spectra to be dispersed over a larger number of detector pixels, limiting the value of N for a given detector size. Similarly, if the light-gathering power is increased by increasing the entrance aperture, the width of the resulting micro-spectra increases accordingly, requiring a larger value for α, and thus shorter micro-spectra (less spectral bandwidth or dispersion). This trade-off allows for great flexibility in the application of this design. Depending on the application, a direct exchange between spatial and spectral range and resolution and light gathering power can be made, using only robust steady-state components.

We conservatively assume that the grid of micro-spectra should fit on a 1k by 1k detector because larger detectors are rare in space-based applications. This upper limit on the amount of pixels limits the information density of the observations and the implementation of LOUPE should thus focus on de-magnifying and re-imaging the entrance aperture as finely as possible to allow for optimal stacking of the micro-spectra onto the detector. In

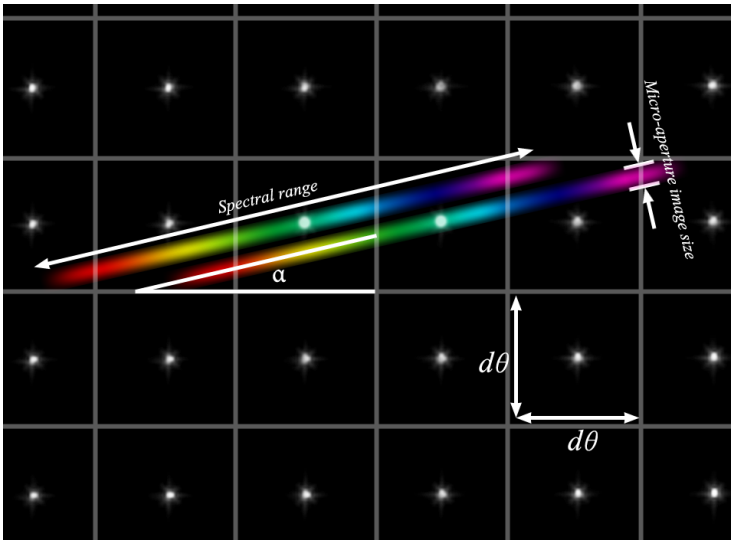

Figure 3.2: A read-out of the grid of micro-apertures, overlaid with a schematic illustration of how micro-spectra are stacked to fill the detector array. By rotating the grid of micro-lenses by an angle α with respect to the spectral dispersion direction, the micro-spectra can be stacked side-by-side. The smaller α can be made without lateral overlap, the more space there is in the dispersion direction for an increase in bandwidth or spectral resolution. The width of the spectra is determined by the magnification of the micro-apertures onto the detector, or the point-spread function of the re-imaging achromats, whichever dominates. The suppression of aberrations is therefore crucial to stack the micro-spectra efficiently.

the case of LOUPE, light gathering power is not a major issue because the Earth is a bright target, so LOUPE will use a small entrance aperture. Therefore, the imaging performance of the instrument determines the point-spread-function of the micro-apertures which then constrains the physical pixel size of the detector: If the pixel scale of the detector does not match the point-spread-function of the micro-aperture, the image of the micro-spectrum on the detector will be under or oversampled.

If the grid of micro-spectra measures 50×50 elements, a total of 2500 micro-spectra should be contained in a single image. In order to fully obtain the polarization modulation, each micro-spectrum should be imaged in two polarization channels simultaneously (see section 3.2.3). Therefore there are 200 pixels per individual micro-spectrum available on a 1k×1k detector. If we further assume a bandwidth of 250 nm, a PSF measuring 2 pixels and a margin of 1 pixel around all sides (to prevent lateral cross-talk between micro-spectra), the dimensions of a micro-spectrum are 50×4 pixels, which

results in a pixel scale of 5.0 nm/px and a spectral resolution of 10 nm/px. This is enough to sample a polarization modulation with a period of 20 nm as dictated to be a requirement in section 3.2.1. This pixel budget is thus theoretically sufficient to satisfy the sampling requirements. However, stacking the micro-spectra onto the detector is a serious challenge. This is why our proof-of-concept will be limited to the single-beam implementation of the polarization modulation scheme, and we note that the pixel budget can be relaxed greatly by choosing a larger detector (see Section 3.5).

3.3 PROOF OF CONCEPT

3.3.1 *Optics*

From left to right in Fig. 3.1 we have chosen the following optical components: The entrance aperture is a circular pinhole with a diameter of 1 mm. It is placed in the front-focus of a plano-convex $F_1 = 150.5$ mm lens with a diameter of 25.4 mm, made of fused silica to minimize stress birefringence. At the back focus of this lens, we place a square, 68×68 MLA measuring $15 \times 15 \times 1\text{mm}^3$, with a focal length of 0.93 mm. The polarization modulation optics is placed between the lens and the MLA, and consists of a zero-order QWP, a stack of six 4λ retarding polymer films (the same films are used in iSPEX (Snik et al., 2014)) and a 2" linear polarizer. The linear polarizer needs to be rotated to obtain the two complementary polarization channels sequentially. It is therefore placed in a rotation mount, so that it can be aligned to either axis of the QWP (see Section 3.2.3) This implementation therefore does not perform *snapshot* imaging polarimetry, as a sequence of two exposures is needed to capture both polarization channels. In Section 3.5 we discuss how this will be addressed in future iterations.

The focal plane of the MLA is re-imaged by a pair of identical 2" achromats with a focal length of 100 mm, spaced 200 mm apart. The dispersive element is a right-angle N-BK7 prism placed on a rotation platform in the middle between the re-imaging lenses. Because the spectral dispersion depends on the incident angle of the beam onto the prism, the dispersion can be fine-tuned by rotating this platform. The advantage of using a prism is that the dispersion increases towards blue wavelengths. This counters the decrease in the fast periodicity of the modulation at blue wavelengths, which scales with $\frac{1}{\lambda^2}$ (Snik et al., 2009).

At the image plane is a Point Grey Flea3 1.2 megapixel monochromatic CMOS camera. The detector consists of 1280×1024 square pixels, measuring $5.3\ \mu\text{m} \times 5.3\ \mu\text{m}$, and thus spans a total area of $6.8 \times 5.4\ \text{mm}^2$. The detector is aligned to the dispersion direction of the prism, so that the micro-spectra are imaged horizontally on the detector. Because the magnification of the two

achromats is unity, the image plane of the MLA matches the size of the MLA itself, which has an effective diameter of 14 mm. Therefore, this detector sees only a quarter of the re-imaged micro-pupils, and thus covers only a quarter of the total FOV. The micro-spectra are dispersed in the direction of the long side of the detector and the micro-pupil grid is rotated such that the spectra do not overlap, and that cross-talk between adjacent micro-spectra due to the wings of the PSF is minimal (see Fig. 3.2 and Section 3.2.2). In order to reduce aberrations induced by the re-imaging lenses, we add a circular field stop and an 800 nm short-pass filter behind the first achromat. Regardless, because the pixel scale of 5.3 μm^2 is small, the spectral performance of this implementation will be limited by the imaging performance of the optics as the spectral resolution is limited by the point-spread-function of the micro-apertures, rather than the spatial sampling of the detector array. This oversampling of the PSF is not relevant for our demonstration of the working principle of LOUPE.

The $F_1 = 150.5$ mm objective lens generates a circular FOV with a diameter of 9.6°. The beam exiting the lens has a diameter of 25.4 mm, which is subsequently vignetted by the mount of the MLA which has a circular clear area 14 mm wide. This thus cuts the total FOV to a diameter of 5.3°. Although this is much smaller than the required 20° FOV, we note that the FOV can be increased trivially by reducing the focal length of the lens to ~ 40 mm. However, we chose a slower lens because 4 cm between the lens and the MLA would have been insufficient to fit our polarization modulation optics. The image plane of the MLA is re-imaged onto the detector with unity magnification, so the grid of micro-spectra is circular with a diameter of 14 mm. The detector measures 6.8×5.4 mm^2, so it sees only a quarter of the re-imaged micro-pupils, and thus covers only a quarter of the already vignetted FOV. This can be mitigated by choosing a detector with larger pixels.

3.3.2 *Test observations*

We have simulated science spectra with our LOUPE prototype using a Styrofoam sphere as a model planet. The sphere (with a diameter of 7.8 cm) was illuminated by a slide projector at an angle of $10° < \gamma < 90°$ with the line of sight to the instrument, which was located at a distance of ~ 3 meters from the target. Observations consist of median-combined sequences of ten 1 m s^{-1} exposures to reduce photon-noise. In each polarization channel (Eq. 3.3), we also obtain such a sequence of wavelength calibration frames, polarization calibration frames and dark frames.

To assess how the prototype performs at retrieving the polarization of the Styrofoam target, we obtain control-measurements using a standard imaging-polarimetry setup: The target is imaged onto the camera by a single lens that

is preceded by a linear polarizer. We obtain the image at visible wavelengths (between 400 nm and 800 nm) in a horizontal (S_+) and a vertical (S_-) channel, parallel respectively perpendicular to the plane in which the light is reflected off the target. P_L is obtained by aligning and combining the two channels.

3.3.3 *Data reduction*

The detector images the grid of micro-spectra and saves them in 16-bit monochromatic TIFF images. We start the analysis by feeding a broadband deuterium-halogen lamp into the setup using a fiber, thereby uniformly illuminating the entrance aperture. This reveals each micro-spectrum at high contrast and allows us to establish the location and extent of all micro-spectra. The micro-spectra are surrounded by background flux, caused by aberrations, diffraction, internal reflections and other instrumental imperfections. In the uniformly illuminated image, we designate a collection of pixels between micro-spectra that are furthest away from the bulk of the flux of the surrounding micro-spectra. We fit a 3^{rd} degree polynomial surface to all these pixels in the image to get a measure of the background flux, which we subtract. Bad pixels are removed by interpolating pixel values that are more than 4σ away from their surroundings. Finally, the micro-spectra are cropped-out along rectangular areas, and extracted by adding the pixel rows of the cropped region. We co-add the rows with Gaussian weights to weigh down rows away from the central pixel row, that are more sensitive to cross-talk from PSF-wings of neighbouring micro-spectra (see Section 3.4 for an analysis of the cross-talk in this setup). After extraction, we have thus obtained a 1D representation of each micro-spectrum.

3.3.4 *Wavelength calibration*

To obtain a wavelength calibration, we illuminate the entrance aperture with a HgAr line-lamp that emits 15 lines in the range between 450 to 820 nm. We locate these lines in each micro-spectrum by obtaining the center-of-mass of each line and matching those to the known line-positions of the mercury-argon spectrum. Not all lines are resolved by LOUPE, so we match the center-of-mass of a group of unresolved lines to the center-of-mass of the known wavelength-positions, while weighing for the individual line strengths. We map pixel positions to wavelength by performing a 4^{th} degree polynomial fit, also weighted to the known line strengths. This yields a wavelength-solution for each extracted micro-spectrum.

3.3.5 *Polarization calibration*

The modulation as described by Eq. 3.3 scales with $P_L(\lambda)$ between 0 and 1. However in practise, our prototype is not able to produce a modulation with an amplitude of 1 when illuminated with fully polarized light. This is because the performance of the polarization optics is not perfect and wavelength dependent. Though the wavelength dependence of the multiple-order retarder was exploited to produce the polarization modulation, similar wavelength dependence of the QWP and the linear polarizer results in reduced efficiency at wavelengths away from the rated optimum wavelength of the optics. Similarly, the imaging performance of the lenses deteriorates near the edges of the wavelength range. This means that spectral resolution of the instrument decreases accordingly so that light from a maximum of the modulation may leak into the surrounding minima, decreasing the observed amplitude of the polarization modulation. This effect is especially relevant towards blue wavelengths, because the frequency of the polarization modulation increases with decreasing wavelength (Snik et al., 2009).

The wavelength-dependence of the efficiency of the instrument is calibrated by fully polarizing the deuterium-halogen input (see Section 3.3.3) using a linear polarizer. In our case, only a single reflection geometry is relevant (see Section 3.3.2). Ideally however, we would calibrate Stokes-Q and U independently because the retardance of the QWP is not exactly $\frac{1}{4}\lambda$, which reduces the ability of the polarization modulator to register polarization in the direction of U (Snik et al., 2009; van Harten, 2014).

The calibration spectrum also yields a measurement of the retardance $\delta(\lambda)$ of the multiple-order retarder and the zero-point angle of the input polarization ϕ_L. These are represented by the frequency and the phase of the modulation, and are obtained by fitting the modulation (Eq. 3.3) to each calibration spectrum.

3.3.6 *Demodulation*

Equation 3.3 assumes that the transmission in both polarization channels is identical, in which case the modulation function oscillates around 0. However in practise, the throughput of the instrument will be slightly dependent on the input polarization, which means that both channels need to be normalized independently. We adopt the procedure outlined by Harten et al. (2014), who iteratively correct the wavelength-dependent transmission for each channel $t_\pm(\lambda)$ by requiring that the integral over any period of the modulation is 0. The deviation from 0 is measured for $\sim$ 200 steps in phase (i.e. wavelength), which is then fit with a 4^{th} degree polynomial to obtain the wavelength-dependent transmission correction on $t_\pm(\lambda)$ (see Fig. 3.3).

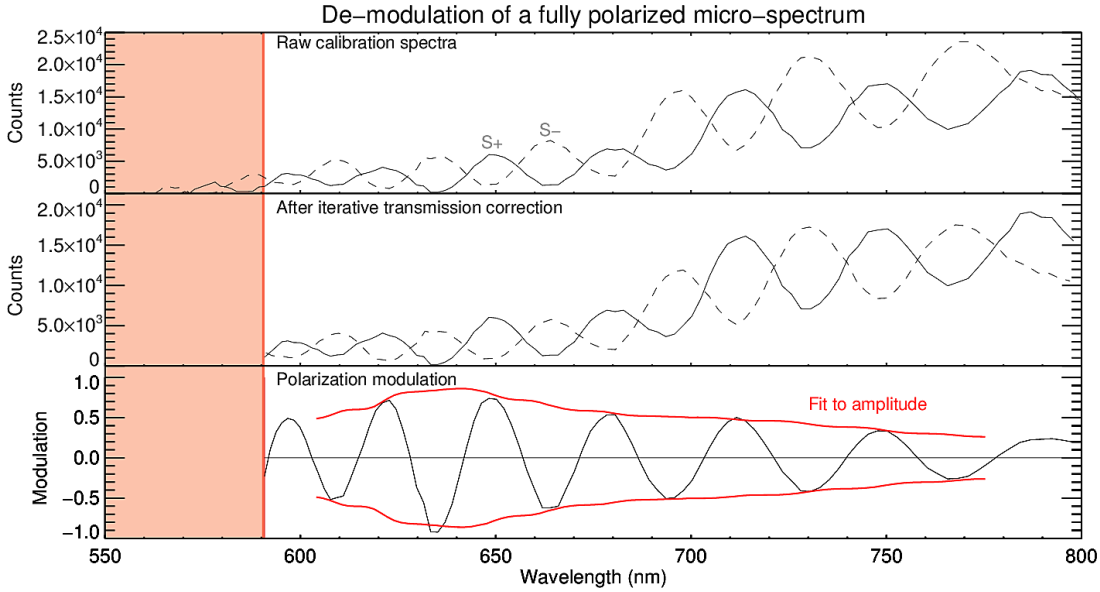

Figure 3.3: Step-wise reduction of a single micro-spectrum from the two calibration channels (i.e. fully polarized input either in the horizontal or vertical direction). The top panel shows both channels of a single micro-spectrum after dark subtraction, background correction and extraction. In the middle panel, the two have been modulated such that the transmission in both channels is equalized. The bottom panel shows the extracted polarization modulations as described by Eq. 3.3. In order to obtain a polarization measurement from these, we fit the modulation (Eq. 3.3) to a $\pm$15 nm range around each point. The measured amplitudes are then divided by the modulation amplitudes of the respective (fully polarized) calibration micro-spectra, the result of which yields P_L for each point. Note that the wavelength range is cut during the analysis. On the one hand, this is because of low signal-to-noise of the calibration spectra. On the other, chromatic aberrations deteriorate the spectral resolution towards shorter wavelengths, causing the polarization modulation to become unresolved. Also note that the efficiency of the spectral polarization modulation-optics at producing the polarization modulation (amplitude of the modulation), diminishes long-ward of 700 nm. This is due to the break-down of the linear polarizer at red wavelengths.

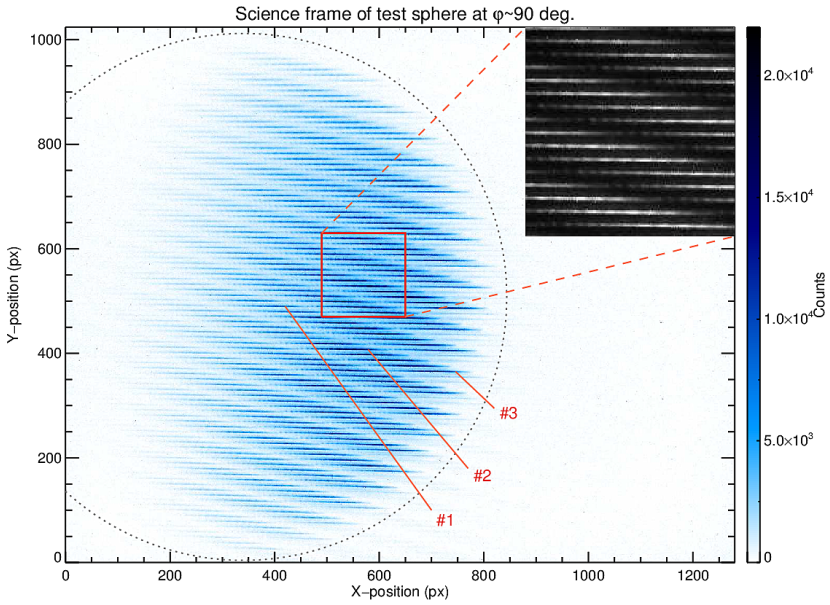

Figure 3.4: A readout of a single LOUPE exposure while observing the Styrofoam test-sphere, illuminated to simulate a planet at close to 90° phase. Microspectra #1 to 3 are separately shown in figure 3.5, for illustrative purposes. Significant linear polarization is caused in this scattering configuration as evidenced by the fact that the polarization modulation can be observed by eye in the zoomed-in section in the upper-right.

The corrected modulation is fit within bins of 20 px (on average ~ 30 nm) wide between wavelengths of 610 and 800 nm (as the efficiency of the modulation diminishes blueward of 610 nm), while keeping the retardance $\delta(\lambda)$ fixed to the value as measured by fitting the entire calibration spectrum. This provides a measurement of the average amplitude of the modulation per wavelength-bin, for both the "science" micro-spectra as well as their associated calibration micro-spectra (see Fig. 3.3). These are divided to yield the polarization spectrum of each field-point. The angle of polarization is obtained by subtracting the measured phases of the calibration spectra from those of the "science" spectra.

3.4 PERFORMANCE OF THE LOUPE PROTOTYPE

Figure 3.4 shows a readout of the prototype, with the polarization modulations of three micro-spectra illustrated in Fig. 3.5, along with the resulting measurements of $P_L(\lambda)$. Each point of P_L is obtained by fitting the modulation curve in a range of ± 15 pixels from that point, and therefore represents

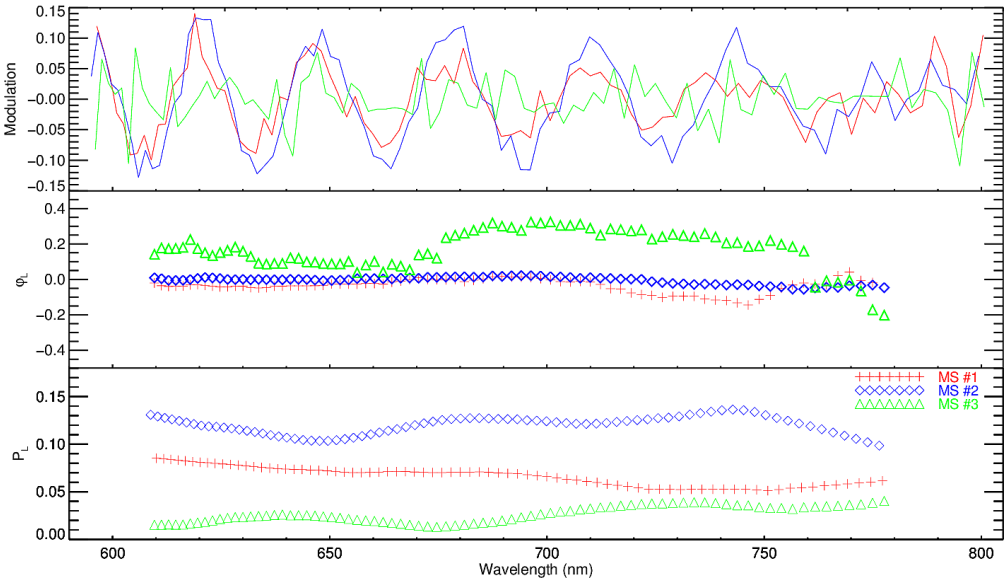

Figure 3.5: Top panel: The three micro-spectra selected in figure 3.4 after extraction, wavelength calibration and transmission correction. Middle panel: The angle of polarization ϕ_L relative to the phase of the calibration spectra. The increased scatter in retrieved polarization angle of micro-spectrum #3 is reminiscent of the fact that the modulation is dominated by noise because the amplitude is low. Bottom panel: P_L is obtained by combining the two polarization channels of each according to Eq. 3.3 (only one channel is shown in the top panel), fitting the amplitude as a function of wavelength, and dividing the measured amplitudes by the corresponding amplitudes measured in the fully-polarized calibration micro-spectrum. Note that the wavelength-range is reduced at the edges, because the fit at the edge of the spectrum generates a measurement of P_L at the center of the fitting range, and that the measurement of P_L is smoothed with a box-window that matches the size of the fitting range around each point.

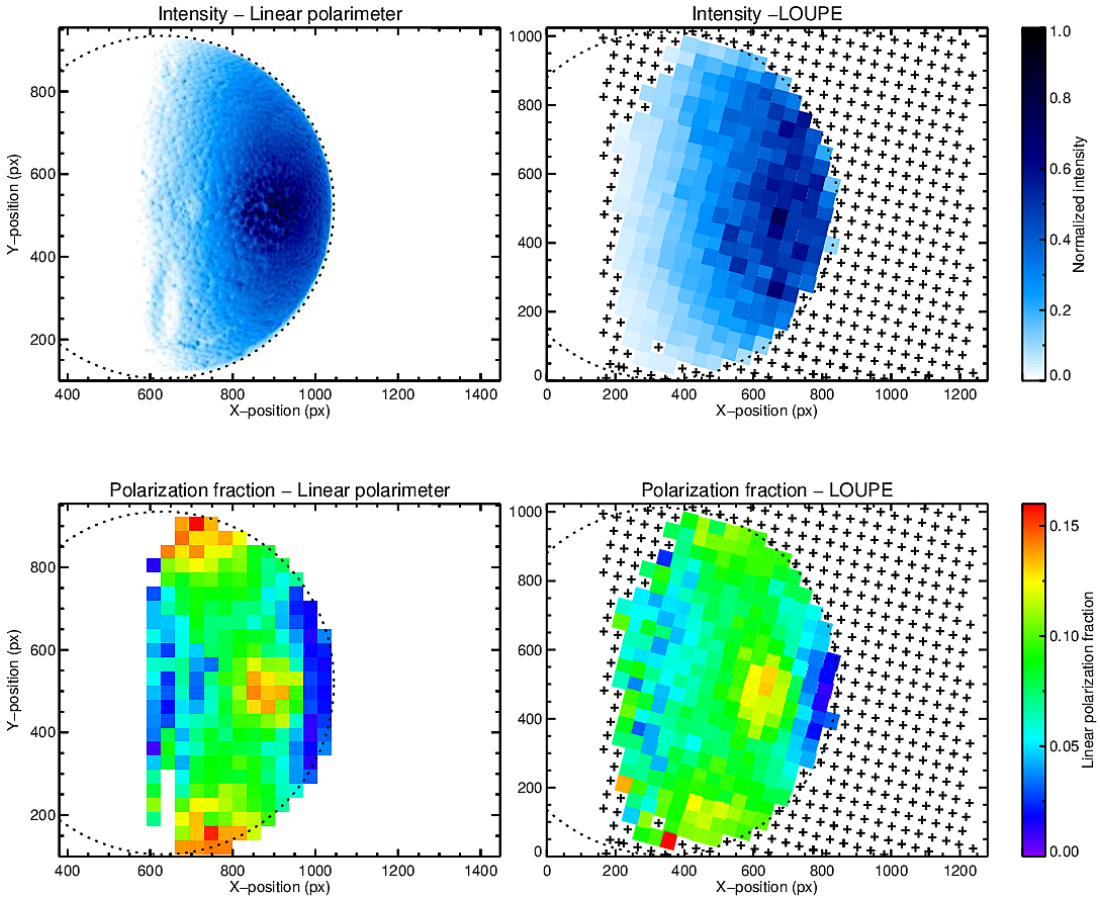

Figure 3.6: Comparison of a measurement obtained by LOUPE versus a higher resolution image obtained using a standard linear polarizer. The target is the Styrophome sphere, illuminated from a right angle. The top panels show the raw intensity image of the linear polarimeter (upper-left, arbitrary colour scale), and the average of the intensity in the micro-spectra between 600 and 700 nm, as determined for each micro-spectrum obtained by LOUPE (upper-right). The bottom panels show the resulting distribution of P_L on the sphere as measured by subtracting the two channels taken with linear polarimeter (bottom-left), and the average of P_L measured by LOUPE, also between 600 and 700 nm (bottom-right). The control measurement of P_L in the bottom-left panel was blurred and down-sampled to the same angular resolution and grid-size as the measurement by LOUPE in the bottom-right panel. The colour scale is the same for both lower panels, which shows that LOUPE is able to reproduce the global variations in P_L, at the same qualitative level. The crosses in the right panels denote the locations of micro-spectra. This grid is slanted because the MLA is rotated with respect to the detector array. Only micro-spectra with sufficient flux were extracted and analysed.

a $\sim 23-42$ nm bin (at 610 and 800 nm respectively) within which P_L is measured. These measurements are subsequently smoothed to the bin-size (Snik et al., 2009), producing bin-averaged measurements of P_L with a typical scatter of a few percent. This level of noise scatter is fully accounted for by photon noise in the micro-spectra (primarily noise in the science-frames because flux levels are low), readout noise and photon-noise in the background that was subtracted.

With a measurement of P_L for each micro-spectrum, we re-construct the spatial dependence of the polarization fraction across the image, and compare it with control measurements obtained with the linear polarimetry setup (see Section 3.3.2). Figure 3.6 shows this comparison for the intensity images (top panels) and polarization (bottom panels). LOUPE is able to retrieve the major features in the polarization map, notably the specular reflection and decreasing polarization towards the edge on the right side of the sphere. Quantitatively, systematic errors clearly persist on the percent level: LOUPE seems to overestimate the polarization by a few percent near the edges of the disk, while not reproducing the strong polarization towards the poles observed in the control measurement.

There are a number of possible causes for systematic errors. Most importantly, there is the possibility that micro-spectra are stacked too closely together, causing cross-talk between neighbouring micro-spectra. Cross-talk is especially important when the amplitude of the polarization modulation is high (as is the case for the polarization calibration spectra) because the maximum of the polarization modulation of one micro-spectrum can strongly contaminate the minimum of an adjacent spectrum. This means that cross-talk is expected to peak at certain wavelengths (van Harten, 2014). For each pixel (in the spectral direction between 600 to 800 nm, which covers all of our effective wavelength range, see Section 3.3.6) of each micro-spectrum, we modelled the integrated flux originating from all adjacent micro-spectra by fitting their lateral profiles with Gaussian distributions. We define cross-talk in any pixel, as the ratio of the flux originating from all neighbouring micro-spectra, to the total flux in the pixel. We find that for the micro-spectra onto which the Styrofoam sphere is imaged, the peak cross-talk exceeds 5% in three of the polarization calibration spectra, but never exceeds 5% in the science-frames. At the same time, the wavelength-averaged cross-talk is never higher than 0.5% for any of the polarization calibration spectra, and never exceeds 0.2% for any of the science-spectra.

However, close examination of the high-contrast images used to calibrate the locations of the micro-spectra (Section 3.3.3) reveal the presence of a significant ghost associated with each micro-spectrum, caused by an internal reflection in the re-imaging system. These ghosts partly overlap with the cores adjacent micro-spectra and may cause significant cross-talk - as they can be discerned by eye. We therefore conclude that although cross-talk from

the PSF-wings of adjacent micro-spectra cannot account for systematic errors of several percent on the measured polarization levels, it is possible that an internal reflection can.

Besides cross-talk, there are a number of other sources of error that could contribute to the observed systematic variations, and which must also be addressed in future iterations. Firstly, the linear polarizer used to calibrate LOUPE, as well as the polarizer used in the imaging polarimeter with which we perform the control measurements are wavelength-dependent and not calibrated. Similarly, the light-source used to illuminate the Styrofoam sphere is not stabilized and may be varyingly polarized.

Secondly, we have not characterized the instrumental polarization. The polarization-modulation optics are preceded only by a single objective lens which is made of fused-silica to minimize stress-birefringence. Although we expect this lens not to cause significant polarization, it was not calibrated for.

Thirdly, an incorrect extraction of large-scale background flux (the measurement of which is affected by the presence of ghosts) will offset all micro-spectra, decreasing the amplitude of the polarization modulation (Snik et al., 2009; van Harten, 2014). Fractionally, this would affect the polarization calibration spectra more strongly than the science spectra, causing an apparent excess of the derived polarization which is dependent on the location in the field.

Fourthly, detector non-linearity was not characterized, and would again mainly affect the polarization calibration because the flux levels in these spectra were generally high.

Finally, because S_+ and S_- are obtained separately by manually rotating the linear polarizer of the polarization modulation optics, the two channels are not imaged on the same detector position, which introduces errors due to flat-field and defocussing.

We note that systematic errors on the percent-level are not unexpected, given the usage of rotating polarizers and an un-stabilized light source to perform calibration measurements. Solving these systematic errors by using better calibration data and by addressing the issues mentioned above with a more sophisticated data reduction method and higher quality components, is beyond the scope of this proof-of-concept. More importantly, there are some qualitative departures from the requirements stated in Section 3.2.1 and the design concept described in Section 3.2.2. These represent no fundamental barriers however, and possible avenues and considerations for addressing these issues in future iterations are discussed in the following section.

3.5 OPTIMIZING THE PROTOTYPE MODEL

3.5.1 *Beamsplitter*

The notion of a snapshot linear polarimeter is defeated when the polarization channels S_+ and S_- need to be obtained in sequence with a rotating polarizer, as is the case with this proof-of-concept. It uses a single beam setup whereas LOUPE should measure two beams simultaneously to do full linear spectro-polarimetry using snapshot observations. Dual-beam capability is achieved by replacing the linear polarizer with a polarizing beamsplitter. This doubles the density of micro-spectra on the detector array as noted in Section 3.2.3. We performed a trade-off analysis between a Wollaston prism, a Savart plate and a polarization grating.

- The Wollaston prism would be placed in the pupil-plane near the dispersive element. The two polarization channels exit the prism in diverging beams, with separation angle γ. The plane of separation is perpendicular to the dispersion direction of the dispersion element, such that the micro-spectra belonging to each channel are stacked laterally.
- The Savart plate is similar to the Wollaston prism, but would be placed in the focal plane of the MLA. It splits the two polarization channels into beams that exit the plate in parallel, with spatial separation d. The plane in which the beams are separated is again perpendicular to the dispersion direction, causing the micro-spectra to be duplicated in the lateral direction.
- The polarization grating would combine the functionality of a beamspltiter and a dispersion element (Packham et al., 2010), and be placed in the foci of the two re-imaging achromats. The polarization grating disperses the beam into two spectral orders, each in orthogonal polarization directions. The two orders lie on opposite sides of an undispersed zero-th order which serves as a direct measurement of the total integrated flux (Stokes-I).

Of these, we consider the Savart plate to be the best option for LOUPE. The advantage of the Savart plate over the Wollaston prism is that the separation angle of the Wollaston prism varies over the field, because the beams coming from the MLA pass through the prism at different incidence angles. The Savart plate does not have this problem because it is located in a parallel beam. An additional disadvantage of using a Wollaston prism, is that it would be sensitive to systematic polarization originating in the MLA and the first achromat. In contrast, the Savart plate is located one step earlier in the optical path. Finally, the separation between the exiting beams of the Savart plate depends on the thickness of the plate. To efficiently stack the

micro-spectra the separation must be made small, which can be achieved by choosing a thin plate. By putting an achromatic half-wave plate (HWP) between the two parts of the Savart plate, any crystal abberations (primarily astigmatism) will be identical in both polarization directions which means that they can be corrected for using a cylindrical lens (Keller, 2006).

We favor the Savart plate over the polarization grating because in the latter implementation, optimally stacking the spectra onto a small detector is more complicated. With a polarization grating, the spectral dispersion and polarization splitting occur in the same direction. Ideally, spectra are stacked such that the gap between the zero-th and first order of one spectrum is filled by the first order of a nearby micro-spectrum (Rodenhuis et al., 2012). This reduces the stacking efficiency at the edges of the field, where gaps between the dispersion orders will not be filled. For higher dispersion strengths, the orders will be further apart, so the total stacking efficiency will decrease with spectral resolution. In the case of the Savart plate, the spectral dispersion is decoupled from the polarization separation, allowing for more efficient stacking on a small detector.

3.5.2 *Stacking*

Figure 3.2 shows how single-channel observations are stacked onto the detector using the Savart plate. The lateral distance between micro-spectra in the single-beam setup is ~ 50 μm (equivalent to 10 px, see figure 3.4) and if we assume the same margin in the dual-beam implementation, the length of each micro-spectrum should be halved in order to double the available space needed to image the second channel. Now the trade-off described in Section 3.2.2 is particularly relevant: Reducing the spectral dispersion reduces the bandwidth and/or the spectral resolution, provided that the detector pixels are shrunk accordingly. This has implications for the dimensions of the detector and the accessible field-of-view. Conversely, maintaining bandwidth and spectral resolution means that a smaller amount of micro-spectra can be fit onto the detector, resulting in a reduced spatial resolution or increased cross-talk, if spectra are to be stacked more closely to each-other.

We made a MATLAB simulation to optimize dual-channel stacking on a 1k by 1k detector considering the application of both a hexagonal and a square MLA. We assume square pixels with a size of 10×10 μm^2 and micro-spectra with a length of 64 pixels (slightly longer than theorized in Section 3.2.2), a width of 2 pixels and a lateral margin of 3 pixels (giving a total lateral distance of 5×10 μm $= 50$ μm between spectra). As argued before, better spectral characteristics can be achieved by reducing aberrations (which decreases the margin needed between adjacent micro-spectra) and by increasing the resolution and size of the detector array. From the MATLAB simulation it was

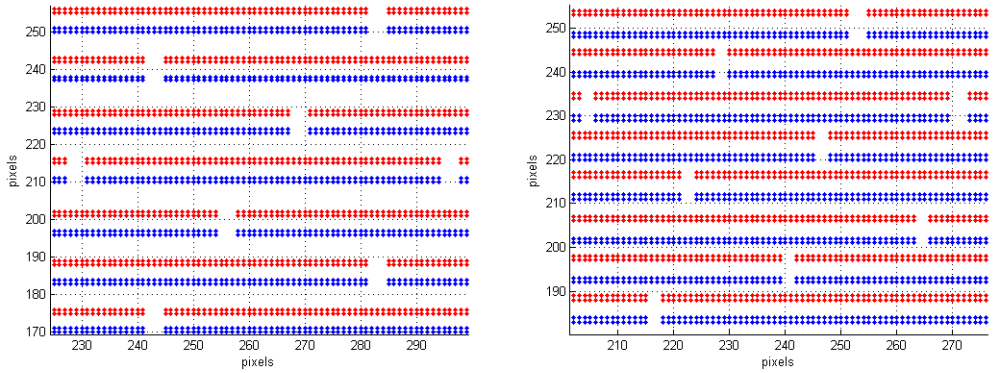

Figure 3.7: Stacking using a square MLA (left), compared to a hexagonal MLA (right). The red and blue spectra denote the two polarization channels. For mictro-spectra with these dimensions, a hexagonal MLA grid allows for more efficient stacking than a square MLA grid.

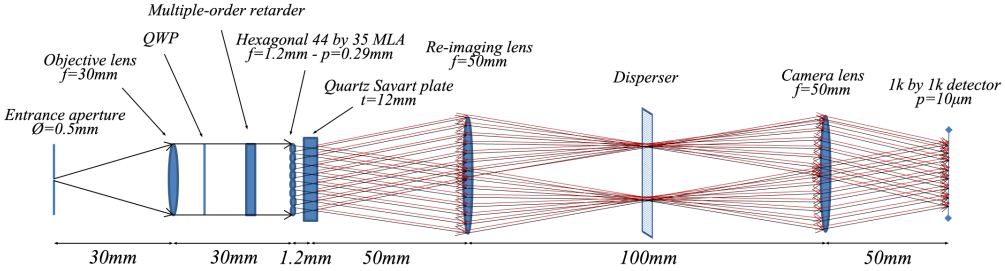

Figure 3.8: The dual beam concept for LOUPE. The red and black beams emerging from the Savart plate represent the two orthogonal polarization channels. Dispersion is not shown.

found that optimal stacking with a hexagonal MLA occurs at a rotation angle of $\alpha = 12.5°$, in which case a maximum of 44×35 spectra can be fully imaged on the detector. In contrast, a square MLA allows a maximum of 32×34 spectra at a rotation angle of $\alpha = 26.5°$ (see Fig. 3.7). A hexagonal MLA therefore provides better stacking efficiency than a square MLA, which serves to show that the choise of micro-lens configuration is important when designing an integral-field spectrograph using an MLA.

3.5.3 *Proposed design implementation and further considerations*

Our proposal for the dual beam concept for LOUPE is shown in Fig. 3.8. The system has a one-to-one re-imaging pair behind the MLA with focal lengths

of $f = 50$ mm. The hexagonal MLA contains 44×35 lenslets with a focal length of $f_{MLA} = 1.2$ mm and a lens diameter of 290 μm. To obtain a field of view with of 20°, the field lens should have a focal length of $f = 30$ mm, giving an $f/4$ system and a spatial resolution of 0.6° (3×3 samples over the Earth's disk). The image of the 0.5 mm entrance aperture will then have a diameter of 20 μm, corresponding to 2×2 pixels on a detector with 10 μm pixels. To achieve a lateral distance of 5 pixels between the spectra of the two channels, the Savart plate needs to be made of 12 mm thick quartz. As follows from Fig. 3.8, the dimensions of this design are approximately $26 \times 2 \times 2$ cm^3, which can be further compressed by folding the optical path, possibly using a Littrow configuration and if necessary, a three-mirror anastigmat.

In this design, micro-spectra have a length of 64 px and a PSF diameter of 2 px, which can provide 32 independent spectral measurements between $500 - 800$ nm, equivalent to a spectral resolution of 9 nm, enough to sample a polarization modulation with a period of 20 nm, in line with the science requirements stated in Section 3.2.1. We do stress that an increase of the detector size beyond $1k \times 1k$ as well as a reduction of the spot size would directly result in better spectral and spatial performance of this design.

Further issues that need to be addressed are the shielding of the instrument against extreme fluxes when the Sun is in view, the calibration of the instrument (either before the start of the mission or by adding the capability to calibrate the instrument after launch), the possibility of active-pointing (which would radically relax the field-of-view requirements and improve performance, but would involve moving parts which would increase the risk of failure), the (thermo-)mechanical and electrical design, power (power usage will be low owing to the solid-state design) and data handling (considering the possibility of on-board processing).

3.6 CONCLUSION

This paper presents a proof-of-concept for the Lunar Observatory for Unresolved spectro-Polarimetry of Earth (LOUPE). From the Earth-facing side of the Moon, LOUPE will measure the polarization spectrum of Earth over all phase-angles and diurnal phases, to generate a benchmark for future polarization observations of exoplanets, as initially proposed by Karalidi et al. (2012b). Such benchmarks are needed to verify the polarization models that will be used to infer physical characteristics of the exoplanet environment from their polarization spectra and phase-curves, and to optimize instrumentation for direct observations. The design we propose is the first snapshot spectro-polarimetric integral-field unit: A linear spectro-polarimeter with spatial resolution. This is accomplished using a robust solid state design without

moving parts and the polarization modulation principle in combination with a micro-lens array.

We constructed a prototype using off-the-shelf components, and prove that this design for LOUPE is able to retrieve spatially resolved spectro-polarimetric observations of a mock planet target. These observations are affected by systematics on the percent level, which we mainly attributed to a combination of ghost images and instrumental polarization caused by the optics and the light-source. The main shortcoming of our proof-of-concept is that it relies on a rotating linear polarizer to obtain both polarization channels S_+ and S_- in sequence. However, we have discussed the most important avenues for solving this shortcoming by incorporating dual-beam functionality using a Savart plate and modelled how the micro-spectra can optimally be stacked onto the detector using a hexagonal micro-lens array. Finally, we have identified the challenges that remain to be addressed to reach a fully capable flight-model.

Due to its low level of complexity and small size, this design is ideal for application in space, and we are in the process of designing a flight-model for LOUPE. In addition, we note that the flexibility in its optical and spectral characteristics allow applying our design to a wide range of problems in which spatially resolved spectro-polarimetry is required.

BIBLIOGRAPHY

Bazzon, A., H. M. Schmid, and D. Gisler (2013). „Measurement of the earthshine polarization in the B, V, R, and I band as function of phase." In: *ArXiv e-prints*. arXiv: 1306.1218 [astro-ph.EP].

Briot, D. et al. (2014). „Present and Future Detection of Terrestrial Biomarkers on Earthshine." In: *IAU Symposium*. Ed. by N. Haghighipour. Vol. 293. IAU Symposium, pp. 65–67. DOI: 10.1017/S1743921313012544.

Carroll, James D. (2009). „A new definition of life." In: *Chirality* 21.3, pp. 354–358. ISSN: 1520-636X. DOI: 10.1002/chir.20590. URL: http://dx.doi.org/10.1002/chir.20590.

Dereniak, E. L. (2005). „Infrared spectro-polarimeter." In: *Infrared Photoelectronics*. Ed. by A. Rogalski, E. L. Dereniak, and F. F. Sizov. Vol. 5957. Proc. SPIE, pp. 202–211. DOI: 10.1117/12.623389.

Duursma, E. and M. Boisson (1994). „Global oceanic and atmospheric oxygen stability considered in relation to the carbon cycle and to different time scales." In: *Oceanologica Acta* 17, pp. 117–141.

Hagen, Nathan and Michael W. Kudenov (2013). „Review of snapshot spectral imaging technologies." In: *Optical Engineering* 52.9, pp. 090901–090901. DOI: 10.1117/1.OE.52.9.090901. URL: http://dx.doi.org/10.1117/1.OE.52.9.090901.

Hansen, J. E. and J. W. Hovenier (1974). „Interpretation of the polarization of Venus." In: *Journal of Atmospheric Sciences* 31, pp. 1137–1160. DOI: 10.1175/1520-0469(1974)031<1137:IOTPOV>2.0.CO;2.

Harten, Gerard van et al. (2014). „Spectral line polarimetry with a channeled polarimeter." In: *Appl. Opt.* 53.19, pp. 4187–4194. DOI: 10.1364/AO.53.004187. URL: http://ao.osa.org/abstract.cfm?URI=ao-53-19-4187.

Hough, James (2006). „Polarimetry: a powerful diagnostic tool in astronomy." In: *A&G* 47.3, pp. 3.31–3.35. DOI: 10.1111/j.1468-4004.2006.47331.x. eprint: http://astrogeo.oxfordjournals.org/content/47/3/3.31.full.pdf+html. URL: http://astrogeo.oxfordjournals.org/content/47/3/3.31.abstract.

Jones, Stephen, Frank Iannarilli, and Paul Kebabian (2004). „Realization of quantitative-grade fieldable snapshot imaging spectropolarimeter." In: *Opt. Express* 12.26, pp. 6559–6573. DOI: 10.1364/OPEX.12.006559. URL: http://www.opticsexpress.org/abstract.cfm?URI=oe-12-26-6559.

Karalidi, T., D. M. Stam, and J. W. Hovenier (2012a). „Looking for the rainbow on exoplanets covered by liquid and icy water clouds." In: *A&A* 548, A90, A90. DOI: 10.1051/0004-6361/201220245. arXiv: 1211.1293 [astro-ph.EP].

Karalidi, T. et al. (2012b). „Observing the Earth as an exoplanet with LOUPE, the Lunar Observatory for Unresolved Polarimetry of Earth." In: *ArXiv e-prints*. arXiv: 1203.0209 [astro-ph.EP].

Keller, C. U. (2006). „Design of a polarimeter for extrasolar planetary systems characterization." In: *Society of Photo-Optical Instrumentation Engineers (SPIE) Conference Series*. Vol. 6269. Proc. SPIE, 62690T. DOI: 10.1117/12.671472.

Kudenov, M. W. and E. L. Dereniak (2012). „Compact real-time birefringent imaging spectrometer." In: *Optics Express* 20, p. 17973. DOI: 10.1364/OE.20.017973.

Kudenov, M. W. et al. (2009). „White light Sagnac interferometer for snapshot linear polarimetric imaging." In: *Optics Express* 17, p. 22520. DOI: 10.1364/OE.17.022520.

Kudenov, Michael W. et al. (2011). „White-light channeled imaging polarimeter using broadband polarization gratings." In: *Appl. Opt.* 50.15, pp. 2283–2293. DOI: 10.1364/AO.50.002283. URL: http://ao.osa.org/abstract.cfm?URI=ao-50-15-2283.

Mishchenko, M. I. et al. (2007). „Accurate Monitoring of Terrestrial Aerosols and Total Solar Irradiance: Introducing the Glory Mission." In: *Bulletin of the American Meteorological Society* 88, p. 677. DOI: 10.1175/BAMS-88-5-677.

Narita, N. et al. (2015). „Titania may produce abiotic oxygen atmospheres on habitable exoplanets." In: *Scientific Reports* 5, 13977, p. 13977. DOI: 10.1038/srep13977. arXiv: 1509.03123 [astro-ph.EP].

Oka, Kazuhiko and Takayuki Kato (1999). „Spectroscopic polarimetry with a channeled spectrum." In: *Opt. Lett.* 24.21, pp. 1475–1477. DOI: 10.1364/OL.24.001475. URL: http://ol.osa.org/abstract.cfm?URI=ol-24-21-1475.

Packham, C. et al. (2010). „Polarization Gratings: A Novel Polarimetric Component for Astronomical Instruments." In: *PASP* 122, pp. 1471–1482. DOI: 10.1086/657904.

Pallé, E. (2010). „Earthshine observations of an inhabited planet." In: *EAS Publications Series*. Ed. by T. Montmerle, D. Ehrenreich, and A.-M. Lagrange. Vol. 41. EAS Publications Series, pp. 505–516. DOI: 10.1051/eas/1041041. arXiv: 0906.0570 [astro-ph.EP].

Pallé, E. and P. R. Goode (2009). „The Lunar Terrestrial Observatory: Observing the Earth using photometers on the Moon's surface." In: *Advances in Space Research* 43, pp. 1083–1089. DOI: 10.1016/j.asr.2008.11.022.

Parol, F. et al. (2004). „Review of capabilities of multi-angle and polarization cloud measurements from POLDER." In: *Advances in Space Research* 33, pp. 1080–1088. DOI: 10.1016/S0273-1177(03)00734-8.

Rodenhuis, M. et al. (2012). „The extreme polarimeter: design, performance, first results and upgrades." In: *Ground-based and Airborne Instrumenta-*

tion for Astronomy IV. Vol. 8446. Proc. SPIE, p. 84469I. DOI: 10.1117/12.927203. arXiv: 1211.6300 [astro-ph.IM].

Seager, S. et al. (2005). „Vegetation's Red Edge: A Possible Spectroscopic Biosignature of Extraterrestrial Plants." In: *Astrobiology* 5, pp. 372–390. DOI: 10.1089/ast.2005.5.372. eprint: astro-ph/0503302.

Snik, F., T. Karalidi, and C. U. Keller (2009). „Spectral modulation for full linear polarimetry." In: *ArXiv e-prints*. arXiv: 0903.2735 [physics.optics].

Snik, F. and C. U. Keller (2013). „Astronomical Polarimetry: Polarized Views of Stars and Planets." In: *Planets, Stars and Stellar Systems. Volume 2: Astronomical Techniques, Software and Data*. Ed. by T. D. Oswalt and H. E. Bond, p. 175. DOI: 10.1007/978-94-007-5618-2_4.

Snik, F. et al. (2014). „Mapping atmospheric aerosols with a citizen science network of smartphone spectropolarimeters." In: *Geophys. Res. Lett.* 41, pp. 7351–7358. DOI: 10.1002/2014GL061462.

Sparks, W.B. et al. (2009). „Circular polarization in scattered light as a possible biomarker." In: *Journal of Quantitative Spectroscopy and Radiative Transfer* 110.14-16. XI Conference on Electromagnetic and Light Scattering by Non-Spherical Particles: 2008, pp. 1771–1779. ISSN: 0022-4073. DOI: 10.1016/j.jqsrt.2009.02.028. URL: http://www.sciencedirect.com/science/article/pii/S0022407309000909.

Stam, D. M. (2008). „Spectropolarimetric signatures of Earth-like extrasolar planets." In: *A&A* 482, pp. 989–1007. DOI: 10.1051/0004-6361:20078358. arXiv: 0707.3905.

Stam, D. M., J. W. Hovenier, and L. B. F. M. Waters (2004). „Using polarimetry to detect and characterize Jupiter-like extrasolar planets." In: *A&A* 428, pp. 663–672. DOI: 10.1051/0004-6361:20041578.

Sterzik, M. F., S. Bagnulo, and E. Palle (2012). „Biosignatures as revealed by spectropolarimetry of Earthshine." In: *Nature* 483, pp. 64–66. DOI: 10.1038/nature10778.

Tanré, D. et al. (2011). „Remote sensing of aerosols by using polarized, directional and spectral measurements within the A-Train: the PARASOL mission." In: *Atmospheric Measurement Techniques* 4, pp. 1383–1395. DOI: 10.5194/amt-4-1383-2011.

Tinbergen, J. (1996). *Astronomical Polarimetry*, p. 174.

van Harten, G. (2014). „Spectropolarimetry for planetary exploration." PhD thesis. Ph. D. thesis, University of Leiden (2014), ISBN:9789462594586. Promotor: Christoph U. Keller, Co-promotor: Frans Snik.

4

SEARCHING FOR REFLECTED LIGHT FROM τ BOÖTIS B WITH HIGH-RESOLUTION GROUND-BASED SPECTROSCOPY: APPROACHING THE 10^{-5} CONTRAST BARRIER

It is challenging to measure the starlight reflected from exoplanets because of the extreme contrast with their host stars. For hot Jupiters, this contrast is in the range of 10^{-6} to 10^{-4}, depending on their albedo, radius and orbital distance. Searches for reflected light have been performed since the first hot Jupiters were discovered, but with very limited success because hot Jupiters tend to have low albedo values due to the general absence of reflective cloud decks. The aim of this study is to search for reflected light from τ Boo b, a hot Jupiter with one of the brightest host stars. Since its discovery in 1997, it has been the subject of several reflected-light searches using high-dispersion spectroscopy. Here we aim to combine these data in to a single meta-analysis. We analysed more than 2,000 archival high-dispersion spectra obtained with the UVES, ESPaDOnS, NARVAL UES and HARPS-N spectrographs during various epochs between 1998 and 2013. Each spectrum was first cleaned of the stellar spectrum and subsequently cross-correlated with a PHOENIX model spectrum. These were then Doppler shifted to the planet rest-frame and co-added in time, weighted according to the expected signal-to-noise of the planet signal. We reach a 3σ upper limit of the planet to star contrast of 1.5×10^{-5}. Assuming a planet radius of 1.15 R_J, this corresponds to an optical albedo of 0.12 between 400-700 nm. This low albedo is in line with secondary eclipse and phase curve observations of other hot Jupiters using space-based observatories, as well as theoretical predictions of their reflective properties.

Hoeijmakers, Snellen and van Terwisga.
Accepted for publication in A&A.

4.1 INTRODUCTION

Since the discovery of the first hot Jupiters, multiple attempts have been made to detect starlight reflected off their atmospheres using ground-based facilities (e.g. Charbonneau et al., 1999; Collier Cameron et al., 1999; Collier Cameron et al., 2000; Leigh et al., 2003a; Rodler et al., 2010; Rodler et al., 2013a). However these studies have all resulted in non-detections and upper limits. To date, the only ground-based measurement of reflected light of an exoplanet is claimed by Martins et al. (2015), who report a detection of 51 Pegasi b.

A detection of direct reflected light can be used to constrain the reflectivity (albedo), as well as its spectral and directional dependence. This is an important observable because it is directly related to the global surface and/or atmospheric properties of the planet. This is exemplified by bodies in the solar system: lunar regolith appears dark at intermediate phase angles and preferably scatters light into either the forward or backward direction. The icy moons in the outer solar system have albedos close to 1.0, whereas rocky cometary nuclei may reflect only a few percent of the incoming light. Jupiter and Saturn have an orange hue due to organic hazes, while Uranus and Nepture are blue due to deep Rayleigh scattering combined with absorption by methane at red wavelengths (see e.g. Atreya et al., 1985; Wagener et al., 1986; Moses et al., 1995; Irwin et al., 2017)

Because exoplanets are unresolved, the albedo spectrum as a function of orbital phase is one of the few observables that can be used to constrain its physical nature. The Bond albedo, the fraction of incoming stellar energy that is reflected into space, is an important physical quantity because it is the principal component of the radiative energy budget of the planet.

4.1.1 *Albedo measurements of exoplanets*

For the current generation of telescopes, the angular distances between extrasolar planets and their host stars are generally too small to be spatially resolved. Moreover, the host stars are many orders of magnitude brighter than their planets, making these notoriously difficult to detect. Therefore in most cases, the presence of an orbiting planet needs to be inferred by measuring its indirect effect on the light of the host star. The transit and radial velocity methods have been the most successful in terms of yield (Schneider, 2011). These methods were first successfully applied by (Charbonneau et al., 1999) and (Mayor et al., 1995) respectively, and are mostly sensitive to gas giants in close-in orbits. Such hot Jupiters are relatively rare, but are overrepresented in the known exoplanet population because of this detection bias (see e.g. Howard et al., 2012; Fressin et al., 2013). In principle, hot Jupiters are

also the most favourable targets to search for reflected light: they intercept a relatively large fraction of the stellar flux due to their large radii and short orbital distances, potentially optimising the contrast between the planet and its star (Charbonneau et al., 1999). As follows below, this contrast is a direct proxy for the albedo of the planet.

In relating the contrast to the underlying physical parameters (albedo, planet radius and orbital distance), we adopt the notation and terminology used by Charbonneau et al. (1999) and Haswell (2010). The contrast ϵ is defined as the ratio of the starlight reflected by the planet to the total flux of the star as a function of wavelength and phase angle α,

$$F_p(\lambda) = \epsilon(\lambda) F_*(\lambda) \Phi_\alpha(\lambda) \tag{4.1}$$

where $F_*(\lambda)$ and $F_p(\lambda)$ are the observed spectra of the star and planet, and $\Phi_\alpha(\lambda)$ is the phase function which describes what fraction of light is scattered into any direction as determined by the global scattering properties of the surface and the atmosphere. α is the phase angle at which the planet is observed, and is defined as:

$$\cos(\alpha) = -\sin(i)\sin\left(2\pi\varphi - \frac{1}{2}\pi\right) \tag{4.2}$$

where φ is the orbital phase of the planet between 0 and 1 and i is the orbital inclination. Φ equals unity for a fully illuminated planet seen face-on ($\alpha = 0$) and less than unity for larger phase angles.

ϵ depends on the geometric albedo $p(\lambda)$, the radius R_p and the orbital distance a of the planet and is typically on the order of 10^{-5} for hot Jupiters:

$$F_p(\lambda) = p(\lambda)\left(\frac{R_p}{a}\right)^2 \Phi_\alpha(\lambda) F_*(\lambda) \tag{4.3}$$

The geometric albedo is defined as the fraction of incident light that is scattered back into the direction of the star, compared to that of an isotropically scattering (Lambertian) disk with the same cross-section as the planet[1]. The geometric albedo is not the same as the Bond albedo - which is defined as the fraction of the incident stellar energy that is scattered back into space, and which is a crucial factor for determining the equilibrium temperature of the planet. Although important, the Bond albedo is technically very challenging to determine because it requires measurements of the reflective properties of the planet at all phase angles and wavelengths. Instead, the geometric

1 Eq. 4.3 follows from the formal definition of the geometric albedo, which is counter-intuitive considering the fact that p can be greater than 1.0. See Seager (2010) for a thorough explanation of the geometric albedo.

albedo and the phase function can be measured directly, and both can be used to estimate the Bond albedo. Throughout this paper, albedo refers to the wavelength-dependent geometric albedo unless explicitly stated otherwise.

The albedo of a transiting hot Jupiter can readily be inferred from the depth of the secondary eclipse. Successful measurements are all attributed to space telescopes, such as Kepler, MOST, CoRoT, EPOXI and the Hubble space telescope (see e.g. Rowe et al., 2008; Christiansen et al., 2010; Alonso et al., 2009b; Alonso et al., 2009a; Santerne et al., 2011; Désert et al., 2011; Kipping et al., 2011; Coughlin et al., 2012; Esteves et al., 2013; Evans et al., 2013; Gandolfi et al., 2013; Morris et al., 2013; Demory, 2014; Shporer et al., 2015; Angerhausen et al., 2015; Gandolfi et al., 2015, and others). These have shown that hot Jupiters are generally dark, in line with theoretical models of the scattering properties of their atmospheres (e.g. Marley et al., 1999; Sudarsky et al., 2000; Burrows et al., 2008; Heng et al., 2013). However, hot Jupiters with effective temperatures in the range of T~2000 - 3000 K can glow considerably at optical wavelengths, contaminating reflected starlight with intrinsic thermal emission. This has complicated the retrieval of the albedo from secondary eclipse measurements for the hottest planets (Snellen et al., 2009; Snellen et al., 2010a; Cowan et al., 2011; Kipping et al., 2011; Demory et al., 2011; Esteves et al., 2013; Hu et al., 2015).

High-resolution spectroscopy offers an alternative way to discern the reflected planet light from the much brighter host star. Upon reflection by the planet, the starlight experiences a Doppler shift equal to the radial component of the planet's orbital velocity. As hot Jupiters generally have orbital velocities in excess of ~ 100 km s^{-1}, these Doppler shifts are well resolved by modern Echelle spectrographs with spectral resolutions of $R = \frac{\lambda}{\Delta\lambda} > 50,000$. Using the known orbital parameters, spectra taken at any orbital phase can be shifted back to the rest frame of the planet and subsequently co-added in time. Over the past 20 years there have been a number of attempts to detect the reflected light of hot Jupiters in this way, but besides the detection of 51 Peg b claimed by Martins et al. (2015), these have all resulted in upper limits on the planet-to-star contrast (see e.g. Charbonneau et al., 1999; Collier Cameron et al., 2000; Collier Cameron et al., 2002; Leigh et al., 2003a; Leigh et al., 2003b; Rodler et al., 2008; Rodler et al., 2010). The main results of these searches for reflected light using ground-based high-resolution spectroscopy are summarized in Table 4.1.

Planet	**Reference**	ϵ	**Confidence**	**Phase-function**	i (K_p)	R_p (R_J)	p
τ Boo b	Charbonneau et al. (1999)	$< 5 \times 10^{-5}$	99%	Lambertian	$\sim 45°$	1.2	<0.3
	Collier Cameron et al. (2000)	$< 3.5 \times 10^{-5}$	99.9%	Lambertian	$\sim 40°$	1.2	<0.22
	Leigh et al. (2003a)	$< 5.61 \times 10^{-5}$	99.9%	Venus-like	36°	1.2	<0.39
	Rodler et al. (2010)	$< 5.1 \times 10^{-5}$	99.9%	Venus-like	46°	1.2	<0.40
HD 75289 b	Leigh et al. (2003b)	$< 4.18 \times 10^{-5}$	99.9%	Venus-like	(127km/s)	1.6	<0.12
	Rodler et al. (2008)	$< 6.7 \times 10^{-5}$	99.9%	Venus-like	(129km/s)	1.2	<0.46
υ And b	Collier Cameron et al. (2002)	$< 5.85 \times 10^{-5}$	99.9%	Venus-like	(135km/s)	-	-
51 Peg b	Martins et al. (2015)	$6.0 \pm 0.4 \times 10^{-5}$	3.7σ	Lambertian	(132km/s)	1.9 ± 0.3	0.5

Table 4.1: Results of previous high-resolution searches for reflected light of non-transiting hot Jupiters. The last four columns indicate the assumed phase function, the best-fit orbital inclination i (or equivalent: the best-fit semi-amplitude K_p of the radially projected orbital velocity) and the inferred limiting combination of planet radius and grey albedo. The works that use Venus-like phase functions use an empirical model formulated by Hilton (1992). The only work in this list that claims an actual measurement of ϵ is the work by Martins et al. (2015). All other studies report upper limits. The upper limit by Collier Cameron et al. (2000) was adjusted by Leigh et al. (2003a) and is therefore superseded by it. The limit quoted from Charbonneau et al. (1999) is inferred from the inclination-dependent contrast curve presented in their work.

4.1.2 *The τ Boo system*

τ Boötis b was discovered in 1997 along with two other hot Jupiters (Butler et al., 1997). It orbits a bright ($V_{mag} = 4.5$) F8 main-sequence star located 15.6 pc from Earth, but was found not to transit (Baliunas et al., 1997). This star is one of the most metal-rich exoplanet hosts, and is orbited by a resolved M-dwarf companion at a distance of 240 AU (Hale, 1994; Patience et al., 2002). The properties of the system are listed in Table 4.2.

τ Boo was observed by the MOST spacecraft for 37.5 days in 2004 and 2005 to monitor its variability. Searching this data for evidence of planet-to-star interaction, Walker et al. (2008) found a variable region on the stellar surface that is synchronized with the orbital period of the planet, and is likely magnetically induced. From spectro-polarimetric observations, Donati et al. (2008) were able to map the magnetic field of the star and found evidence for differential rotation, with the rotation period varying from 3.0 to 3.9 days from equator to pole, consistent with the orbital period of the planet. This synchronization of star and planet has important consequences for the reflection spectrum. As seen from Earth, the stellar spectrum is rotationally broadened with $v \sin(i) = 15$ km s^{-1}. However, since the planet co-rotates with the stellar surface, the star does not rotate from the perspective of the planet. Therefore, the reflected light spectrum is not expected to be strongly rotationally broadened, resulting in the absorption lines being significantly more narrow than those in the stellar spectrum as observed from Earth. The reflected stellar absorption lines are only broadened by the axial rotation ($v \sin(i) = 1.24$ km s^{-1}) of the planet itself (Rodler et al., 2010; Brogi et al., 2013). Techniques that aim to detect the absorption lines of the planet are therefore particularly sensitive for this system, owing to the fact that the planet and the star are tidally locked.

4.1.3 *Searches for reflected light of τ Boo b*

As τ Boo is such a bright star, efforts to detect the reflection spectrum of the planetary companion quickly commenced after its discovery in 1997. The first search for reflected light was performed by Charbonneau et al. (1999), who observed the system for three consecutive nights with the HIRES spectrograph at the 10-m Keck Observatory, between 465.8 nm and 498.7 nm. By fitting a scaled, Doppler-shifted version of a stellar template to each individual spectrum, they constrained ϵ to be less than 5×10^{-5} to 8×10^{-5}, depending on the orbital inclination which was unknown at the time. Assuming a radius of $1.2 R_J$, the albedo was constrained to $p < 0.3$. Collier Cameron et al. (1999) analysed 48 hours of high-resolution spectra obtained by the now decommissioned Utrecht Echelle Spectrograph (UES) at the 4.2-m William Herschel

Parameter	**Sym.**	**Value**
Visible magnitude[a]	V	4.50
Distance (pc)[b]	d	15.60 ± 0.17
Effective temperature (K)[c]	T_{eff}	6399 ± 45
Luminosity $(L_\odot)$[c]	L_*	3.06 ± 0.16
Mass $(M_\odot)$[c]	M_*	1.38 ± 0.05
Radius $(R_\odot)$[c]	R_*	1.42 ± 0.08
Surface gravity (cgs)[d]	$\log g$	$4.27^{+0.04}_{-0.02}$
Systemic velocity (km s^{-1})[e]	γ	-16.54 ± 0.34
Metallicity (dex)[c]	[F/H]	0.26 ± 0.03
Age (Gyr)[c]		0.9 ± 0.5
Rotation velocity (km s^{-1})[c]	$v \sin(i)$	14.27 ± 0.06
Orbital period (days)[c]	P	3.3124568 ± 0.0000069
Semi-major axis (AU)[c]	a	0.049 ± 0.003
Orbital inclination (deg)[f]	i	44.5 ± 1.5
Eccentricity[c]	e	0.011 ± 0.006
Mass (M_J)[c]	M_p	6.13 ± 0.17
Phase zero-point (HJD)[f]	T_0	$2,455,652.108 \pm 0.004$

Table 4.2: Properties of the star τ Boo (upper part) and τ Boo b (lower part).

a : Adopted from Valenti et al. (2005).
b : Adopted from van Belle et al. (2009).
c : Adopted from Borsa et al. (2015).
d : Adopted from Takeda et al. (2007).
e : Adopted from Nidever et al. (2002).
f : Adopted from Brogi et al. (2012).

Telescope on La Palma, Spain. Following a similar procedure as Charbonneau et al. (1999), they detected a signal equivalent to $\epsilon = 1.9 \pm 0.4 \times 10^{-4}$ between 456 nm and 524 nm. These authors explained the discrepancy between their results and those of Charbonneau et al. (1999) by the assumption of a different phase-function, differences in their template fitting procedure and a different way of treating systematics. However, after obtaining more data with the same instrument in early 2000, they were unable to reproduce this signal, this time constraining ϵ to 3.5×10^{-5} (Collier Cameron et al., 2000). Again assuming a planetary radius of $R_p = 1.2 R_J$, this resulted in an albedo of $p < 0.22$. In 2003, the same group combined and re-analysed all data they obtained from 1998 to 2000 with the UES, and adjusted their 3σ upper limit to $\epsilon < 5.61 \times 10^{-5}$, assuming an orbital inclination of $i = 39°$ (Leigh et al., 2003a).

In 2007, Rodler et al. (2010) obtained two nights of high-resolution spectra with the UVES spectrograph at the UT2 of the VLT. Following the fitting method of Charbonneau et al. (1999), their analysis constrained the planet-to-star contrast ratio to 5.1×10^{-5} to 5.7×10^{-5} between 425 to 632 nm, depending on the assumed wavelength dependence of the albedo, and assuming an orbital inclination of $i = 60°$ and a planet radius of $R_p = 1.2 R_J$.

In 2011, Brogi et al. (2012) and Rodler et al. (2012) independently observed τ Boo with the CRyogenic InfraRed Echelle Spectrograph (CRIRES) mounted on UT1 at the VLT, both targeting the CO absorption band at 2.3 μm in the planet's intrinsic thermal spectrum. By cross-correlating their spectra with a CO model template, both groups were able to significantly retrieve the planet's CO absorption at 6σ and 3.4σ confidence respectively. The Doppler shift of this CO spectrum revealed the radially projected velocity semi-amplitude K_p of the planet. Together with the known orbital velocity v_{orb} and under the assumption of a circular orbit, this directly yields the orbital inclination i:

$$K_p = v_{orb} \sin(i) = \frac{2\pi a}{P} \sin(i). \tag{4.4}$$

These observations thus constrained the orbital inclination of τ Boo b to $i = 44.5 \pm 1.5°$ and $i = 47^{\circ +7}_{-6}$ respectively. For the first time, a non-transiting hot Jupiter was detected directly, and the degeneracy between M_p and i that is inherent to the radial velocity method could be broken. In the case of a small spin-orbit misalignment angle, the stellar rotation velocity of $v \sin(i) = 15$ km s^{-1} is consistent with an orbital period of 3.3 days, providing an independent confirmation of synchronization of the stellar rotation with the orbital period of the planet (Brogi et al., 2012). Rodler et al. (2013b) proceeded to re-analyse their UVES data with the known orbital inclination and an updated set of orbital parameters. Using the same fitting procedure as used in

Rodler et al. (2012), they were not able to significantly detect the reflection spectrum of the planet.

In this work, we perform a meta search for reflected light from τ Boo b by combining data from the UVES, ESPaDOnS, NARVAL UES and HARPS-N spectrographs during various epochs between 1998 and 2013. Section 4.2 describes the observations and data analysis. In Section 4.3 we present our results and possible caveats, the implications of which are discussed in Section 4.4.

4.2 OBSERVATIONS

τ Boo has been observed as part of several observing campaigns, and previous studies have shown that reflected light from the planet is too faint to be detected in a single night of data. In this analysis we therefore combine the archival high-resolution, high-signal-to-noise optical spectra obtained with the UVES spectrograph at the 8-m VLT/UT2 (Dekker et al., 2000), the ESPaDOnS spectropolarimeter at the 3.6-m CFHT (Donati, 2003), the NARVAL spectropolarimeter at the 2-m TBL (Aurière, 2003), the UES spectrograph at the 4-m WHT (Walker et al., 1986) and the HARPS-N spectrograph at the 3.6-m TNG (Cosentino et al., 2012). These contain the vast majority of all high-resolution observations of this system, except those that form the basis of Charbonneau et al. (1999) because these HIRES data were not preserved digitally and are likely lost (David Charbonneau, private communication). Table 4.3 presents an overview of all 25 datasets that are analysed in this work, with Fig. 4.2 showing the orbital phase coverage of all of the data.

4.2.1 *UES data of τ Boo*

Soon after the discovery of τ Boo b, Collier Cameron et al. (2000) initiated an observing campaign to search for the reflected light of τ Boo b using the Utrecht Echelle Spectrograph mounted on the William Herschel Telescope at the Roche de Los Muchachos observatory on La Palma. They observed the τ Boo system for 17 complete and partial nights during three observing seasons in the years 1998, 1999 and 2000, obtaining 893 spectra in total[2]. The raw data are available in the online data archive of the Isaac Netwon Group of telescopes [3] and were reduced in a standard way using IRAF version 2.16.1. In the analysis we treat each night of observations as an independent dataset, and use 63 to 67 spectral orders[4] ranging from 407 nm to 649 nm at a spectral resolution of $R = 53,000$. During the data reduction, we discarded 60 of the

2 These observations are described in detail by Leigh et al. (2003a).
3 http://casu.ast.cam.ac.uk/casuadc/ingarch/query
4 Depending on the signal-to-noise of the bluest and reddest orders.

893 spectra that were visibly affected by poor observing conditions, including the entire nights of April 13, 1998 and June 4, 1999. In total, the remaining data consist of 68.54 hours of observations.

4.2.2 *ESPaDOnS & NARVAL data of τ Boo*

The NARVAL and ESPaDOnS spectro-polarimeters are nearly identical fiber-fed bench-mounted echelle spectrographs, located at the 3.6-m Canadian French Hawaiian Telescope and the 2-m Telescope Bernard Lyot on Pic du Midi in the French Pyrenees respectively. Reduced observations of τ Boo obtained by the ESPaDOnS and NARVAL instruments are publicly available via the Polar Base online database (Petit et al., 2014)[5]. The data were originally taken to study time variations in the magnetic field of the star (Donati et al., 2008; Fares et al., 2009). We downloaded all 751 polarization spectra that were taken during multiple programmes between March 2005 and January 2011. Querying the Polar Base database for τ Boo returns a total of 971 spectra. 751 of these are individual polarization channels, while 220 are intensity channels that are obtained by combining multiple polarization channels and thus contain no independent information. All spectra have a wavelength coverage from 369.45 nm to 1048.5 nm at a spectral resolution of $R = 65,000$, with exposure times between 150 and 600 seconds, resulting in a continuum signal-to-noise between 100 and 1000 per pixel. Although each exposure is formatted as a single 1D spectrum, the 40 individual echelle orders are not stitched together and were retrieved from the downloaded reduced data files. The wavelength coverage of the data is shown in Figure 4.1.

Of the 751 spectra in total, 229 were taken on three consecutive nights in March 2005, while the other 522 spectra were obtained at various time intervals between June 2006 and January 2011, containing between 1 and 25 exposures at a given night. The three consecutive nights obtained in 2005 were treated as three individual datasets. The automatic pipelines used to reduce the data has caused the presence of negative values in some orders at the edges of the waveband (orders 1-3 and 37-39). Any spectral orders with such artefacts were discarded from the analysis. We chose to split the groups of ESPaDOnS + NARVAL spectra into four separate sets which were analysed independently of each other (each containing observations taken within a period of approximately one month), because our analysis relies on the time-stability of the stellar spectra (see Section 4.3). We chose to disregard 131 exposures that were obtained sparsely over longer periods of time. In total, the data used in our analysis consist of 49.85 hours of observations.

5 http://polarbase.irap.omp.eu/

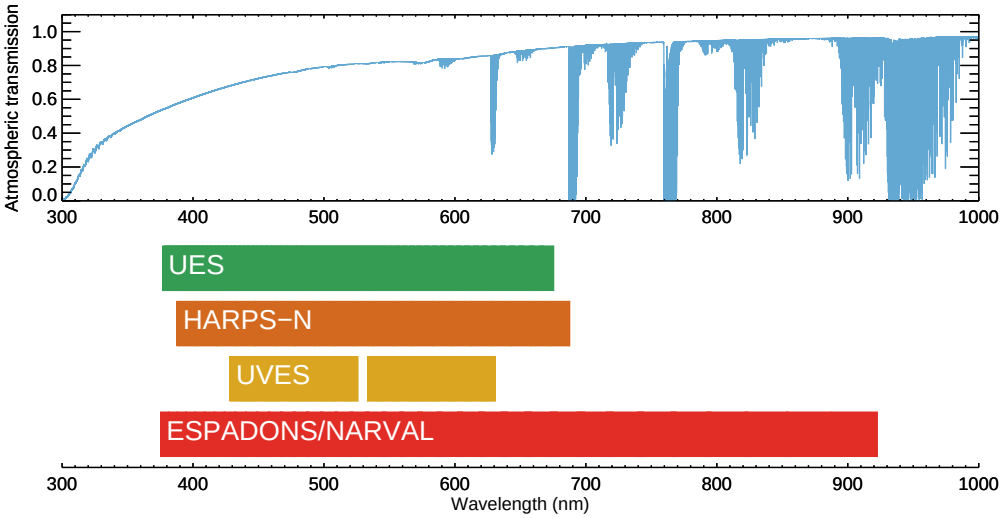

Figure 4.1: Wavelength coverage of the data. The top panel indicates the transmission function of the Earth's atmosphere, and the bottom panel shows the wavelength coverage of the data from the four instruments used in this work. Telluric contamination adversely affects our analysis, but regions that contain telluric lines are down-weighted by our analysis procedure according to the effect of the telluric lines on the cross-correlation function (see Section 4.3).

4.2.3 *UVES data of τ Boo*

τ Boo was observed with UVES (Dekker et al., 2000) on June 16 and 17, 2007 by Rodler et al. (2010)[6]. These consist of 422 1D spectra covering a wavelength range between 427.88 nm and 630.72 nm at a resolution of $R = 110,000$. The individual echelle orders were stitched together by the data reduction pipeline, hence each downloaded spectrum covers the full bandwidth of the instrument set-up. We chose to slice the spectra into 21 band-passes (hereafter referred to as 'Orders', even though these slices technically do not exactly match the echelle orders of the UVES spectrograph) that we analyse independently from each other.

The two nights cover orbital phases between $0.29 < \varphi < 0.35$ and $0.59 < \varphi < 0.66$ respectively (by convention φ varies between 0 and 1, with inferior conjunction as zero point). This timing was chosen by the observers to maximize the fraction of the day-side of the planet in view, while ensuring that the planet has an appreciable radial velocity, allowing the reflected spectrum to be discerned from the spectrum of the star through its relative Doppler-shift.

6 ESO programme 079.C-0413(A). Data obtained from the ESO Science Archive Facility.

4.2.4 *HARPS-N data of τ Boo*

The τ Boo system is being monitored using the HARPS-N spectrograph at the 3.6-m Telescopio Nationale Galileo at Roche de los Muchachos Observatory on La Palma as part of the GAPS programme to characterize known exoplanet host stars and search for additional planetary companions using the standard radial velocity technique, astroseismology and the Rossiter-McLaughlin effect (see e.g. Covino et al., 2013; Desidera et al., 2013; Sozzetti et al., 2013). To date, the TNG data archive includes 531 exposures of the τ Boo system. The first 285 of these were publicly available and were obtained in the second half of April and the first half of May of 2013. These were initially analysed by Borsa et al. (2015) to investigate the host star, the orbit of the outer stellar companion τ Boo B, and to update the orbital ephemeris of the planet.

The reduced 1D spectra were downloaded from the TNG public data archive[7] and cover wavelengths from 387 nm to 691 nm at a spectral resolution of $R \sim 110,000$. As with the UVES data, we sliced the spectra into 21 bands that were analysed separately. Because of the highly stable nature of the HARPS-N spectrograph, we chose to group the entire time-series together and treat it as a single set. In total, these data consist of 5.14 hours of observations.

4.3 DATA ANALYSIS

The reflected planet spectrum is expected to be present in the data at a level of $\epsilon \sim 10^{-5}$ times the stellar spectrum, assuming a planet radius and albedo in the order of $1 R_J$ and 10% respectively (see Eq. 4.3). The high-resolution spectra typically have a peak signal-to-noise of $\sim 500 - 1000$ per pixel. The sensitivity of the observations is subsequently enhanced by three orders of magnitude by combining the signal from $\sim 10^3$ individual absorption lines and the ~2100 spectra. This procedure is similar to that used in previous works that use cross-correlation at high spectral resolution (e.g. Charbonneau et al., 1999; Collier Cameron et al., 2000; Leigh et al., 2003a; Snellen et al., 2010b; Brogi et al., 2012; Rodler et al., 2012; Hoeijmakers et al., 2015). First, the stellar absorption lines need to be removed from the spectra to reveal the faint Doppler shifted copy originating from reflection by the planet. For each data set, we obtain the stellar spectrum by time-averaging the spectra, which is subsequently subtracted from the data. This procedure removes all time-constant spectral features, but not the planet's reflected spectrum because its radial velocity changes with up to 8.4 km s^{-1} per hour (~3× the full width at half maximum (FWHM) of the line-spread function at $R = 100,000$). Residual time-dependent features arise from changes in the stellar line-shapes caused by variations in spectral resolution due to weather and seeing, telluric ab-

7 http://ia2.oats.inaf.it/archives/tng

Set	Instrument	N_{exp}	t_{exp} (hr)	Epoch	φ range
1	UES	99	3.86	09-04-1998	0.42-0.53
2	UES	113	3.76	10-04-1998	0.72-0.83
3	UES	81	4.20	11-04-1998	0.03-0.13
4	UES	45	4.22	02-04-1999	0.50-0.60
5	UES	39	3.96	25-04-1999	0.44-0.54
6	UES	61	4.20	05-05-1999	0.46-0.55
7	UES	48	5.24	25-05-1999	0.48-0.58
8	UES	44	3.56	28-05-1999	0.39-0.47
9	UES	47	5.44	14-03-2000	0.27-0.37
10	UES	44	6.10	15-03-2000	0.57-0.67
11	UES	29	3.22	24-03-2000	0.29-0.39
12	UES	44	5.35	23-04-2000	0.32-0.42
13	UES	56	5.19	24-04-2000	0.62-0.73
14	UES	41	4.83	13-05-2000	0.36-0.44
15	UES	42	5.39	17-05-2000	0.56-0.65
16	ESPaDOnS	76	6.11	23-03-2005	0.07-0.16
17	ESPaDOnS	76	6.33	24-03-2005	0.37-0.46
18	ESPaDOnS	77	6.22	25-03-2005	0.67-0.76
19	ESPaDOnS	75	3.01	06-2006	Variable
20	UVES	105	3.88	16-06-2007	0.29-0.35
21	UVES	317	3.77	17-06-2007	0.59-0.66
22	ESPaDOnS	103	7.02	07-2007	Variable
23	ESPaDOnS	142	9.33	01-2008	Variable
24	NARVAL	71	11.83	01-2011	Variable
25	HARPS-N	285	5.14	05-2013	Variable

Table 4.3: The 25 datasets analysed in this work in chronological order, showing the instrument used, the number of exposures, amount of time spent on target, the observing epoch, and the range in orbital phase covered.

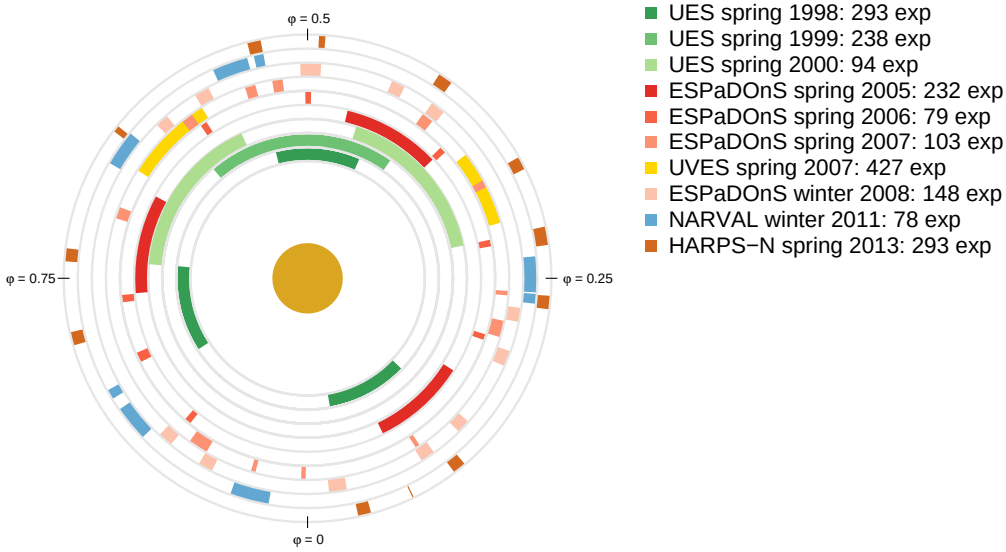

Figure 4.2: Diagram of the distribution of orbital phases covered by the observations used in this work. The data are grouped into rings, with the earliest data in the inner ring, moving outward chronologically. This diagram shows the varying nature of the observing strategies used for the different programmes. The UES obervations of 1998-2000, the ESPaDOnS observations of 2005 and the UVES observations of 2007 targeted the system consecutively for multiple hours, while the other ESPaDOnS, NARVAL and HARPS-N spectra were used to monitor the system periodically over longer periods of time. The UES and UVES observations were mostly obtained at large phase angles because these observations specifically targeted the planet's day side.

sorption, and stellar chromospheric activity. Therefore a significant part of our analysis focuses on their removal. The residual spectra are subsequently cross-correlated with a model template spectrum of the host star Doppler-shifted to the rest frame of the planet, which are then co-added in time.

Below is a description of the sequence of processing steps in detail, which are executed for each order of each dataset independently. An example of the step-wise analysis of a single spectral order is shown in Figure 4.3.

1 **Alignment of spectra:** Instabilities in tracking, weather and a changing radial velocity of the observatory with respect to τ Boo cause the spectra to drift in wavelength over the course of an observing run[8]. Such velocity variations must be removed before the time-averaged stellar spectrum can be obtained. For this purpose, we identify all stellar absorption lines stronger than 6.0% in the individual spectra, and locate their centroids by fitting a Gaussian line profile to the core of each line. Telluric lines are identified and rejected using a model telluric absorption spectrum obtained from ESO's SkyCalc Sky model calculator (Noll, S. et al., 2012; Jones, A. et al., 2013). We used these fitted line positions to align all spectra to a common reference frame. Fig. 4.4 shows the average shift needed to align each exposure of one UVES, ESPaDOnS and UES night.

2 **Wavelength solution:** We adopted the pipeline wavelength-solutions that are provided with the UVES, ESPaDOnS and HARPS-N data and shift these to the rest-frame of the star. In previous work we matched a model stellar template to the lines that we identified in step 1 (Hoeijmakers et al., 2015). However because τ Boo is a fast-rotating F-star, this matching does not result in a more accurate solution than the pipeline solutions for these datasets. To determine the rest-frame velocity of the star, we first obtained the time-averaged spectrum from the mean flux of each spectral pixel (this is also used in steps 6 and 7). This yields the highest S/N measurement of the stellar spectrum, which is subsequently cross-correlated with a model stellar template that was broadened to the rotation velocity of the star (Section 4.3.1). The resulting cross-correlation strengths are close to 1.0, confirming the quality of the pipeline wavelength solutions (see Fig. 4.8).

3 **Model injection:** We duplicate each spectral order and inject a model of the planet reflection spectrum (see Section 4.3.1) into the duplicate after appropriate broadening, Doppler-shifting and scaling:

8 For UVES in particular, instrumental instability may cause velocity shifts in the order of 1 km s^{-1}. See Czesla et al. (2015) for an extreme example in the case of transit observations of HD 189733 b.

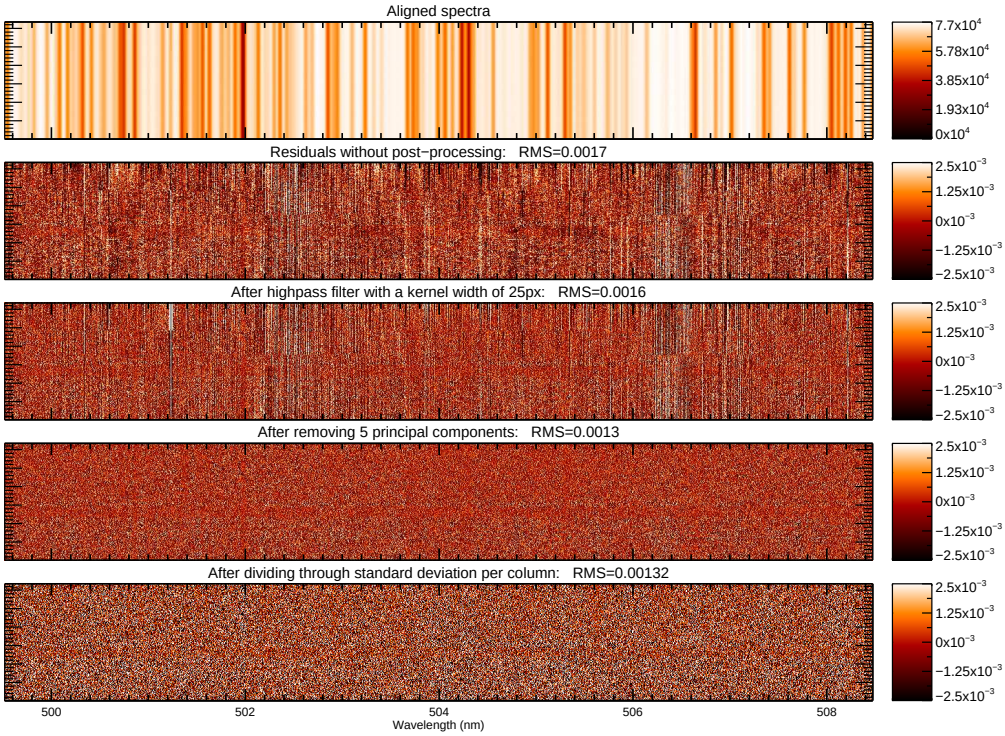

Figure 4.3: Step-wise analysis of order eight of the UVES observations obtained during the night of June 17, 2007. **First panel:** The aligned spectra (after step 1). **Second panel:** The residuals after subtracting the mean value from each column. **Third panel:** The residuals after applying a high-pass box-filter with a width of 40 pixels (roughly 40 km s^{-1}). **Fourth panel:** After subsequent removal of four principal components (step 5). **Fifth panel:** After dividing each column from the fourth panel by the standard deviation in each column (step 6). This weighs down columns that intrinsically have a lower signal-to-noise. The strong vertical structures in the third panel are telluric water lines. These are effectively removed by the principal component analysis.

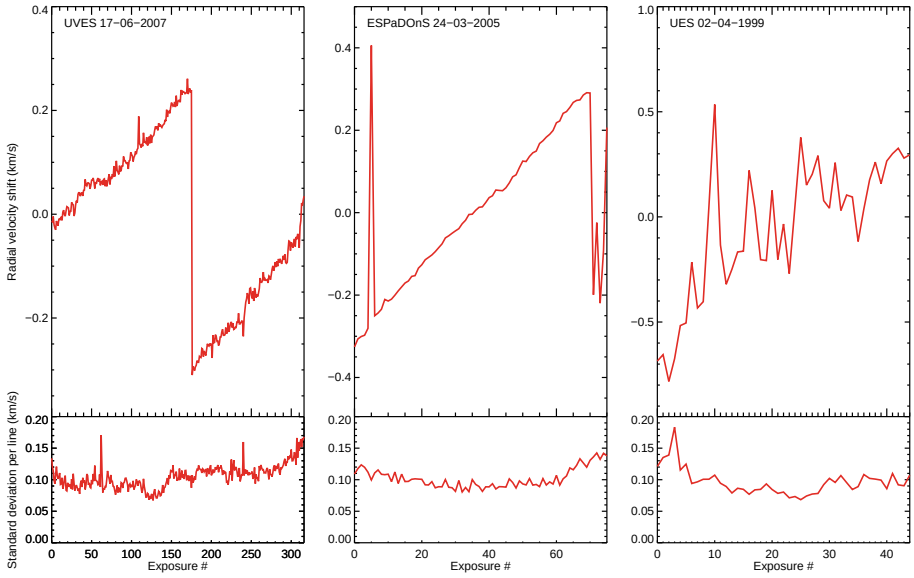

Figure 4.4: Alignment of the wavelength solution for a single UVES, ESPaDOnS and UES dataset. The top panels indicate the mean shift required to align the absorption lines to their average position. The bottom panels show the residual scatter in the line positions. On average, absorption lines are aligned to within 0.1 km s^{-1} accuracy. The wavelength solution of the UES data is less stable compared to those of UVES and ESPaDOnS, however our procedure is able to align the UES spectra to the same level of accuracy as the other instruments.

a) **Broadening:** The model spectrum is convolved with a Gaussian kernel with a FWHM of 2.61 km s^{-1} to 5.66 km s^{-1} to match the spectral resolution of the respective instrument. It is then blurred with a box-kernel with a width equal to the velocity shift of the planet during the exposure. This is calculated by multiplying the first derivative of the radial velocity at time t with the exposure time of the spectrum. The spectrum is also convolved with a rotation profile[9] with zero limb-darkening applied, with a rotation velocity of $v \sin(i) = \frac{2\pi R_p}{P} \sin(i) = 1.24$ km s^{-1}, assuming a tidally locked planet with a radius of $R_p = 1.15 R_J$ (also see Sec. 4.4.1).

b) **Doppler-shifting:** From the known ephemeris and orbital parameters (Table 4.2) we calculate the orbital phase φ and the radial velocity of the planet at the time of each observation. The model is then interpolated to the wavelength grid of the data.

c) **Scaling:** The template is subsequently multiplied by $\epsilon(\lambda)\Phi(\lambda)$. We assume that ϵ and Φ are independent of wavelength (grey) and we follow previous authors in adopting a Lambertian phase-function,

$$\Phi = \frac{\sin\alpha + (\pi - \alpha)\cos\alpha}{\pi} \tag{4.5}$$

where ϵ is set to 2.0×10^{-5} (see Figures 4.5 and 4.6). The injected and non-injected data sets are treated identically from this step onward. This simultaneous treatment of the model-injected data allows us to quantify the extent to which the data analysis procedure may influence the planet reflection spectrum, and to optimize the parameters of the procedure to maximize the strength at which the injected planet spectrum is retrieved.

4 **Removal of the stellar spectrum:** We remove the stellar spectrum by subtracting the time-averaged spectrum from each exposure, as was done in previous work (e.g. Charbonneau et al., 1999; Collier Cameron et al., 2000; Rodler et al., 2010), by subtracting the mean from each column in Fig. 4.3. This removes the time-constant components of the stellar spectrum, but leaves residual variations - for example those caused by changes in the observing conditions and/or intrinsic stellar variations (panel 2 of Fig. 4.3).

5 **Removal of time-dependent residuals:** For each spectrum we remove broad-band variations by applying a high-pass box-filter. Subsequently, we remove up to 12 principal components to eliminate variations in

9 The rotation kernel is calculated using the IDL routing LSF_ROTATE

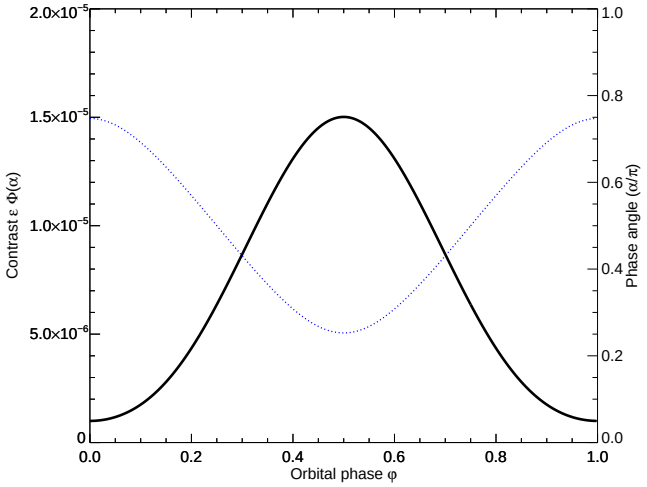

Figure 4.5: The phase-angle $\alpha(\varphi)$ as function of orbital phase φ for an orbital inclination of 44.5°(dashed line), and the resulting contrast curve assuming a Lambertian phase function $\Phi(\alpha)$ (solid line). The orbital phase is 0 when the planet is located closest to the observer (i.e. during transit for a planet with an orbital inclination of $\sim 90°$). At this moment, the phase angle is maximal and the contrast is minimal because a small part of the day-side of the planet is in view.

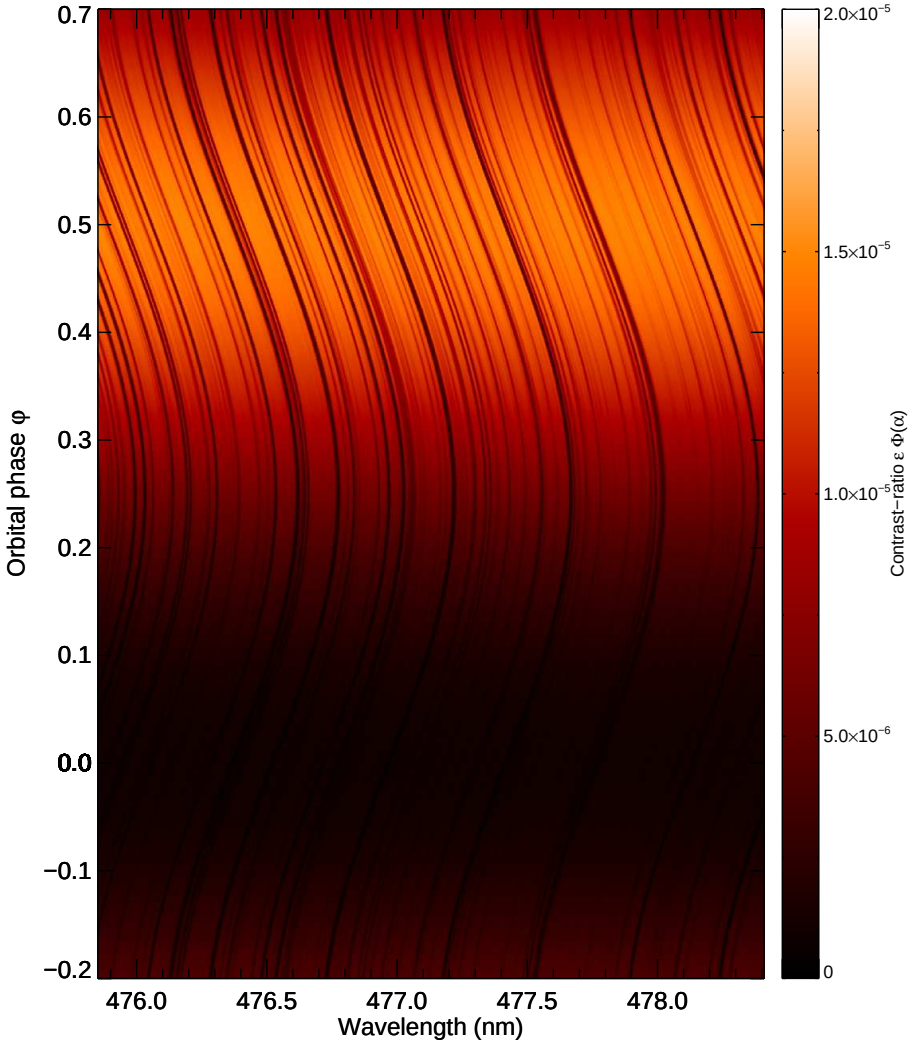

Figure 4.6: Example of the injected planet model spectra over a complete orbit, broadened to the resolution of UVES and shifted to the instantaneous radial velocity of the planet. The model spectrum is scaled to a level of $\epsilon = 2 \times 10^{-5}$, but the maximum contrast is less than that because the peak of the phase function $\Phi(\alpha)$ is less than 1.0.

telluric lines and stellar spectral line shapes. This procedure partly suppresses the planet's spectrum as well. This blind approach of cleaning the data is therefore a trade-off between effective removal of systematics and preserving the planet's reflection spectrum. To optimize the analysis, we perform a grid-search by varying the width of the box-filter and the number of principal components to remove, and choose the combination for which the signal-to-noise of the injected planet signal is maximized after cross-correlation (step 7). Finally, pixel values that are deviant by more than 5σ from the mean of their column and the two adjacent columns, are set to the mean.

6 **Normalization by signal to noise:** Stellar absorption lines and low flux levels at the edges of the blaze orders of the spectrograph cause the signal-to-noise to vary within orders. We weigh down noisy wavelengths by dividing each column to its standard deviation, as was also done in for example Snellen et al. (2010b).

7 **Cross correlation:** We cross-correlate the residuals with a template spectrum that was also used to inject the planet signal in the data in step 3 (see Section 4.3.1). The cross-correlation function (CCF) computed over a range of radial-velocities from -1600 to $+1600$ km s^{-1} in steps of 1 km s^{-1}. For each spectrum this yields 3201 cross-correlation coefficients, which are expected to peak where the template is shifted to the correct radial velocity of the planet at the time on which the spectrum was obtained. At this velocity, all absorption lines in the planet's spectrum are effectively co-added, causing an enhancement in the cross-correlation-function. The cross-correlation is performed over ± 1600 steps in radial velocity to obtain a statistical sample of cross-correlation coefficients over which the random noise level can be measured reliably.

8 **Masking stellar residuals:** At the rest-frame velocity of the star, the CCFs show residuals that arise from time variability in the stellar spectrum due to for example activity, star-spots and instabilities in the observing conditions and the instruments. These residuals take the form of a vertical structure at the rest-frame velocity of the star in the two-dimensional CCF (see Fig. 4.7). We mask out all cross-correlation coefficients within ± 35 km s^{-1} of the rest-frame velocity. This removes the planet during parts of the orbit where it has a low radial velocity (i.e. when it is in full view at $\varphi \sim 0.5$), but ensures that only exposures in which the planet's spectrum is Doppler-shifted away from the stellar line-wings are considered in the co-addition of the data.

At this stage, a CCF is associated with each spectrum, both with and without injected planet signals. For each dataset we therefore have $2 \times N_{\text{orders}} \times$

$N_{exposures}$ CCFs. For each spectrum, we measure the strength at which the injected template is retrieved by taking the difference between the injected and non-injected CCFs, and dividing with the standard deviation of the non-injected CCF. We call this quantity the 'retrievability'. To combine all of the data, the CCFs are shifted to the rest-frame velocity of the planet, weighed by their respective retrievability and summed.

This weighing scheme ensures that spectra are weighed to account for the phase function $\Phi(\alpha)$ (spectra taken near inferior conjunction will have a lower retrievability because the template spectra was injected at a lower level compared to spectra near superior conjunction), by the number of stellar spectral lines in each order (the cross-correlation is more effective at wavelengths where there are many narrow spectral lines), by all noise sources that degrade the efficiency by which the planet's spectrum can be retrieved and by differences between datasets in terms of observing conditions and data quality. Approximately 5% of all spectral orders are found not to contribute positively to the retrieved signal-to-noise of the injected signal, mostly due to the presence of strong tellurics and CCD artifacts in these spectra. These orders are discarded when co-adding the CCFs.

4.3.1 *Template spectra*

Although the stellar spectrum is present in the data at high signal-to-noise, it is strongly rotationally broadened due to the short rotation period of the star that is locked to the orbital period of the planet. Therefore, the reflected planet spectrum is expected to exhibit significantly more narrow spectral features making the broadened stellar spectrum a poor model, as already noted by previous authors (Charbonneau et al., 1999; Collier Cameron et al., 2000; Leigh et al., 2003a; Rodler et al., 2010; Rodler et al., 2013b). Therefore, we use a high spectral-resolution stellar photosphere model from the Göttingen Spectral Library generated with the PHOENIX radiative transfer code (Husser et al., 2013). The library[10] was queried with $T_{eff} = 6300$ K, $\log g = +4.50$, $[Fe/H] = +0.5$ and $[\alpha/M] = 0.0$, to match the literature values for these parameters (Table 4.2).

We tested the quality of this model by broadening it to the instrumental resolution and to the rotational velocity of the star, and subsequently cross-correlated it with the time-average spectrum of each spectral order. Examples are shown in Fig. 4.8, demonstrating that mismatches between the template and the observed stellar spectrum on average degrade the cross-correlation by only 13%. The model template we use is therefore expected to retrieve the planet's reflection spectrum with 87% efficiency, and we apply this as a correction factor on the end result (Section 4.4).

10 http://phoenix.astro.physik.uni-goettingen.de/?page_id=15

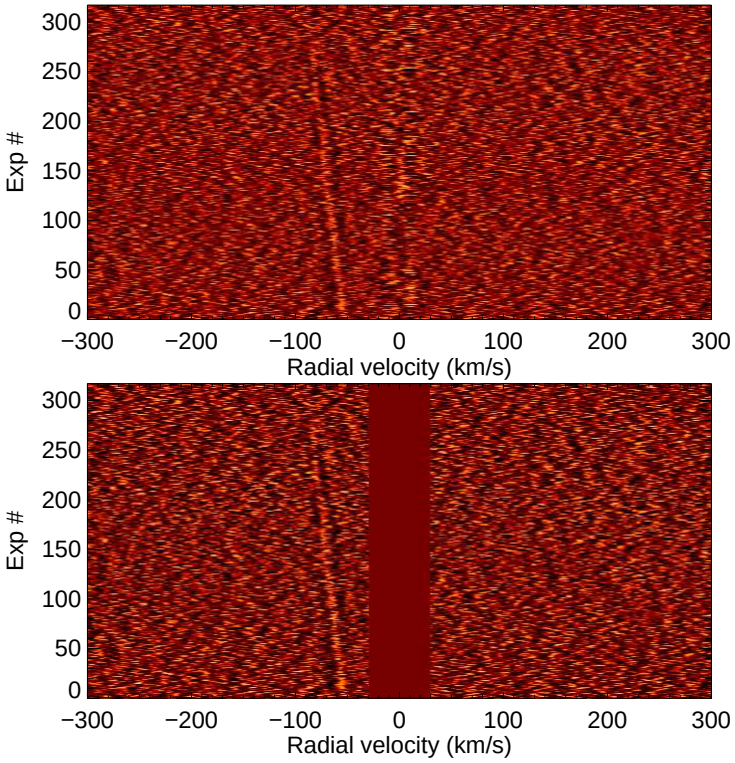

Figure 4.7: **Upper Panel:** The combined cross-correlation function of a spectral order of the second UVES night. For illustrative purposes, the planet's spectrum was injected into these data at $\epsilon = 1 \times 10^{-3}$ to show the slanted cross-correlation peak around -80 km s^{-1} due to the changing radial velocity of the planet during the observations. The vertical structure at 0 km/s is caused by residual correlation with remnants of the stellar spectrum. **Lower Panel:** The same data but with the residual stellar structure at 0 km s^{-1} masked out. This will prevent it from contaminating non-zero radial-velocities when co-adding the individual cross-correlations at the rest-frame of the planet.

We measured the gain of using an unbroadened template to be a factor ~ 2.0 in cross-correlation signal-to-noise at spectral resolutions of $55,000 - 100,000$, compared to a template broadened to $v \sin(i) = 15$ km s^{-1}.

4.4 RESULTS AND DISCUSSION

The final one-dimensional cross-correlation function obtained by combining all the analysed data is shown in Fig. 4.9. We do not detect a significant signal at the rest-frame velocity of the planet. However, the model spectrum injected at a strength of $\epsilon = 2.0 \times 10^{-5}$ is retrieved at 4.6σ significance. The noise level was measured from the one-dimensional CCF, which was evaluated over ± 1600 steps in radial velocity in order to confirm that the noise distribution is Gaussian and that the usage of a 3σ confidence threshold is prudent (see Fig. 4.10). As discussed in Section 4.3.1, the PHOENIX template retrieves the rotation-broadened stellar spectrum with an efficiency of 87%. Therefore, we establish an upper limit on ϵ of 1.5×10^{-5}at 3σ confidence.

This result depends on the assumed values of the orbital period P and phase zero-point T_0 which have associated uncertainties. We simulated the influence of uncertainties on the ephemeris by stacking the data at small deviations dP and dT_0 from the period and phase at with which it was injected, while treating K_P as a fixed constant. Fig. 4.11 shows the signal-to-noise of the retrieved signal as a function of dP and dT_0, normalized to the maximum signal-to-noise at which the signal is retrieved when $dP = dT_0 = 0$. The analysis is only mildly sensitive to errors in T_0, but could be strongly affected by an error in P because the data was taken over a 15 year timespan, spanning ~ 1500 orbital periods. We therefore repeated the complete analysis while varying the planet orbital period P within ± 15 times the standard error reported by Borsa et al. (2015), to take into account the possibility of a large unknown systematic error on the orbital period. However, the resulting upper limits are the same for all trials of dP and no planet signal is retrieved in any of these cases.

To search for a cross-correlation signal at values of K_p other than 110.2 km s^{-1} as determined by Brogi et al. (2012), we co-added all CCFs for a range of values of K_p (Fig. 4.12). No enhancement in cross-correlation is observed near the expected v_{sys} and K_p of the planet.

4.4.1 *The albedo of τ Boo b*

As follows from Eq. 4.3, the upper limit on the planet-to-star contrast ratio ϵ directly constrains the ratio of the projected area of the planet disk ($\sim R_p^2$) and the geometric albedo. Our 3σ upper limit of $\epsilon < 1.5 \times 10^{-5}$ is plotted in Fig. 4.13 as a function of both parameters and compared to the upper limits

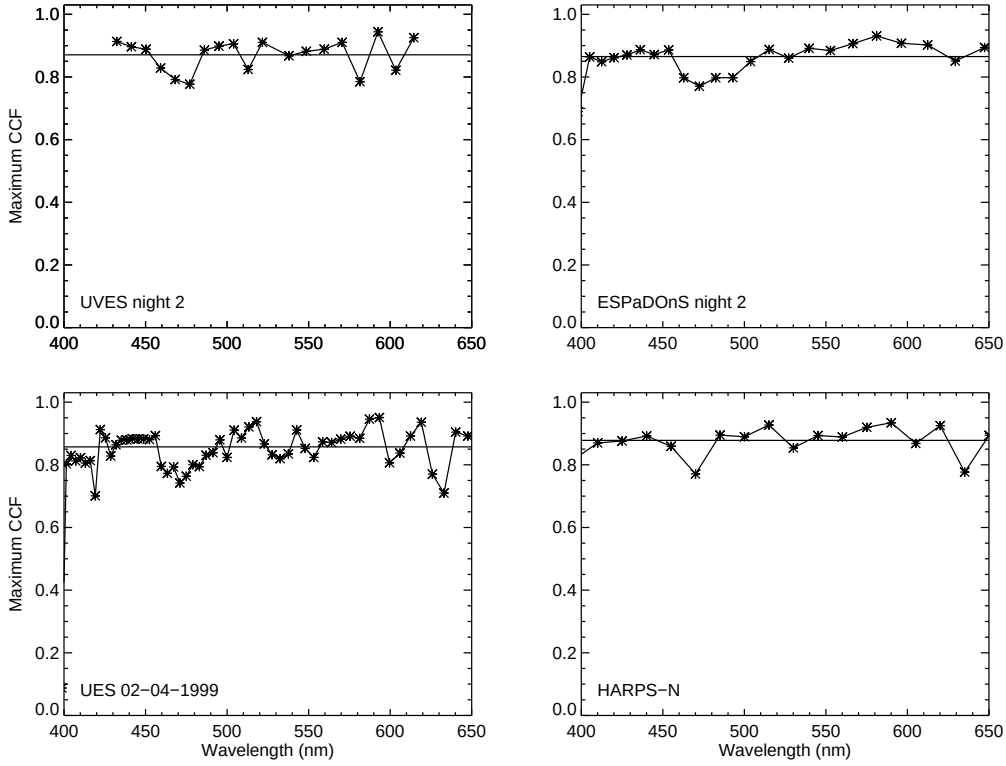

Figure 4.8: Peak cross-correlation of the time-averaged spectrum of each order with the PHOENIX template spectrum broadened to the rotation velocity of the star. In the four datasets shown, the peak cross-correlation strength averages between 0.85 and 0.90, indicating that the template retrieves the stellar spectrum at high efficiency, and therefore is an accurate model of the planet's reflection spectrum. The cross-correlation is only performed at wavelengths between 450 nm to 650 nm, because the disappearance of the continuum at short wavelengths (hence a break-down of the continuum-normalization needed to perform this cross-correlation) and the presence of tellurics at longer wavelengths cause the correlation of the template with the stellar spectrum to be degraded.

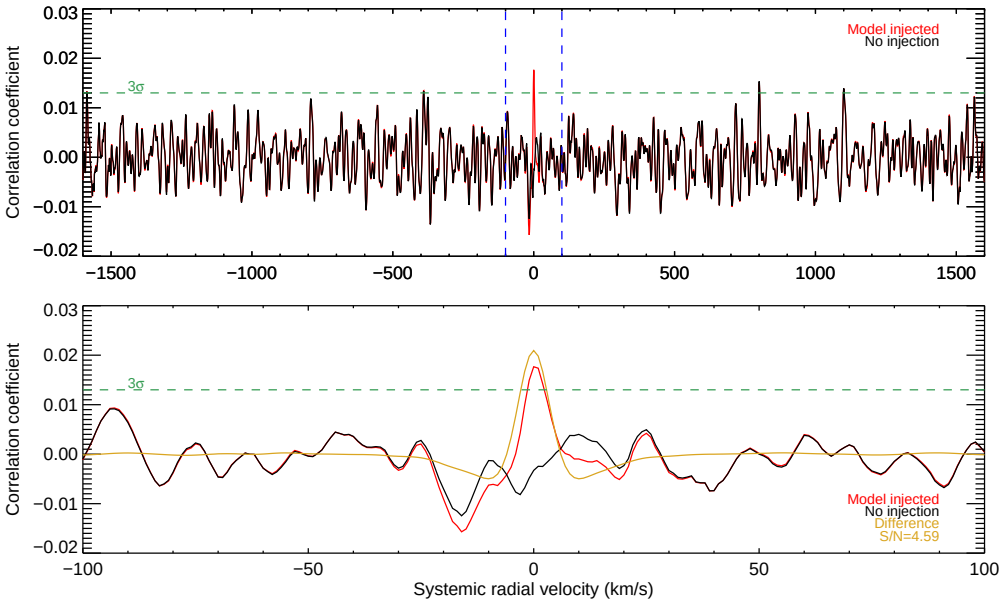

Figure 4.9: The 1D cross-correlation function after stacking all exposures in all orders of all datasets. The top panel shows the entire cross-correlation function between $\pm$1600 km s^{-1}, while the bottom panel is a zoom-in around $\pm$100 km s^{-1} for clarity. The red and black lines represent the injected and non-injected data respectively. The gold line is the difference between the two, and the dashed horizontal line is 3σ away from the mean of cross-correlation (which is around zero). The model was injected at a strength of $2 \times 10^{-5}\Phi(\alpha)$, and is retrieved at a level of 4.6σ. The corresponding 3σ upper limit of ϵ is 1.5×10^{-5}, taking into account a factor 0.87 to correct for the efficiency at which the PHOENIX template correlates with the stellar spectrum (see Section 4.3.1).

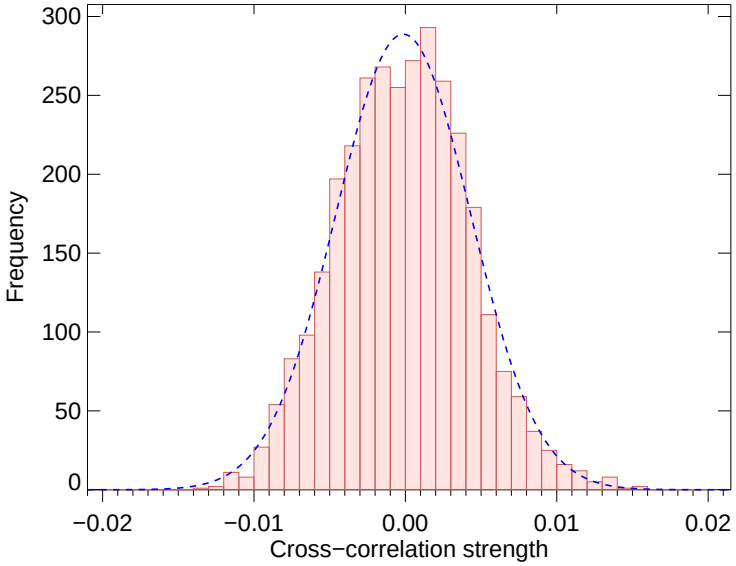

Figure 4.10: Distribution of the 1D cross-correlation function after stacking all exposures in all orders of all datasets. The blue line is a Gaussian fit to the distribution, of which the standard deviation is used to compute the confidence interval of the injected signal.

from Collier Cameron et al. (2000), Rodler et al. (2010) and Charbonneau et al. (1999), converted to 3σ confidence.

Because τ Boo b is a non-transiting planet, the radius of the planet is unknown and must be estimated from the known population of similar hot Jupiters. We select all transiting planets with masses between $3M_J$ and $9M_J$ and orbital periods less than ten days (Schneider, 2011) and find a mean radius of $1.15R_J$ for this sample of planets, the same radius as assumed by Brogi et al. (2012). Combined with the upper limit on ϵ, this places a 3σ upper limit on the geometric albedo of 0.12.

To date, optical secondary-eclipse observations have been performed of a few dozen transiting hot Jupiters, mostly with the Kepler space observatory (see e.g. Coughlin et al., 2012; Esteves et al., 2013; Angerhausen et al., 2015). These have shown that hot Jupiters tend to be dark, with typical visible-light albedo's between 0.06 and 0.11 (Demory, 2014), and even cases where the albedo has been shown to be lower than 0.04 (Kipping et al., 2011; Gandolfi et al., 2015). Our limit of $\epsilon < 1.5 \times 10^{-5}$ shows that the albedo of τ Boo b likely lies in a range that is expected for hot Jupiters and that the candidate signals observed by Leigh et al. (2003a), Rodler et al. (2010) and Rodler et al. (2013a) are false positives, as correctly hypothesized by these authors.

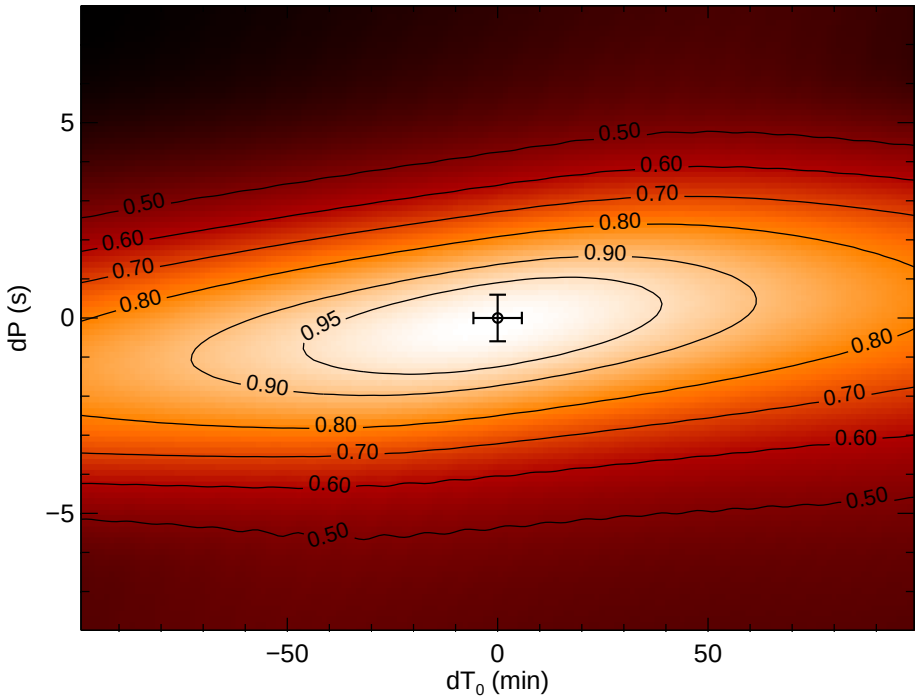

Figure 4.11: Relative decrease of the retrieved planet signal when stacking the cross-correlation functions using erroneous values for P and T_0 in the ephemeris. The retrieved signal is especially sensitive to an error in the orbital period, because the data is obtained over a 15 year timespan. The error bars indicate the known statistical errors on P and T_0 as reported by Brogi et al. (2012) and Borsa et al. (2015). We stack the data at orbital periods that are deviant from the reported period by Borsa et al. (2015) by 15, ten and five times their reported standard error, but find but find no signature of τ Boo b. This is done to take into account the possibility of a systematic error in the orbital period, which could have affected our analysis.

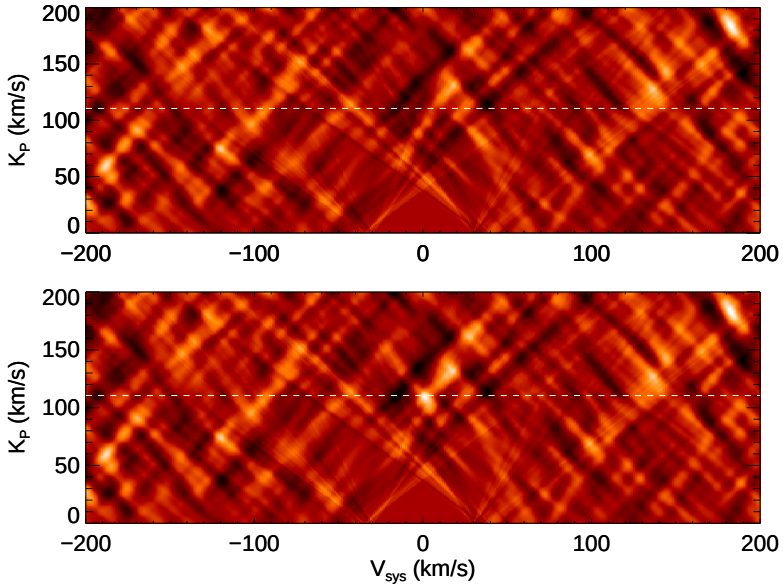

Figure 4.12: **Upper panel:** Cross-correlation strength as a function of the rest frame velocity of the system V_{sys} and the planet radial velocity amplitude K_p. **Lower panel:** The cross-correlation strength for the injected planet signal at $\epsilon = 2 \times 10^{-5}$. No significant signals are present near the expected K_p of the planet.

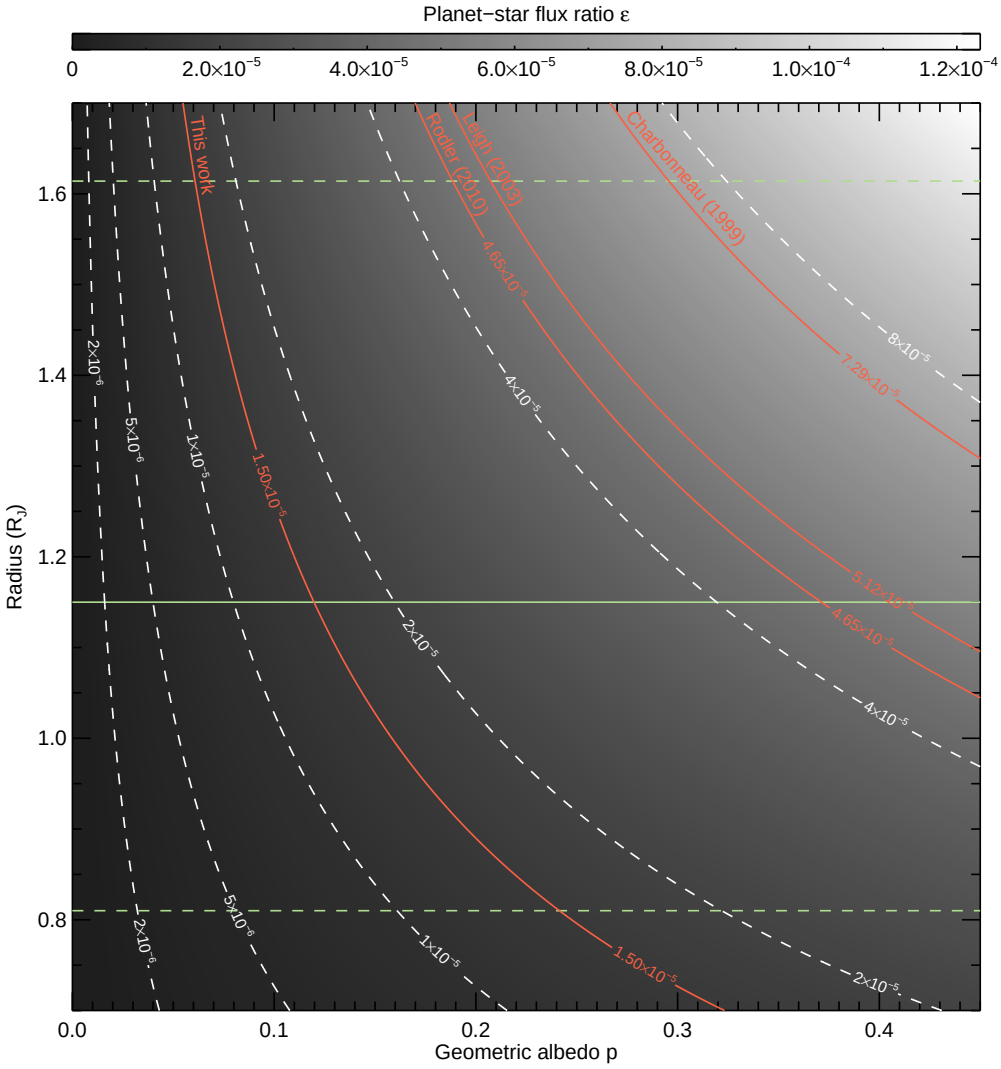

Figure 4.13: Planet-to-star contrast ratio ϵ as a function of the geometric albedo p and the planetary radius R_p. Solid contour lines indicate the contrast limit of 1.5×10^{-5} and the limits reached by Charbonneau et al. (1999), Collier Cameron et al. (2000) and Rodler et al. (2010) converted to 3σ confidence. The horizontal lines denote $R = 0.8, 1.15$ and $1.61 R_J$, which are the minimum, the mean and the maximum radii of all known transiting hot Jupiters with masses between 3 and $9 M_J$.

A low albedo can be explained by strong absorption at visible wavelengths due to the broad wings of alkali absorption lines, Rayleigh scattering by hydrogen and small condensate particles and an absence of a reflective cloud deck Heng et al. (2013). Because Rayleigh scattering dominates at short wavelengths, the planet is expected to have a blue appearance such as has been observed in HD 18733 b (Evans et al., 2013). We investigated whether such a Rayleigh scattering signal is present in the data by co-adding only the blue spectral orders at wavelengths below 450 nm, roughly matching the band within which Evans et al. (2013) measured the albedo of HD189733 b to be $p = 0.32 \pm 0.15$. Also in this case, we measure no reflection signal from the planet and constrain the average contrast between 380 nm and 450 nm to 3.2×10^{-5}.

Using similar methods and observations as used in this work, Martins et al. (2015) claim a detection of 51 Peg b at the level of $\epsilon = 6.0 \times 10^{-5} \pm 0.4$. This requires the planet to have a high albedo of p=0.5 for a $1.9 R_J$ planet, or higher if assuming a smaller radius. Their measurement is in stark contrast with the observed trend that hot Jupiters tend to have low albedo's, to which only a few exceptions are known to exist (Demory et al., 2011; Shporer et al., 2014). If 51 Peg b indeed has a phase-curve amplitude of 60 ± 4 parts per million, it would be especially suitable for follow-up with the TESS and CHEOPS space telescopes. By measuring the shape of the phase curve, such observations would help to constrain the nature of the scattering particles in the atmosphere of this planet and shed light on the causes for its anomalous brightness (Heng et al., 2013; Hu et al., 2015; Oreshenko et al., 2016).

On the other hand, τ Boo and other dark hot Jupiters around bright stars will require more sustained observations before their reflected light can be characterized at visible wavelengths. High-resolution ground-based spectroscopy may continue to provide a viable alternative to space-based observations, especially in the absence of the Kepler survey that offered the long observing baselines needed to measure the majority of optical secondary eclipses to date. Notably the ESPRESSO instrument at the VLT will be perfectly suited for these kinds of observations, owing to its high spectral resolution, superior stability and the photon-collecting power of the VLT (Martins et al., 2013).

4.5 CONCLUSIONS

Since its discovery, τ Boo has been observed in various programmes in attempts to detect its reflected light using high dispersion spectroscopy at visible wavelengths (Charbonneau et al., 1999; Leigh et al., 2003a; Rodler et al., 2010; Rodler et al., 2013b). These have constrained the planet to be fainter than 5×10^{-5} times the brightness of the star.

In this work, over 2,000 archival UVES, UES, HARPS-N, ESpaDOnS and NARVAL spectra were combined and cross-correlated with a model template to search for the reflected stellar spectrum at the rest-frame velocity of the planet. We are able to rule out planet-to-star contrasts greater than 1.5×10^{-5} at 3σ confidence, under the assumption of a lambertian phase function. The noise level of this analysis is thus 0.50×10^{-5}, on par with optical secondary eclipse measurements of other hot Jupiters by the Kepler, CoRoT and MOST space observatories. τ Boo b has a mass of $6.13 \pm 0.17 M_J$, and planets in this mass range have radii of $1.15 R_j$ on average. This radius would constrain the geometric albedo to a value of 0.12. A low albedo is consistent with theoretical predictions and a number of studies of other hot Jupiters have shown that such albedo values are indeed common.

ACKNOWLEDGEMENTS

This work is part of research programmes PEPSci and VICI 639.043.107, both funded by the Dutch Organisation for Scientific Research (NWO), as well as the Leiden Observatory Huygens Fellowship. Snellen acknowledges funding from the European Research Council (ERC) under the European Union's Horizon 2020 research and innovation programme under grant agreement No 694513. Part of this work is based on observations obtained at the Canada-France-Hawaii Telescope (CFHT) which is operated by the National Research Council of Canada, the Institut National des Sciences de l'Univers of the Centre National de la Recherche Scientique of France, and the University of Hawaii; on observations collected at the European Organisation for Astronomical Research in the Southern Hemisphere under ESO programme 079.C-0413(A); on observations obtained with HARPS-N at the TNG as part of the GAPS programme, and on observations obtained with the UES spectrograph at the WHT.

BIBLIOGRAPHY

Alonso, R. et al. (2009a). „The secondary eclipse of CoRoT-1b." In: *A&A* 506, pp. 353–358. DOI: 10.1051/0004-6361/200912102. arXiv: 0907.1653 [astro-ph.EP].

Alonso, R. et al. (2009b). „The secondary eclipse of the transiting exoplanet CoRoT-2b." In: *A&A* 501, pp. L23–L26. DOI: 10.1051/0004-6361/200912505. arXiv: 0906.2814 [astro-ph.EP].

Angerhausen, D., E. DeLarme, and J. A. Morse (2015). „A Comprehensive Study of Kepler Phase Curves and Secondary Eclipses: Temperatures and Albedos of Confirmed Kepler Giant Planets." In: *PASP* 127, p. 1113. DOI: 10.1086/683797. arXiv: 1404.4348 [astro-ph.SR].

Atreya, S. K. and P. N. Romani (1985). „Photochemistry and clouds of Jupiter, Saturn and Uranus." In: *Recent Advances in Planetary Meteorology*, pp. 17–68.

Aurière, M. (2003). „Stellar Polarimetry with NARVAL." In: *EAS Publications Series*. Ed. by J. Arnaud and N. Meunier. Vol. 9. EAS Publications Series, p. 105.

Baliunas, S. L. et al. (1997). „Properties of Sun-like Stars with Planets: ρ^1 Cancri, τ Bootis, and υ Andromedae." In: *ApJ* 474, pp. L119–L122. DOI: 10.1086/310442.

Borsa, F. et al. (2015). „The GAPS programme with HARPS-N at TNG. VII. Putting exoplanets in the stellar context: magnetic activity and asteroseismology of τ Bootis A." In: *A&A* 578, A64, A64. DOI: 10.1051/0004-6361/201525741. arXiv: 1504.00491 [astro-ph.SR].

Brogi, M. et al. (2012). „The signature of orbital motion from the dayside of the planet τ Boötis b." In: *Nature* 486, pp. 502–504. DOI: 10.1038/nature11161. arXiv: 1206.6109 [astro-ph.EP].

Brogi, M. et al. (2013). „Detection of Molecular Absorption in the Dayside of Exoplanet 51 Pegasi b?" In: *ApJ* 767, 27, p. 27. DOI: 10.1088/0004-637X/767/1/27. arXiv: 1302.6242 [astro-ph.EP].

Burrows, A., J. Budaj, and I. Hubeny (2008). „Theoretical Spectra and Light Curves of Close-in Extrasolar Giant Planets and Comparison with Data." In: *ApJ* 678, pp. 1436–1457. DOI: 10.1086/533518. arXiv: 0709.4080.

Butler, R. P. et al. (1997). „Three New "51 Pegasi-Type" Planets." In: *ApJ* 474, pp. L115–L118. DOI: 10.1086/310444.

Charbonneau, D. et al. (1999). „An Upper Limit on the Reflected Light from the Planet Orbiting the Star τ Bootis." In: *The Astrophysical Journal Letters* 522.2, p. L145. URL: http://stacks.iop.org/1538-4357/522/i=2/a=L145.

Christiansen, J. L. et al. (2010). „Studying the Atmosphere of the Exoplanet HAT-P-7b Via Secondary Eclipse Measurements with EPOXI, Spitzer, and Kepler." In: *ApJ* 710, pp. 97–104. DOI: 10.1088/0004-637X/710/1/97. arXiv: 0912.2132 [astro-ph.EP].

Collier Cameron, A. et al. (1999). „Probable detection of starlight reflected from the giant planet orbiting τ Boötis." In: *Nature* 402, pp. 751–755. DOI: 10.1038/45451. eprint: astro-ph/9911314.

Collier Cameron, A. et al. (2000). „tau Boo b: Not so bright, but just as heavy." In: *ArXiv Astrophysics e-prints*. eprint: astro-ph/0012186.

Collier Cameron, A. et al. (2002). „A search for starlight reflected from υ And's innermost planet." In: *MNRAS* 330, pp. 187–204. DOI: 10.1046/j.1365-8711.2002.05084.x. eprint: astro-ph/0110577.

Cosentino, R. et al. (2012). „Harps-N: the new planet hunter at TNG." In: *Ground-based and Airborne Instrumentation for Astronomy IV*. Vol. 8446. Proc. SPIE, p. 84461V. DOI: 10.1117/12.925738.

Coughlin, J. L. and M. López-Morales (2012). „A Uniform Search for Secondary Eclipses of Hot Jupiters in Kepler Q2 Light Curves." In: *AJ* 143, 39, p. 39. DOI: 10.1088/0004-6256/143/2/39. arXiv: 1112.1021 [astro-ph.SR].

Covino, E. et al. (2013). „The GAPS programme with HARPS-N at TNG. I. Observations of the Rossiter-McLaughlin effect and characterisation of the transiting system Qatar-1." In: *A&A* 554, A28, A28. DOI: 10.1051/0004-6361/201321298. arXiv: 1304.0005 [astro-ph.SR].

Cowan, N. B. and E. Agol (2011). „The Statistics of Albedo and Heat Recirculation on Hot Exoplanets." In: *ApJ* 729, 54, p. 54. DOI: 10.1088/0004-637X/729/1/54. arXiv: 1001.0012 [astro-ph.EP].

Czesla, S. et al. (2015). „The center-to-limb variation across the Fraunhofer lines of HD 189733. Sampling the stellar spectrum using a transiting planet." In: *A&A* 582, A51, A51. DOI: 10.1051/0004-6361/201526386. arXiv: 1509.05657 [astro-ph.SR].

Dekker, H. et al. (2000). „Design, construction, and performance of UVES, the echelle spectrograph for the UT2 Kueyen Telescope at the ESO Paranal Observatory." In: *Optical and IR Telescope Instrumentation and Detectors*. Ed. by M. Iye and A. F. Moorwood. Vol. 4008. Proc. SPIE, pp. 534–545.

Demory, B.-O. (2014). „The Albedos of Kepler's Close-in Super-Earths." In: *ApJ* 789, L20, p. L20. DOI: 10.1088/2041-8205/789/1/L20. arXiv: 1405.3798 [astro-ph.EP].

Demory, B.-O. et al. (2011). „The High Albedo of the Hot Jupiter Kepler-7 b." In: *ApJ* 735, L12, p. L12. DOI: 10.1088/2041-8205/735/1/L12. arXiv: 1105.5143 [astro-ph.EP].

Désert, J.-M. et al. (2011). „The Atmospheres of the Hot-Jupiters Kepler-5b and Kepler-6b Observed during Occultations with Warm-Spitzer and Kepler." In: *ApJ* 197, 11, p. 11. DOI: 10.1088/0067-0049/197/1/11. arXiv: 1102.0555 [astro-ph.EP].

Desidera, S. et al. (2013). „The GAPS programme with HARPS-N at TNG. II. No giant planets around the metal-poor star HIP 11952." In: *A&A* 554, A29, A29. DOI: 10.1051/0004-6361/201321155. arXiv: 1302.3093 [astro-ph.EP].

Donati, J.-F. (2003). „ESPaDOnS: An Echelle SpectroPolarimetric Device for the Observation of Stars at CFHT." In: *Solar Polarization*. Ed. by J. Trujillo-Bueno and J. Sanchez Almeida. Vol. 307. Astronomical Society of the Pacific Conference Series, p. 41.

Donati, J.-F. et al. (2008). „Magnetic cycles of the planet-hosting star τ Bootis." In: *MNRAS* 385, pp. 1179–1185. DOI: 10.1111/j.1365-2966.2008.12946.x. arXiv: 0802.1584.

Esteves, L. J., E. J. W. De Mooij, and R. Jayawardhana (2013). „Optical Phase Curves of Kepler Exoplanets." In: *ApJ* 772, 51, p. 51. DOI: 10.1088/0004-637X/772/1/51. arXiv: 1305.3271 [astro-ph.EP].

Evans, T. M. et al. (2013). „The Deep Blue Color of HD 189733b: Albedo Measurements with Hubble Space Telescope/Space Telescope Imaging Spectrograph at Visible Wavelengths." In: *ApJ* 772, L16, p. L16. DOI: 10.1088/2041-8205/772/2/L16. arXiv: 1307.3239 [astro-ph.EP].

Fares, R. et al. (2009). „Magnetic cycles of the planet-hosting star τ Bootis - II. A second magnetic polarity reversal." In: *MNRAS* 398, pp. 1383–1391. DOI: 10.1111/j.1365-2966.2009.15303.x. arXiv: 0906.4515 [astro-ph.SR].

Fressin, F. et al. (2013). „The False Positive Rate of Kepler and the Occurrence of Planets." In: *ApJ* 766, 81, p. 81. DOI: 10.1088/0004-637X/766/2/81. arXiv: 1301.0842 [astro-ph.EP].

Gandolfi, D. et al. (2013). „Kepler-77b: a very low albedo, Saturn-mass transiting planet around a metal-rich solar-like star." In: *A&A* 557, A74, A74. DOI: 10.1051/0004-6361/201321901. arXiv: 1305.3891 [astro-ph.EP].

Gandolfi, D. et al. (2015). „Kepler-423b: a half-Jupiter mass planet transiting a very old solar-like star." In: *A&A* 576, A11, A11. DOI: 10.1051/0004-6361/201425062. arXiv: 1409.8245 [astro-ph.EP].

Hale, A. (1994). „Orbital coplanarity in solar-type binary systems: Implications for planetary system formation and detection." In: *AJ* 107, pp. 306–332. DOI: 10.1086/116855.

Haswell, C. A. (2010). *Transiting Exoplanets*.

Heng, K. and B.-O. Demory (2013). „Understanding Trends Associated with Clouds in Irradiated Exoplanets." In: *ApJ* 777, 100, p. 100. DOI: 10.1088/0004-637X/777/2/100. arXiv: 1309.5956 [astro-ph.EP].

Hilton, J. L. (1992). *Explanatory Supplement to the Astronomical Almanac*. 20 Edgehill Road, Mill Valley, CA 94941, USA: University Science Books, p. 383.

Hoeijmakers, H. J. et al. (2015). „A search for TiO in the optical high-resolution transmission spectrum of HD 209458b: Hindrance due to inaccuracies in

the line database." In: *A&A* 575, A20, A20. DOI: 10.1051/0004-6361/201424794. arXiv: 1411.6017 [astro-ph.EP].

Howard, A. W. et al. (2012). „Planet Occurrence within 0.25 AU of Solar-type Stars from Kepler." In: *ApJ* 201, 15, p. 15. DOI: 10.1088/0067-0049/201/2/15. arXiv: 1103.2541 [astro-ph.EP].

Hu, R. et al. (2015). „A Semi-analytical Model of Visible-wavelength Phase Curves of Exoplanets and Applications to Kepler-7 b and Kepler-10 b." In: *ApJ* 802, 51, p. 51. DOI: 10.1088/0004-637X/802/1/51. arXiv: 1501.03876 [astro-ph.EP].

Husser, T.-O. et al. (2013). „A new extensive library of PHOENIX stellar atmospheres and synthetic spectra." In: *A&A* 553, A6, A6. DOI: 10.1051/0004-6361/201219058. arXiv: 1303.5632 [astro-ph.SR].

Irwin, P. G. J. et al. (2017). „HST/WFC3 observations of Uranus' 2014 storm clouds and comparison with VLT/SINFONI and IRTF/Spex observations." In: *Icarus* 288, pp. 99–119. DOI: 10.1016/j.icarus.2017.01.031. arXiv: 1611.03257 [astro-ph.EP].

Jones, A. et al. (2013). „An advanced scattered moonlight model for Cerro Paranal." In: *A&A* 560, A91. DOI: 10.1051/0004-6361/201322433. URL: http://dx.doi.org/10.1051/0004-6361/201322433.

Kipping, D. M. and D. S. Spiegel (2011). „Detection of visible light from the darkest world." In: *MNRAS* 417, pp. L88–L92. DOI: 10.1111/j.1745-3933.2011.01127.x. arXiv: 1108.2297 [astro-ph.EP].

Leigh, Christopher et al. (2003a). „A new upper limit on the reflected starlight from t Bootis b." In: *Monthly Notices of the Royal Astronomical Society* 344.4, pp. 1271–1282. ISSN: 1365-2966. DOI: 10.1046/j.1365-8711.2003.06901.x. URL: http://dx.doi.org/10.1046/j.1365-8711.2003.06901.x.

Leigh, C. et al. (2003b). „A search for starlight reflected from HD 75289b." In: *MNRAS* 346, pp. L16–L20. DOI: 10.1046/j.1365-2966.2003.07276.x. eprint: astro-ph/0310489.

Marley, M. S. et al. (1999). „Reflected Spectra and Albedos of Extrasolar Giant Planets. I. Clear and Cloudy Atmospheres." In: *ApJ* 513, pp. 879–893. DOI: 10.1086/306881. eprint: astro-ph/9810073.

Martins, J. H. C. et al. (2013). „Spectroscopic direct detection of reflected light from extrasolar planets." In: *MNRAS* 436, pp. 1215–1224. DOI: 10.1093/mnras/stt1642. arXiv: 1308.6516 [astro-ph.EP].

Martins, J. H. C. et al. (2015). „Evidence for a spectroscopic direct detection of reflected light from 51 Pegasi b." In: *A&A* 576, A134, A134. DOI: 10.1051/0004-6361/201425298. arXiv: 1504.05962 [astro-ph.EP].

Mayor, M. and D. Queloz (1995). „A Jupiter-mass companion to a solar-type star." In: *Nature* 378, pp. 355–359. DOI: 10.1038/378355a0.

Morris, B. M., A. M. Mandell, and D. Deming (2013). „Kepler's Optical Secondary Eclipse of HAT-P-7b and Probable Detection of Planet-induced

Stellar Gravity Darkening." In: *ApJ* 764, L22, p. L22. DOI: 10.1088/2041-8205/764/2/L22. arXiv: 1301.4503 [astro-ph.EP].

Moses, J. I., K. Rages, and J. B. Pollack (1995). „An analysis of Neptune's stratospheric haze using high-phase-angle voyager images." In: *Icarus* 113, pp. 232–266. DOI: 10.1006/icar.1995.1022.

Nidever, D. L. et al. (2002). „Radial Velocities for 889 Late-Type Stars." In: *ApJ* 141, pp. 503–522. DOI: 10.1086/340570. eprint: astro-ph/0112477.

Noll, S. et al. (2012). „An atmospheric radiation model for Cerro Paranal." In: *A&A* 543, A92. DOI: 10.1051/0004-6361/201219040. URL: http://dx.doi.org/10.1051/0004-6361/201219040.

Oreshenko, M., K. Heng, and B.-O. Demory (2016). „Optical phase curves as diagnostics for aerosol composition in exoplanetary atmospheres." In: *MNRAS* 457, pp. 3420–3429. DOI: 10.1093/mnras/stw133. arXiv: 1601.03050 [astro-ph.EP].

Patience, J. et al. (2002). „Stellar Companions to Stars with Planets." In: *ApJ* 581, pp. 654–665. DOI: 10.1086/342982. eprint: astro-ph/0207538.

Petit, P. et al. (2014). „PolarBase: A Database of High-Resolution Spectropolarimetric Stellar Observations." In: *PASP* 126, pp. 469–475. DOI: 10.1086/676976. arXiv: 1401.1082 [astro-ph.SR].

Rodler, F., M. Kürster, and J. R. Barnes (2013a). „Detection of CO absorption in the atmosphere of the hot Jupiter HD 189733b." In: *MNRAS* 432, pp. 1980–1988. DOI: 10.1093/mnras/stt462.

Rodler, F., M. Kürster, and T. Henning (2008). „HD 75289Ab revisited. Searching for starlight reflected from a hot Jupiter." In: *A&A* 485, pp. 859–864. DOI: 10.1051/0004-6361:20079175. arXiv: 0804.4609.

Rodler, F., M. Kürster, and T. Henning (2010). „τ Boötis b: Hunting for reflected starlight." In: *A&A* 514, A23, A23. DOI: 10.1051/0004-6361/200913627. arXiv: 1002.1638 [astro-ph.SR].

Rodler, F., M. Lopez-Morales, and I. Ribas (2012). „Weighing the Non-transiting Hot Jupiter τ Boo b." In: *ApJ* 753, L25, p. L25. DOI: 10.1088/2041-8205/753/1/L25. arXiv: 1206.6197 [astro-ph.EP].

Rodler, F. et al. (2013b). „The return of the mummy: Evidence for starlight reflected from the massive hot Jupiter τ Boo b?" In: *Astronomische Nachrichten* 334, p. 188. DOI: 10.1002/asna.201211744.

Rowe, J. F. et al. (2008). „The Very Low Albedo of an Extrasolar Planet: MOST Space-based Photometry of HD 209458." In: *ApJ* 689, 1345-1353, pp. 1345–1353. DOI: 10.1086/591835. arXiv: 0711.4111.

Santerne, A. et al. (2011). „SOPHIE velocimetry of Kepler transit candidates. IV. KOI-196b: a non-inflated hot Jupiter with a high albedo." In: *A&A* 536, A70, A70. DOI: 10.1051/0004-6361/201117807. arXiv: 1108.0550 [astro-ph.EP].

Schneider, J. (2011). „Defining and cataloging exoplanets: The exoplanet.eu database." In: *EPSC-DPS Joint Meeting 2011*, p. 3.

Seager, S. (2010). *Exoplanet Atmospheres: Physical Processes*.

Shporer, A. and R. Hu (2015). „Studying Atmosphere-dominated Hot Jupiter Kepler Phase Curves: Evidence that Inhomogeneous Atmospheric Reflection Is Common." In: *AJ* 150, 112, p. 112. DOI: 10.1088/0004-6256/150/4/112. arXiv: 1504.00498 [astro-ph.SR].

Shporer, A. et al. (2014). „Atmospheric Characterization of the Hot Jupiter Kepler-13Ab." In: *ApJ* 788, 92, p. 92. DOI: 10.1088/0004-637X/788/1/92. arXiv: 1403.6831 [astro-ph.EP].

Snellen, I. A. G., E. J. W. de Mooij, and S. Albrecht (2009). „The changing phases of extrasolar planet CoRoT-1b." In: *Nature* 459, pp. 543–545. DOI: 10.1038/nature08045. arXiv: 0904.1208 [astro-ph.EP].

Snellen, I. A. G., E. J. W. de Mooij, and A. Burrows (2010a). „Bright optical dayside emission from extrasolar planet CoRoT-2b." In: *A&A* 513, A76, A76. DOI: 10.1051/0004-6361/200913338. arXiv: 0909.4080 [astro-ph.EP].

Snellen, I. A. G. et al. (2010b). „The orbital motion, absolute mass and high-altitude winds of exoplanet HD209458b." In: *Nature* 465, pp. 1049–1051. DOI: 10.1038/nature09111. arXiv: 1006.4364 [astro-ph.EP].

Sozzetti, A. et al. (2013). „The GAPS Programme with HARPS-N@TNG: A Search for Additional Planets in Transiting Planet Systems." In: *European Planetary Science Congress 2013, held 8-13 September in London, UK., id.EPSC2013-940* 8, EPSC2013-940, EPSC2013–940.

Sudarsky, D., A. Burrows, and P. Pinto (2000). „Albedo and Reflection Spectra of Extrasolar Giant Planets." In: *ApJ* 538, pp. 885–903. DOI: 10.1086/309160. eprint: astro-ph/9910504.

Takeda, G. et al. (2007). „Structure and Evolution of Nearby Stars with Planets. II. Physical Properties of ˜1000 Cool Stars from the SPOCS Catalog." In: *ApJ* 168, pp. 297–318. DOI: 10.1086/509763. eprint: astro-ph/0607235.

Valenti, J. A. and D. A. Fischer (2005). „Spectroscopic Properties of Cool Stars (SPOCS). I. 1040 F, G, and K Dwarfs from Keck, Lick, and AAT Planet Search Programs." In: *ApJ* 159, pp. 141–166. DOI: 10.1086/430500.

van Belle, G. T. and K. von Braun (2009). „Directly Determined Linear Radii and Effective Temperatures of Exoplanet Host Stars." In: *ApJ* 694, pp. 1085–1098. DOI: 10.1088/0004-637X/694/2/1085. arXiv: 0901.1206 [astro-ph.SR].

Wagener, R., J. Caldwell, and K.-H. Fricke (1986). „The geometric albedos of Uranus and Neptune between 2100 and 3350 A." In: *Icarus* 67, pp. 281–288. DOI: 10.1016/0019-1035(86)90109-0.

Walker, D. D. et al. (1986). „High resolution echelle spectrographs for the Anglo-Australian Telescope coude focus and William Herschel Telescope Nasmyth focus." In: *Instrumentation in astronomy VI*. Ed. by D. L. Crawford. Vol. 627. Proc. SPIE, pp. 291–302. DOI: 10.1117/12.968103.

Walker, G. A. H. et al. (2008). „MOST detects variability on τ Bootis A possibly induced by its planetary companion." In: *A&A* 482, pp. 691–697. DOI: 10.1051/0004-6361:20078952. arXiv: 0802.2732.

5

MEDIUM-RESOLUTION INTEGRAL-FIELD SPECTROSCOPY FOR HIGH-CONTRAST EXOPLANET IMAGING: MOLECULE MAPS OF THE β PICTORIS SYSTEM WITH SINFONI

Angular Differential Imaging (ADI) and Spectral Differential Imaging (SDI) are well-established high-contrast imaging techniques but their application is challenging for companions at small angular separations from their host stars. The aim of this study is to investigate to what extent adaptive-optics assisted, medium-resolution ($R \sim 5000$) integral field spectrographs (IFS) can be used to directly detect the absorption of molecular species in the spectra of planets and substellar companions, which are not present in the spectrum of the star. We analysed archival data of the β Pictoris system taken with the SINFONI integral field spectrograph located at ESO's Very Large Telescope, originally taken to image β Pictoris b using ADI techniques. At each spatial position in the IFS, a scaled version of the stellar spectrum is subtracted from the data after which the residuals are cross-correlated with model spectra. The cross-correlation co-adds the individual absorption lines of the planet emission spectrum constructively, while this is not the case for (residual) telluric and stellar features. Cross-correlation with CO and H_2O models result in significant detections of β Pictoris b at 6.9σ and 11.0σ respectively, at an angular distance of 0.36" from the star. Correlation with a $T = 1700$K BT-Settl model provides a 14.4σ detection. This in contrast to data analysis using the LOCI (ADI) algorithm which barely reveals the planet. While the adaptive optics system only achieved modest Strehl ratios of 19-27% and a raw contrast of 1:300 at the planet position, cross-correlation achieves a 3σ contrast limit of 4.4×10^{-5} in this 2.5 hr data set. Adaptive-optics assisted, medium-resolution IFS such as SINFONI on the VLT and OSIRIS on the Keck Telescope, can be used for high-contrast imaging utilizing cross-correlation techniques for planets that are close to their star and embedded in speckle noise. We refer to this method as "molecule mapping" and advocate its application to observations with future medium resolution instruments, in particular HARMONI on the ELT and NIRSpec and MIRI on the JWST.

Hoeijmakers, Schwarz, Snellen et al.
To be submitted.

5.1 INTRODUCTION

To directly image an extrasolar planet, the light of its host star must generally be suppressed by orders of magnitude. The techniques that have been developed to do this rely on a combination of precise wave front control (adaptive optics), possible smoothing of the diffraction pattern of the telescope (pupil apodization), blocking the star with a mask (coronography) and/or by using interferometric optics to make the starlight interfere destructively with itself (phase masks). In such imaging data, residual starlight is present in the form of speckles which may mimic point-source objects, confusing the detection of companions and planets. Such residuals can be suppressed during post-processing by assuming that the pattern is fixed to the orientation of the telescope (angular differential imaging, ADI), that such a pattern scales with wavelength (spectral differential imaging, SDI), and/or by modelling the time-variability of the speckles (e.g. principal component analysis, PCA) (see e.g. Guyon, 2011; Mawet et al., 2012; Chauvin, 2016, for reviews).

So far, direct imaging detections are generally limited to a specific part of the exoplanet population: Young gas giants in wide orbits that glow by radiating out the internal heat that resulted from their formation. These planets can be resolved from their host star owing to their relatively large mutual angular separation and the fact that they are self-luminous at infrared wavelengths. Such planets can generally only be observed during the first few tens of millions of years of their lifetime, after which they have cooled too much to be detected with current facilities (see e.g. Bowler, 2016, for a review).

The desire to image cooler (i.e. older or less massive) planets that are closer to their host star is fuelling the development of new instruments, and observing and data analysis techniques. The arsenal of high-contrast imaging facilities has recently been expanded by the deployment of dedicated planet finding instruments such as the Gemini Planet Finder (Macintosh et al., 2006) at the Gemini Telescope, SPHERE (Beuzit et al., 2008) on the European Very Large Telescope (VLT), and SCExAO (Jovanovic et al., 2015) on the Subaru telescope. These instruments also have low-resolution ($R \sim 30 - 100$) spectroscopic capability - allowing the spectal characterization of directly imaged planets, achieving planet-to-star contrast ratios down to 10^{-6} at 0.2" angular separation (see e.g. Macintosh et al., 2014; Ruffio et al., 2017; Mesa et al., 2017; Currie et al., 2017).

5.1.1 *Integral field spectroscopy*

Multiple studies indicate that when high-contrast imaging is combined with high-dispersion spectroscopic techniques, the achieved contrasts can be significantly enhanced (see e.g. Sparks et al., 2002; Riaud et al., 2007; Kawahara

et al., 2014; Snellen et al., 2015; Luger et al., 2017; Wang et al., 2017). Such strategies assume that the faint planet and the much brighter star have spectral properties that are distinctly different at high spectral resolution; notably the presence of molecular absorption bands in the spectrum of the planet. Because the planet is close to the star, its spectrum is deeply embedded in speckle-noise, but it can be extracted using cross-correlation: The cross-correlation co-adds the individual absorption lines of the planet constructively, but not stellar and telluric features, or at a different radial velocity. This method has been applied successfully for the first time by Snellen et al. (2014) at high spectral resolution, albeit using the CRIRES slit spectrograph that probes only one spatial dimension. This resulted in the measurement of the spin of β Pictoris b (Snellen et al., 2014).

In this study we investigate to what extent this method can be applied to data from adaptive-optics assisted, medium-resolution ($R \sim 5000$) integral field spectrographs (IFS) - targeting molecular species in a planet atmosphere that are not present in the star throughout the two-dimensional field of view. The use of cross-correlation techniques on IFS data was first performed by Konopacky et al. (2013) and Barman et al. (2015) to detect H_2O, CO and CH_4 in the atmospheres of HR 8799 b&c using the OSIRIS integral field spectrograph at the Keck Observatory. At 1.7" and 0.96", HR 8799 b&c are widely separated from their host star (Marois et al., 2008). Such angular distances are well resolvable by modern adaptive-optics systems and the speckle-pattern can be effectively removed using ADI or SDI-based methods. However, the application of ADI and SDI are less effective at smaller angular separations because the effects of field rotation and wavelength-dependencies are limited (Fitzgerald et al., 2006; Lafrenière et al., 2007; Marois et al., 2008; Rameau et al., 2015).

We apply the cross-correlation technique to archival K-band SINFONI image cubes of the β Pictoris system and are able to extract the spectral signature of the planet β Pictoris b, while effectively removing the diffraction pattern of the star in which the planet is embedded. We refer to this technique as *molecule mapping* because it produces two-dimensional cross-correlation maps that show where in the image certain molecules are detected.

In Section 5.2 we describe the β Pictoris system. Section 5.3 describes the archival SINFONI observations used in this analysis and the data reduction. The cross-correlation procedure is described in Section 5.4, followed by the resulting cross-correlation images in Section 5.5, including a comparison with the LOCI algorithm (Lafrenière et al., 2007). Paragraphs 5.5.4 and 5.5.5 highlight potential application of molecule mapping with upcoming medium-resolution integral-field instruments on the ELT and JWST, after which the paper is summarized and concluded in Section 5.6.

5.2 THE β PICTORIS SYSTEM

In 1984, β Pictoris was the first star to be found to host a debris disk, associated with planet formation processes (Smith et al., 1984). The warped structure of the disk led to the inference of a possible planetary mass companion (Scholl et al., 1993; Roques et al., 1994; Lazzaro et al., 1994; Burrows et al., 1995; Lecavelier des Etangs et al., 1996; Mouillet et al., 1997; Augereau et al., 2001), which was discovered in 2008 (Lagrange et al., 2009; Lagrange et al., 2010) via direct imaging. The system is a member of the nearby β Pictoris moving group which has an estimated age of 24 ± 3 Myr (Bell et al., 2015). A recent estimate of the bolometric luminosity and effective temperature of the planet by Chilcote et al. (2017) of $\log\left(\frac{L_p}{L_\odot}\right) = -3.78 \pm 0.03$ and 1724 ± 15K respectively, provides a mass of $12.9 \pm 0.2 M_J$ and a radius of $1.46 \pm 0.01 R_J$ (see Table 5.1), assuming a hot-start evolution model (Baraffe et al., 2003).

β Pic b moves on a 20–26-year orbit that is highly inclined with respect to the line of sight from Earth (Wang et al., 2016). This high inclination has recently triggered a renewed interest in this system because the Hill sphere of the planet is predicted to transit the star between April 2017 and January 2018 (Lecavelier des Etangs et al., 2016; Wang et al., 2016; Kenworthy, 2017). Snellen et al. (2014) measured the projected equatorial rotation velocity of the planet, inferring a length of day of ~8 hours.

5.3 OBSERVATIONS

The β Pictoris system was observed with the SINFONI IFS (Eisenhauer et al., 2003) mounted on ESO's the Very Large Telescope in K-band on the nights of September 10 and 11, 2014 as part of ESO programme 093.C-0626(A) (P.I.: Chauvin). The observations on both nights were taken in pupil tracking mode which makes the field rotate during the observing sequence, facilitating Angular Differential Imaging. The 32x64 pixel images were taken in the highest spatial resolution mode, with each pixel covering 0.0125" by 0.025", providing a field of view (FOV) of 0.8" by 0.8" on sky. At a resolving power of $R \sim 5000$ the SINFONI spectra have a wavelength coverage from 1.929 μm to 2.472 μm with a sampling of 0.25 nm. At the time of these observations the planet was separated from the central star by approximately 0.36" (Wang et al., 2016). On the first and second night, 24 and 30 science frames were obtained respectively, spanning a total duration of 2.5 hours (see Table 5.2). During both nights, the seeing varied between 0.7" to 0.9" and the AO system delivered modest Strehl ratios between 19% and 27%. The observations on the first night were preceded by a few acquisition images after which the star was placed just outside the FOV for the rest of the sequence. During the second night both star and planet were observed continuously (see Fig. 5.1).

Parameter	Symbol	Value
Visible magnitude[a]	V	3.86
K-band magnitude[a]	K	3.48
Distance (pc)[b]	d	19.44 ± 0.05
Effective temperature (K)[c]	$T_{\rm eff}$	8052 ± 30
Mass ($M_\odot$)[d]	M_*	$1.85^{+0.03}_{-0.04}$
Metallicity (dex)[c]	[M/H]	0.05 ± 0.06
Age (Myr)[e]		24 ± 3
Rotation velocity (km s^{-1})[f]	$v \sin i$	130
Systemic velocity (km s^{-1})[g]	v	20.0 ± 0.7
Luminosity $\left(\log \frac{L}{L_\odot}\right)$[h]	L_p	-3.78 ± 0.03
K-band contrast[i]	ΔK	9.2 ± 0.1
Effective temperature (K)[h]	$T_{\rm eff}$	1724 ± 15
Surface gravity ($\log g$)[h]		4.18 ± 0.01
Angular separation (mas)[i]		356.5 ± 0.9
Position angle (deg)[j]		213.0 ± 0.2

Table 5.1: Summary of the properties of the star β Pictoris (upper part) and its planet (lower part).
a: Ducati (2002).
b: van Leeuwen (2007).
c: Gray et al. (2006).
d: Wang et al. (2016). The stellar mass was inferred from their fit to the total mass of the system minus the mass of the planet. Although the quoted confidence intervals correspond to 1σ uncertainties, the posterior distributions are non-Gaussian.
e: Bell et al. (2015).
f: Royer et al. (2007).
g: Gontcharov (2006).
h: Chilcote et al. (2017). These authors measured the luminosity from their GPI datasets, but inferred the other parameters using a hot-start evolutionary model by Baraffe et al. (2003). The reported statistical errors do not account for the model-dependency of these values.
i: Bonnefoy et al. (2011).
j: Measurements obtained by Wang et al. (2016) on November 8, 2014.

Observing night	Sept. 10, 2014	Sept. 11, 2014
N_{exp}	24	30
DIT (s)	60	2
NDIT	4	50
Airmass	1.34 - 1.15	1.49 - 1.14
PA (deg)	340.7 - 304.6	355.7 - 304.3
Strehl ratio (%)	19 - 27	20 - 25

Table 5.2: Overview of the observations of the the β Pictoris system of September 10 and 11, 2014, showing the number of exposures N_{exp}, the exposure time per dithering position (DIT), the number of dithering positions combined to make each science frame (NDIT), and the range of airmasses, position angles on sky, and approximate Strehl ratios achieved.

The raw data was downloaded from the ESO Science Archive Facility and reduced using version 3.0.0 of the SINFONI pipeline. The reduction pipeline produces a three-dimensional image cube for each science observation, with sky position in the x and y directions and wavelength in the z direction. The pipeline reduced data cubes contain NAN values at the edges of the waveband and at the location of known bad pixels. To reject these areas, we only consider wavelengths between 2.088 μm and 2.452 μm and flag any remaining NAN values (see Figure 5.2). From each science exposure we obtain the wavelength-averaged two-dimensional image. The spatial location of the star was found by fitting a two-dimensional Gaussian profile to a region of 10×10 pixels around the maximum of the PSF. We use this location as a pivot to derotate all image-cubes by their respective position angle and to align them to a common frame. We co-added all image cubes of each night to obtain two master image cubes, excluding all regions within a range of 5 pixels from the edges of the individual frames. The wavelength-averaged images of these two master cubes are shown in Figure 5.1. From the wavelength-averaged image of the second night, we constructed a curve of the raw contrast as a function of angular separation from the star, and measure the raw contrast at the separation of the planet to be 1:300 (see Figure 5.8).

We subsequently applied our cross-correlation analysis to the master cubes of both nights independently as described in the next section, and co-added the resulting cross-correlation functions into a single three-dimensional cross-correlation cube.

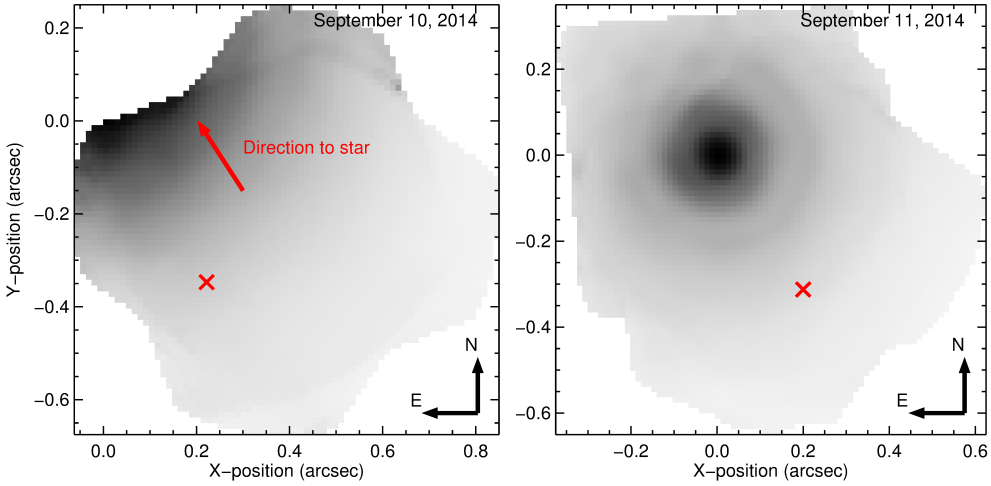

Figure 5.1: Wavelength-averaged images of the β Pictoris SINFONI data, obtained by de-rotating and stacking the exposures of each night, and taking the median flux of the spectrum at each image location. The expected position of β Pictoris b is indicated by the red crosses.

5.4 DATA ANALYSIS

5.4.1 *Removal of starlight*

The flux at each spatial position in the data cube is dominated by the spectrum of the star, showing a few stellar but mainly telluric absorption features. The steps to remove this starlight are shown in Figure 5.3. First, a high signal-to-noise master stellar spectrum is created by combining the spectra from the 1% (20) brightest pixels by first normalizing them to the same flux level and then by taking the mean of these spectra at each wavelength while rejecting $> 6\sigma$ outliers.

For each spatial position in the data cube we subsequently divide the spectrum by this master and apply a Gaussian smoothing filtering with a 1σ width of 10 wavelength steps (~ 300 km s^{-1}). The resulting function is used as a proxy for the local wavelength-dependence of the stellar diffraction pattern. The stellar master spectrum is then multiplied with this proxy and subtracted from the local spectrum. This effectively removes the starlight at each position and wavelength. As a final step, any remaining $> 6\sigma$ outliers are set to zero.

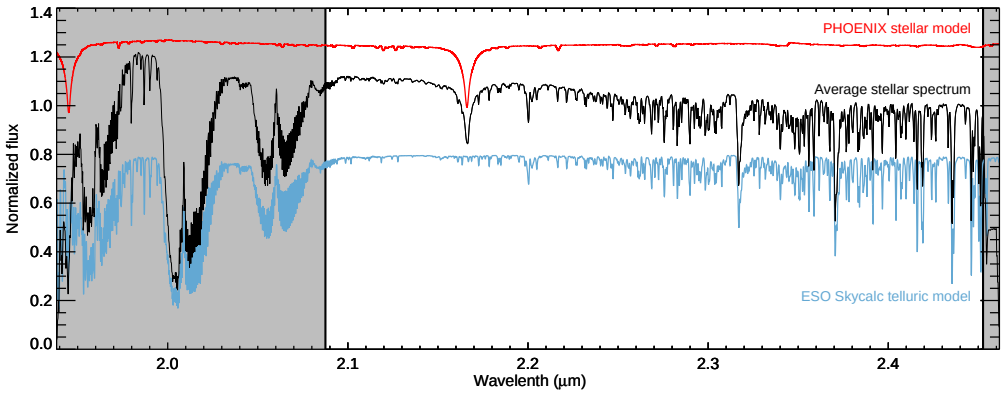

Figure 5.2: The average stellar spectrum of the master cube of the second night (black), compared with a continuum-normalized rotation-broadened PHOENIX model in red (Husser et al., 2013) and the telluric transmission spectrum as obtained using ESO SkyCalc in blue (Noll, S. et al., 2012; Jones, A. et al., 2013), both convolved to the spectral resolution of SINFONI. There are few stellar absorption lines in this wavelength range and the data is dominated by telluric absorption bands due to water, CO_2 and methane. The grey regions at the edges of the waveband were discarded due to strong telluric bands of H_2O and CO_2 or bad pixels that are close to the edges of the detector.

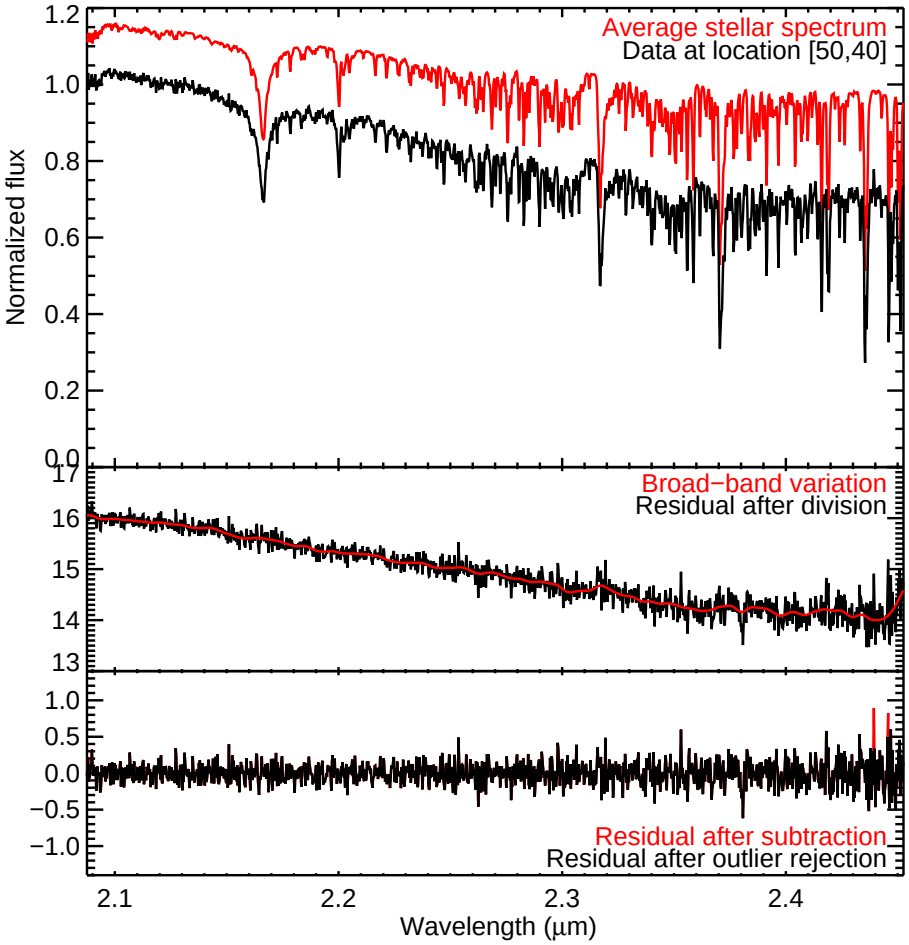

Figure 5.3: Stepwise removal of starlight from each spatial location in the data cubes. **Upper panel:** The master stellar spectrum (red) compared to the local observed spectrum (black) at spatial pixel location [50,40] of the second night. The absolute flux level of the master stellar spectrum is much greater than that at this location, so it is scaled to the level of the local spectrum for visual purposes. **Middle panel:** Ratio of the master spectrum over the local spectrum (black) after application of Gaussian smoothing (red), which is used as a proxy for the local wavelength-dependence of the stellar diffraction pattern. **Bottom panel:** Residuals obtained after subtracting the master stellar spectrum multiplied by the proxy from the local observed spectrum. Pixel values that are more than 6σ away from the mean are rejected (red).

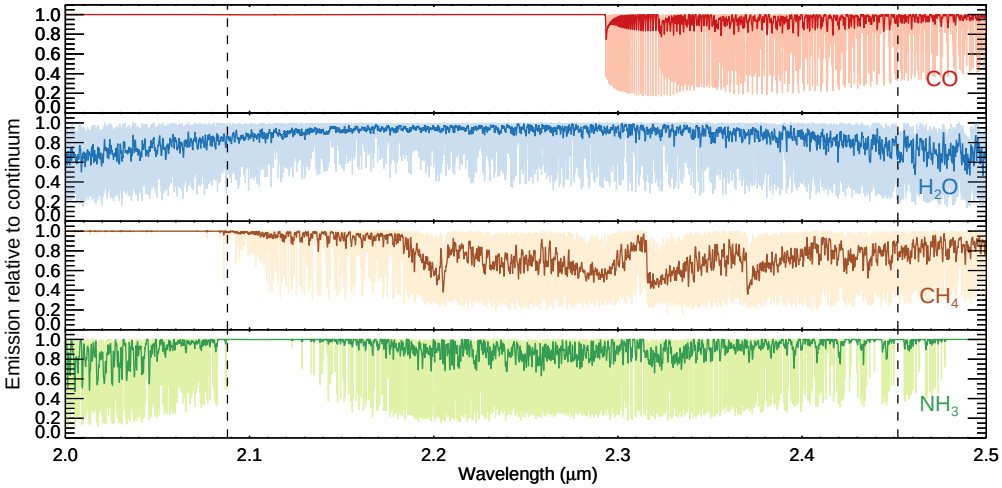

Figure 5.4: Model templates of CO, H_2O, CH_4 and NH_3 at high ($R \sim 10^6$) spectral resolution (light colour) and convolved to a spectral resolution of $R = 5000$ (dark colour). The vertical dashed lines indicate the wavelength range of the data.

5.4.2 *Cross correlation with model templates*

We search for the presence of CO, H_2O, NH_3 and CH_4 at each spatial location in the data cube by cross-correlating each local residual spectrum with a model template of each of these molecules, corresponding to ~ 1200 K emission models of the day side HD 189733, adopted from de Kok et al. (2014). In addition we cross-correlate with a grid of pre-computed BT-Settl model spectra (Allard et al., 2011)[1] with temperatures less than 3000 K and varying in surface gravity from $\log(g) = 2.5$ to 5.5.

Prior to cross-correlation, we fit and subtract the continuum of these model spectra to eliminate low-frequency variations and convolve them to a spectral resolution of $R = 5000$ (see Figure 5.4). These models are then cross-correlated with each residual spectrum over a range of velocities of $v \pm 2500$ km s^{-1} in steps of 10 km s^{-1}. The cross-correlation of the two data cubes therefore results in two cross-correlation cubes with a depth of 501 steps in radial velocity.

At the planet position, the closer the model template matches the real emission spectrum of the planet, the stronger the resulting cross-correlation signal will be. In all other spatial locations no significant cross-correlation signals are expected. The systematic radial velocity of the β Pictoris system is $+20 \pm 0.7$ km s^{-1} (Gontcharov, 2006). Using the orbital solution of Wang

1 https://phoenix.ens-lyon.fr/Grids/BT-Settl/CIFIST2011_2015/FITS/

et al. (2016), we calculate the instantaneous radial velocity of β Pic b to be ~ -9.5 km s^{-1} (the barycentric correction of -7.9 km s^{-1} has been applied by the pipeline). Therefore, the peak cross-correlation is expected to occur at a radial velocity of ~ 10 km s^{-1}, i.e. one velocity step away from zero in our cross-correlation cubes.

5.4.3 *ADI Analysis*

We also analysed the data by means of angular differential imaging using the LOCI algorithm (Lafrenière et al., 2007) to compare the performance of the molecule mapping technique. LOCI was applied independently at each wavelength with a separation criterion of 1 full-width-at-half-maximum, an optimization area of 300 FWHM and a geometry parameter of 0.5.

5.5 RESULTS AND DISCUSSION

5.5.1 *Molecule maps of the β Pictoris system*

The molecule maps at the radial velocity of the planet are shown in Figure 5.5. The maps of CO and H_2O show a significant signal at the expected position of the planet, while the planet is not detected in the maps of NH_3 and CH_4. The one dimensional cross-correlation functions at the position of the planet are shown in Figure 5.6. From these we measure the detection confidence to be 6.9σ and 11.0σ for CO and H_2O respectively, determined from the ratio of the peak to the standard deviation of the cross correlation functions at $|v| > 250$ km s^{-1}.

The non-detections of CH_4 and NH_3 are consistent with the effective temperature of the planet, which at 1724 K is expected to be too high for significant quantities of these particular molecules unless the planet is rich in respectively carbon or nitrogen (Burrows et al., 2006; Hubeny et al., 2007; Zahnle et al., 2014; Heng et al., 2016b; Heng et al., 2016a; Moses et al., 2016; Todorov et al., 2016).

5.5.2 *Cross-correlation with BT-Settl grid*

The BT-Settl model that corresponds most closely to the planet parameters observed by Chilcote et al. (2017), i.e. $T_{\rm eff}$=1700 K and $\log(g)$ =4.0, is used to produce the cross-correlation map shown in the middle panel of Figure 5.7. This model takes into account absorption from both CO and H_2O, and therefore is a more complete representation of the true planet spectrum than the individual molecule spectra. Indeed, the planet is detected at a significantly higher level of 14.4σ. The K-band contrast ratio between β Pic b and

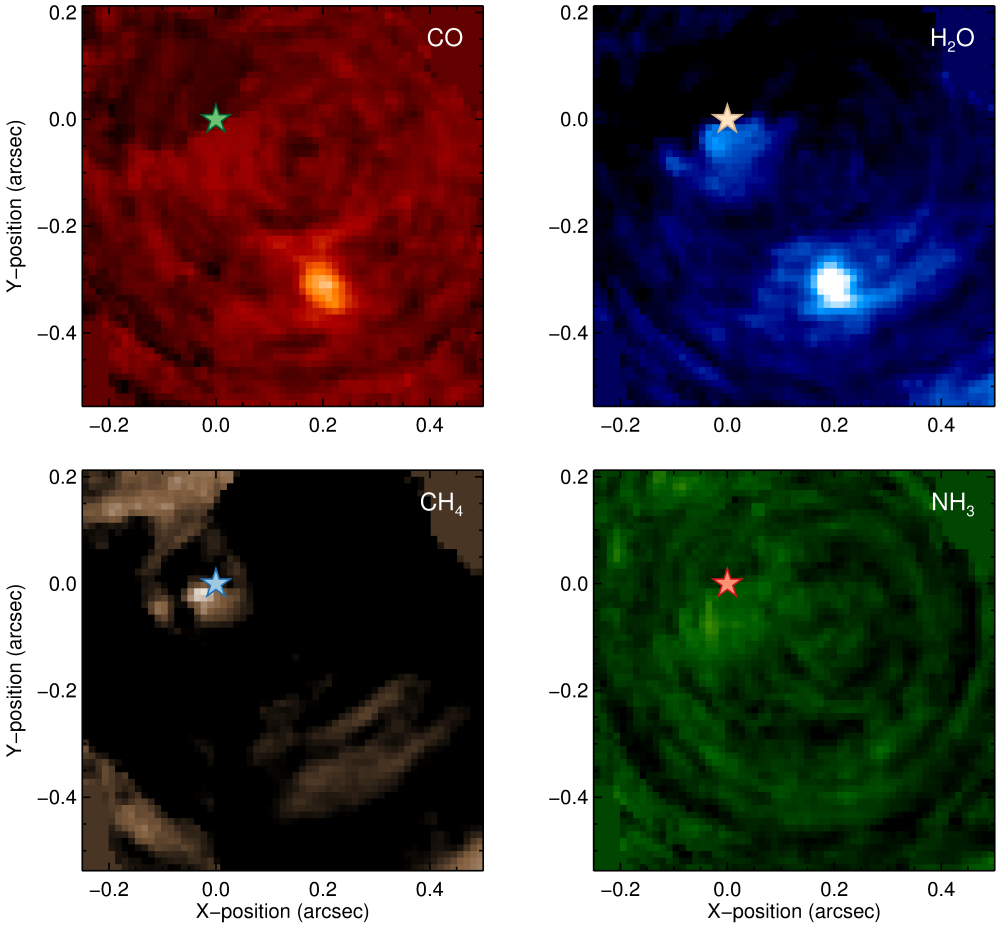

Figure 5.5: Molecule maps of CO, H_2O,CH_4 and NH_3 at $v_{sys} = 10$ km s^{-1}. In all four panels, the colours scale linearly between cross-correlation of -3σ (black) and +8σ (white). The cross-correlation enhancement caused by the planet is detected at a significance of 6.9σ and 11.0σ in the maps of CO and H_2O respectively, but not in CH_4 and NH_3.

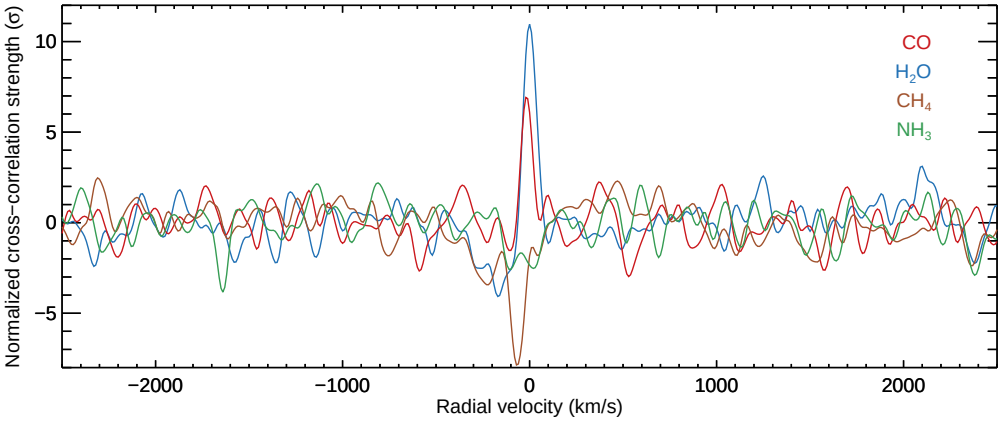

Figure 5.6: 1D cross-correlation functions of CO, H_2O, CH_4 and NH_3 at the location of the planet normalized by their noise level.

its host star is $\Delta K = 9.2 \pm 0.1$ (Bonnefoy et al., 2011). Our 14.4σ detection of the planet therefore corresponds to an achieved 3σ contrast of 4.4×10^{-5}; an improvement of a factor 75 over the raw contrast measured in Section 5.3 (see Figure. 5.8).

The left panel of Figure 5.7 shows the white-light image obtained with the LOCI algorithm for which these observations were initially intended. Although there is a clear peak at the planet position, it is difficult to assess the statistical confidence of this detection. Several other positive and negative features with similar amplitudes as that of the signal at the planet position are present in the image, in particular close to the host star.

Global atmospheric parameters such as the effective temperature, surface gravity, metallicity and abundances ratios, influence the relative strength of individual absorption lines. These may significantly influence the cross-correlation function thus making the analysis sensitive to underlying model parameters. Figure 5.9 shows the peak value of the 1D cross-correlation function with BT-Settl models with varying T_{eff} and $\log(g)$. The cross-correlation peak steeply decreases for temperatures below $\sim$ 1600 K because the strength of the water absorption features at > 2.1 µm become significantly weaker.

Above $\sim$ 2000 K, the cross-correlation peak is a shallower function of T_{eff} as the CO and H_2O absorption bands slowly diminish towards higher temperatures. Similarly, models with $\log(g)$ below 5.0 are favoured over models with higher surface gravities, due to the stronger water absorption bands relative to CO for lower values of $\log(g)$. The highest cross-correlation peak is achieved for $T_{eff} = 1700$ K and $\log(g) = 3.5$, with a signal-to-noise of 14.4σ (see Figure 5.7). Although preliminary, this analysis shows that medium resolution integral-field spectrographs can be used to characterize the funda-

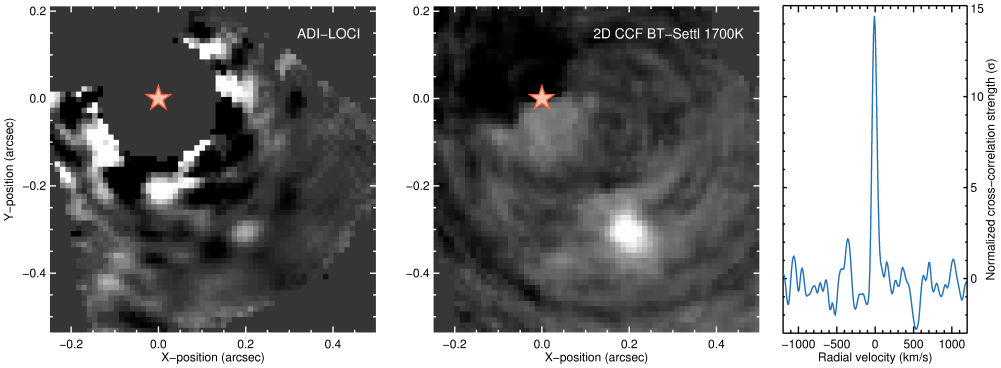

Figure 5.7: **Left panel:** White-light image obtained after co-adding the data with the LOCI algorithm. The planet is visible near [0.2",-0.3"], but is barely recovered. **Middle panel:** Cross-correlation map using the preferred BT-Settl model (T_{eff} = 1700 K and log(g) = 3.5). The grey scales are set between −3 and +14σ. **Right panel:** The one-dimensional cross-correlation function at the location of the planet. The BT-Settl model cross-correlates with the planet at a confidence of 14.4σ.

mental parameters of directly imaged companions via cross-correlation, and that molecule mapping is not limited to only the detection of molecules in the atmospheres of these objects.

5.5.3 *Residual structure in the molecule maps*

The cross-correlation map of CH_4, and to a lesser extent that of H_2O, show systematic correlation signals throughout the image. This is caused by residual telluric absorption that was incompletely or too strongly corrected by our cleaning procedure – most importantly the strong telluric CH_4 feature at 2.32 μm that dominates the absorption spectra of both hot and cold CH_4 gas. This is the result of a mismatch between the local spectra and the stellar master spectrum used to remove the starlight and notably occurs near the edges of individual frames and at the location of the star, where the signal-to-noise of the residuals is high.

We suspect that the systematic correlation signals are caused by stray light in the instrument that was not corrected by the data reduction pipeline. Such spurious light dilutes the spectra and thereby changes the relative depth of spectral lines. Because there is no one-to-one correspondence between the position of a spectrum on the CCD and the location in the image, stray light results in irregular cross-correlation patterns as can be seen in the data. A careful treatment of stray light during the data reduction may partly mitigate this problem. However, the spatial structure of the systematic correlation sig-

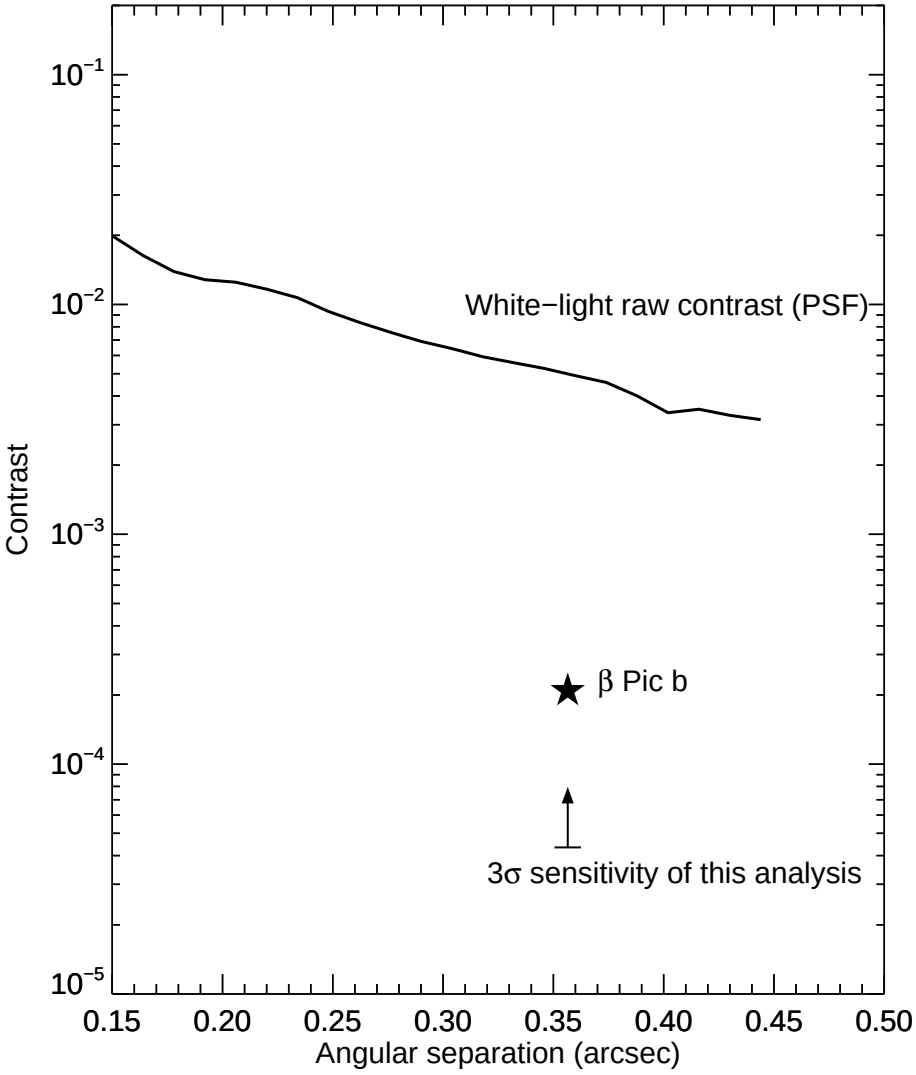

Figure 5.8: Raw-contrast curve obtained by averaging the flux from the second night in annuli with widths of 20 mas around the central star, normalized by the peak flux. The actual K-band contrast of β Pic b is adopted from Bonnefoy et al. (2011) and the 3σ sensitivity limit of this analysis is derived from our 14.4σ detection of the planet.

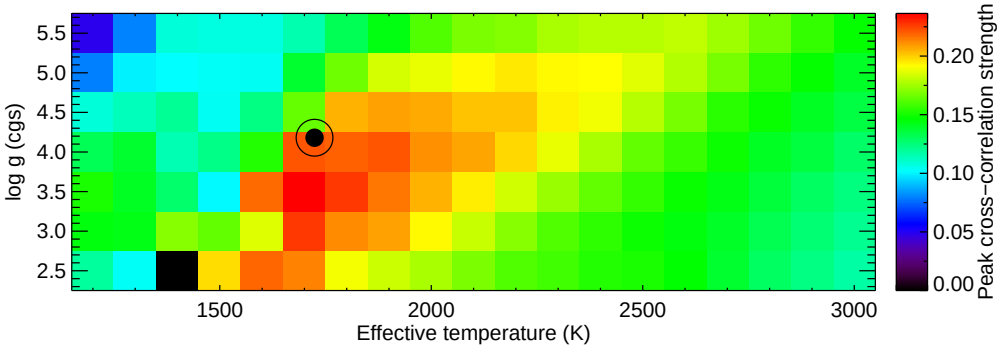

Figure 5.9: The planet cross-correlation peak as a function of BT-Settl models with varying T_{eff} and $\log(g)$. The cross-correlation peak steeply decreases for temperatures below ~ 1600 K because the strength of the water absorption features at > 2.1 μm become significantly weaker. All molecular bands diminish above temperatures of ~ 2000 K, causing a slow decrease of the cross-correlation function at higher temperatures. The black circle corresponds to the values reported by Chilcote et al. (2017).

nals is clearly not point-like and is therefore not readily confused with that of a planet.

5.5.4 *Molecule mapping from space with NIRSpec and MIRI*

Molecule mapping provides new possibilities for high-contrast imaging using R ~ 5000 IFSs, also on instruments aboard space-based observatories. Both NIRSpec and MIRI on the James Webb Space Telescope (JWST), to be launched in 2018, have integral-field capabilities. In IFS mode, NIRSpec covers wavelengths from 0.7 and 5.27 μm at a spectral resolution of ~ 2.700 with a spatial sampling of 0.1" × 0.1". MIRI has a similar IFS mode, operating between 4.89 μm to 28.45 μm at a spectral resolution varying from 3320 at short wavelengths to 1460 at longer wavelengths. The waveband is divided into four channels with increasing slit-size, the bluest channel having a spatial resolution of 0.196", and the reddest a spatial resolution of 0.276". Although the spatial sampling of both NIRSpec and MIRI is significantly more coarse than that of SINFONI in 25 mas plate-scale mode, objects with a separation down to 0.1" can theoretically be resolved by the IFS of NIRSpec, and separations down to 0.2" can be resolved by MIRI at 5 μm .

5.5.5 *Molecule mapping with HARMONI at the ELT*

The primary spectroscopic capability of the ELT in the near infra-red will be fulfilled by the HARMONI integral-field spectrograph. HARMONI will cover wavelengths between 0.47 to 2.45 μm at spectral resolutions ranging from $R \sim 400$ to $\sim 20,000$ in individual Z, J, H and K bands. The highest possible spatial sampling is 4 mas, equivalent to the diffraction limit of the ELT (Thatte et al., 2014).

To first order, the signal-to-noise achieved by cross-correlation scales with the signal-to-noise per wavelength element of the planet's absorption lines times the square root of the number of lines in the waveband (Snellen et al., 2015). For bright stars at near-infrared wavelengths, we can assume that the noise is dominated by the photon noise of the stellar PSF, which scales with the mirror diameter D. The signal-to-noise of the planet spectral lines scales with the square root of the spectral resolving power, so the signal to noise of HARMONI compared to SINFONI can be approximated as:

$$\frac{S/N_{HARMONI}}{S/N_{SINFONI}} = \frac{D_{ELT}\sqrt{R_{HARMONI}}}{D_{VLT}\sqrt{R_{SINFONI}}} = 9.75$$

assuming the maximum spectral resolution of HARMONI, but otherwise equal wavelength coverage and instrument throughput. This indicates that HARMONI can achieve the same sensitivity as SINFONI in $\sim 1\%$ of the exposure time, but for planets that are five times closer to their host star because the diffraction pattern scales with the inverse of the mirror diameter.

With a spectral resolving power of 20,000, the systemic and orbital velocities of target planets can be resolved by the cross-correlation function. In addition to discovering a companion and spectrally characterizing its atmosphere, the HARMONI instrument can therefore be used to establish co-movement with the host star and constrain its orbit via the instantaneous radial velocity. We conceive that this can be achieved in a single observation, making HARMONI especially suitable for the characterization of young giant exoplanets.

5.6 CONCLUSION

This study introduces the first application of the molecule mapping technique for detecting close-in substellar companions using AO-assisted medium-resolution integral field spectroscopy. With molecule mapping, integral-field spectra are cross-correlated with molecular template spectra to search for the spectral signatures of spatially resolved exoplanets that are embedded in the photon noise of the dominating star light. The cross-correlation co-adds the individual absorption lines of the planet spectrum at the spatial location of the planet, while this is not the case for (residual) telluric and stellar features.

We applied molecule mapping to 2.5 hours of archival SINFONI observations of the β Pictoris system. By cross-correlating the integal-field data cubes with templates of CO, H_2O, CH_4 and NH_3, we obtained 6.9σ and 11.0σ detections of CO and H_2O in the atmosphere of the planet. We also cross-correlated with a grid of BT-Settl models, varying the effective temperature between 1200 K − 3000 K, and the surface gravity between $\log(g) = 2.5 - 5.5$. We found that the cross-correlation peaks for $T_{\rm eff} = 1700$ K and $\log(g) = 3.5$, and show that molecule mapping can therefore constrain the fundamental parameters of young gas giant planets. With these model parameters, the planet was detected at a confidence of 14.4σ, corresponding to a 3σ contrast of 4.4×10^{-5}. We also analysed the same data using the LOCI algorithm. In this case the planet was only marginally detected. This result demonstrates molecule mapping can significantly enhance the sensitivity of IFS observations at medium spectral resolution over established direct imaging techniques.

Our successful application of molecule mapping on existing SINFONI data feeds expectations for the potential of upcoming medium-resolution integral-field instruments on the JWST and the ELT. We briefly outlined the specifications of MIRI and NIRSpec (JWST) and HARMONI (ELT) and anticipate that these instruments will benefit significantly from cross-correlation based analyses. We therefore strongly advocate observations of young giant exoplanets with MIRI, NIRSpec and HARMONI.

ACKNOWLEDGEMENTS

This work is part of research programme VICI 639.043.107, funded by the Dutch Organisation for Scientific Research (NWO). Snellen acknowledges funding from the European Research Council (ERC) under the European Union's Horizon 2020 research and innovation programme under grant agreement No 694513. This work is based on observations collected at the European Organisation for Astronomical Research in the Southern Hemisphere under ESO programme 093.C-0626(A).

BIBLIOGRAPHY

Allard, F., D. Homeier, and B. Freytag (2011). „Model Atmospheres From Very Low Mass Stars to Brown Dwarfs." In: *16th Cambridge Workshop on Cool Stars, Stellar Systems, and the Sun*. Ed. by C. Johns-Krull, M. K. Browning, and A. A. West. Vol. 448. Astronomical Society of the Pacific Conference Series, p. 91. arXiv: 1011.5405 [astro-ph.SR].

Augereau, J. C. et al. (2001). „Dynamical modeling of large scale asymmetries in the beta Pictoris dust disk." In: *A&A* 370, pp. 447–455. DOI: 10.1051/0004-6361:20010199. eprint: astro-ph/0102069.

Baraffe, I. et al. (2003). „Evolutionary models for cool brown dwarfs and extrasolar giant planets. The case of HD 209458." In: *A&A* 402, pp. 701–712. DOI: 10.1051/0004-6361:20030252. eprint: astro-ph/0302293.

Barman, T. S. et al. (2015). „Simultaneous Detection of Water, Methane, and Carbon Monoxide in the Atmosphere of Exoplanet HR8799b." In: *ApJ* 804, 61, p. 61. DOI: 10.1088/0004-637X/804/1/61. arXiv: 1503.03539 [astro-ph.EP].

Bell, C. P. M., E. E. Mamajek, and T. Naylor (2015). „A self-consistent, absolute isochronal age scale for young moving groups in the solar neighbourhood." In: *MNRAS* 454, pp. 593–614. DOI: 10.1093/mnras/stv1981. arXiv: 1508.05955 [astro-ph.SR].

Beuzit, J.-L. et al. (2008). „SPHERE: a 'Planet Finder' instrument for the VLT." In: *Ground-based and Airborne Instrumentation for Astronomy II*. Vol. 7014. Proc. SPIE, p. 701418. DOI: 10.1117/12.790120.

Bonnefoy, M. et al. (2011). „High angular resolution detection of β Pictoris b at 2.18 μm." In: *A&A* 528, L15, p. L15. DOI: 10.1051/0004-6361/201016224.

Bowler, B. P. (2016). „Imaging Extrasolar Giant Planets." In: *PASP* 128.10, p. 102001. DOI: 10.1088/1538-3873/128/968/102001. arXiv: 1605.02731 [astro-ph.EP].

Burrows, A., D. Sudarsky, and I. Hubeny (2006). „L and T Dwarf Models and the L to T Transition." In: *ApJ* 640, pp. 1063–1077. DOI: 10.1086/500293. eprint: astro-ph/0509066.

Burrows, C. J. et al. (1995). „HST Observations of the Beta Pictoris Circumstellar Disk." In: *American Astronomical Society Meeting Abstracts*. Vol. 27. Bulletin of the American Astronomical Society, p. 1329.

Chauvin, G. (2016). „Direct Imaging of Exoplanets Living an Exciting Life." In: *Young Stars & Planets Near the Sun*. Ed. by J. H. Kastner, B. Stelzer, and S. A. Metchev. Vol. 314. IAU Symposium, pp. 213–219. DOI: 10.1017/S1743921315006560.

Chilcote, J. et al. (2017). „1-2.4 μm Near-IR Spectrum of the Giant Planet β Pictoris b Obtained with the Gemini Planet Imager." In: *AJ* 153, 182, p. 182. DOI: 10.3847/1538-3881/aa63e9. arXiv: 1703.00011 [astro-ph.EP].

Currie, T. et al. (2017). „Subaru/SCExAO First-light Direct Imaging of a Young Debris Disk around HD 36546." In: *ApJ* 836, L15, p. L15. DOI: 10.3847/2041-8213/836/1/L15. arXiv: 1701.02314 [astro-ph.EP].

de Kok, R. J. et al. (2014). „Identifying new opportunities for exoplanet characterisation at high spectral resolution." In: *A&A* 561, A150, A150. DOI: 10.1051/0004-6361/201322947. arXiv: 1312.3745 [astro-ph.EP].

Ducati, J. R. (2002). „VizieR Online Data Catalog: Catalogue of Stellar Photometry in Johnson's 11-color system." In: *VizieR Online Data Catalog* 2237.

Eisenhauer, F. et al. (2003). „SINFONI - Integral field spectroscopy at 50 milliarcsecond resolution with the ESO VLT." In: *Instrument Design and Performance for Optical/Infrared Ground-based Telescopes*. Ed. by M. Iye and A. F. M. Moorwood. Vol. 4841. Proc. SPIE, pp. 1548–1561. DOI: 10.1117/12.459468. eprint: astro-ph/0306191.

Fitzgerald, M. P. and J. R. Graham (2006). „Speckle Statistics in Adaptively Corrected Images." In: *ApJ* 637, pp. 541–547. DOI: 10.1086/498339. eprint: astro-ph/0510503.

Gontcharov, G. A. (2006). „Pulkovo Compilation of Radial Velocities for 35495 Hipparcos stars in a common system." In: *Astronomy Letters* 32, pp. 759–771. DOI: 10.1134/S1063773706110065. arXiv: 1606.08053 [astro-ph.SR].

Gray, R. O. et al. (2006). „Contributions to the Nearby Stars (NStars) Project: Spectroscopy of Stars Earlier than Mo within 40 pc-The Southern Sample." In: *AJ* 132, pp. 161–170. DOI: 10.1086/504637. eprint: astro-ph/0603770.

Guyon, O. (2011). „High performance coronagraphy for direct imaging of exoplanets." In: *European Physical Journal Web of Conferences*. Vol. 16. European Physical Journal Web of Conferences, p. 03001. DOI: 10.1051/epjconf/20111603001.

Heng, K. and J. R. Lyons (2016a). „Carbon Dioxide in Exoplanetary Atmospheres: Rarely Dominant Compared to Carbon Monoxide and Water in Hot, Hydrogen-dominated Atmospheres." In: *ApJ* 817, 149, p. 149. DOI: 10.3847/0004-637X/817/2/149. arXiv: 1507.01944 [astro-ph.EP].

Heng, K. and S.-M. Tsai (2016b). „Analytical Models of Exoplanetary Atmospheres. III. Gaseous C-H-O-N Chemistry with Nine Molecules." In: *ApJ* 829, 104, p. 104. DOI: 10.3847/0004-637X/829/2/104. arXiv: 1603.05418 [astro-ph.EP].

Hubeny, I. and A. Burrows (2007). „A Systematic Study of Departures from Chemical Equilibrium in the Atmospheres of Substellar Mass Objects." In: *ApJ* 669, pp. 1248–1261. DOI: 10.1086/522107. arXiv: 0705.3922.

Husser, T.-O. et al. (2013). „A new extensive library of PHOENIX stellar atmospheres and synthetic spectra." In: *A&A* 553, A6, A6. DOI: 10.1051/0004-6361/201219058. arXiv: 1303.5632 [astro-ph.SR].

Jones, A. et al. (2013). „An advanced scattered moonlight model for Cerro Paranal." In: *A&A* 560, A91. DOI: 10.1051/0004-6361/201322433. URL: http://dx.doi.org/10.1051/0004-6361/201322433.

Jovanovic, N. et al. (2015). „The Subaru Coronagraphic Extreme Adaptive Optics System: Enabling High-Contrast Imaging on Solar-System Scales." In: *PASP* 127, p. 890. DOI: 10.1086/682989. arXiv: 1507.00017 [astro-ph.IM].

Kawahara, H. et al. (2014). „Spectroscopic Coronagraphy for Planetary Radial Velocimetry of Exoplanets." In: *ApJ* 212, 27, p. 27. DOI: 10.1088/0067-0049/212/2/27. arXiv: 1404.5712 [astro-ph.EP].

Kenworthy, M. (2017). „Looking for rings and things." In: *Nature Astronomy* 1, 0099, p. 0099. DOI: 10.1038/s41550-017-0099.

Konopacky, Q. M. et al. (2013). „Detection of Carbon Monoxide and Water Absorption Lines in an Exoplanet Atmosphere." In: *Science* 339, pp. 1398–1401. DOI: 10.1126/science.1232003. arXiv: 1303.3280 [astro-ph.EP].

Lafrenière, D. et al. (2007). „A New Algorithm for Point-Spread Function Subtraction in High-Contrast Imaging: A Demonstration with Angular Differential Imaging." In: *ApJ* 660, pp. 770–780. DOI: 10.1086/513180. eprint: astro-ph/0702697.

Lagrange, A.-M. et al. (2009). „A probable giant planet imaged in the β Pictoris disk. VLT/NaCo deep L'-band imaging." In: *A&A* 493, pp. L21–L25. DOI: 10.1051/0004-6361:200811325. arXiv: 0811.3583.

Lagrange, A.-M. et al. (2010). „A Giant Planet Imaged in the Disk of the Young Star β Pictoris." In: *Science* 329, p. 57. DOI: 10.1126/science.1187187. arXiv: 1006.3314 [astro-ph.EP].

Lazzaro, D. et al. (1994). „Is there a planet around beta Pictoris? Perturbations of a planet circumstellar dust disk. 2: The analytical model." In: *Icarus* 108, pp. 59–80. DOI: 10.1006/icar.1994.1041.

Lecavelier des Etangs, A. and A. Vidal-Madjar (2016). „The orbit of beta Pictoris b as a transiting planet." In: *A&A* 588, A60, A60. DOI: 10.1051/0004-6361/201527631. arXiv: 1602.04683 [astro-ph.EP].

Lecavelier des Etangs, A. et al. (1996). „Perturbations of a Planet on the β Pictoris Circumstellar Dust Disk. 3. Time Scale of Collisional Destruction versus Resonance Time Scale." In: *Icarus* 123, pp. 168–179. DOI: 10.1006/icar.1996.0147.

Luger, R. et al. (2017). „The Pale Green Dot: A Method to Characterize Proxima Centauri b Using Exo-Aurorae." In: *ApJ* 837, 63, p. 63. DOI: 10.3847/1538-4357/aa6040. arXiv: 1609.09075 [astro-ph.EP].

Macintosh, B. et al. (2006). „The Gemini Planet Imager." In: *Society of Photo-Optical Instrumentation Engineers (SPIE) Conference Series*. Vol. 6272. Proc. SPIE, p. 62720L. DOI: 10.1117/12.672430.

Macintosh, B. et al. (2014). „First light of the Gemini Planet Imager." In: *Proceedings of the National Academy of Science* 111, pp. 12661–12666. DOI: 10.1073/pnas.1304215111. arXiv: 1403.7520 [astro-ph.EP].

Marois, C. et al. (2008). „Direct Imaging of Multiple Planets Orbiting the Star HR 8799." In: *Science* 322, p. 1348. DOI: 10.1126/science.1166585. arXiv: 0811.2606.

Mawet, D. et al. (2012). „Review of small-angle coronagraphic techniques in the wake of ground-based second-generation adaptive optics systems." In: *Space Telescopes and Instrumentation 2012: Optical, Infrared, and Millimeter Wave*. Vol. 8442. Proc. SPIE, p. 844204. DOI: 10.1117/12.927245. arXiv: 1207.5481 [astro-ph.IM].

Mesa, D. et al. (2017). „Upper limits for mass and radius of objects around Proxima Cen from SPHERE/VLT." In: *MNRAS* 466, pp. L118–L122. DOI: 10.1093/mnrasl/slw241. arXiv: 1611.10362 [astro-ph.EP].

Moses, J. I. et al. (2016). „On the Composition of Young, Directly Imaged Giant Planets." In: *ApJ* 829, 66, p. 66. DOI: 10.3847/0004-637X/829/2/66. arXiv: 1608.08643 [astro-ph.EP].

Mouillet, D. et al. (1997). „A planet on an inclined orbit as an explanation of the warp in the Beta Pictoris disc." In: *MNRAS* 292, p. 896. DOI: 10.1093/mnras/292.4.896. eprint: astro-ph/9705100.

Noll, S. et al. (2012). „An atmospheric radiation model for Cerro Paranal." In: *A&A* 543, A92. DOI: 10.1051/0004-6361/201219040. URL: http://dx.doi.org/10.1051/0004-6361/201219040.

Rameau, J. et al. (2015). „Detection limits with spectral differential imaging data." In: *A&A* 581, A80, A80. DOI: 10.1051/0004-6361/201525879.

Riaud, P. and J. Schneider (2007). „Improving Earth-like planets' detection with an ELT: the differential radial velocity experiment." In: *A&A* 469, pp. 355–361. DOI: 10.1051/0004-6361:20077085.

Roques, F. et al. (1994). „Is there a planet around beta Pictoris? Perturbations of a planet on a circumstellar dust disk. 1: The numerical model." In: *Icarus* 108, pp. 37–58. DOI: 10.1006/icar.1994.1040.

Royer, F., J. Zorec, and A. E. Gómez (2007). „Rotational velocities of A-type stars. III. Velocity distributions." In: *A&A* 463, pp. 671–682. DOI: 10.1051/0004-6361:20065224. eprint: astro-ph/0610785.

Ruffio, J.-B. et al. (2017). „Improving and Assessing Planet Sensitivity of the GPI Exoplanet Survey with a Forward Model Matched Filter." In: *ApJ* 842, 14, p. 14. DOI: 10.3847/1538-4357/aa72dd. arXiv: 1705.05477 [astro-ph.EP].

Scholl, H., F. Roques, and B. Sicardy (1993). „Resonance trapping of circumstellar dust particles by an alleged planet." In: *Celestial Mechanics and Dynamical Astronomy* 56, pp. 381–393. DOI: 10.1007/BF00699748.

Smith, Bradford A. and Richard J. Terrile (1984). „A Circumstellar Disk Around β Pictoris." In: *Science* 226.4681, pp. 1421–1424. ISSN: 0036-8075. DOI: 10.

1126/science.226.4681.1421. eprint: http://science.sciencemag.org/content/226/4681/1421.full.pdf. URL: http://science.sciencemag.org/content/226/4681/1421.

Snellen, I. A. G. et al. (2014). „Fast spin of the young extrasolar planet β Pictoris b." In: *Nature* 509, pp. 63–65. DOI: 10.1038/nature13253.

Snellen, I. et al. (2015). „Combining high-dispersion spectroscopy with high contrast imaging: Probing rocky planets around our nearest neighbors." In: *A&A* 576, A59, A59. DOI: 10.1051/0004-6361/201425018. arXiv: 1503.01136 [astro-ph.EP].

Sparks, W. B. and H. C. Ford (2002). „Imaging Spectroscopy for Extrasolar Planet Detection." In: *ApJ* 578, pp. 543–564. DOI: 10.1086/342401. eprint: astro-ph/0209078.

Thatte, N. A. et al. (2014). „HARMONI: the first light integral field spectrograph for the E-ELT." In: *Ground-based and Airborne Instrumentation for Astronomy V*. Vol. 9147. Proc. SPIE, p. 914725. DOI: 10.1117/12.2055436.

Todorov, K. O. et al. (2016). „The Water Abundance of the Directly Imaged Substellar Companion κ And b Retrieved from a Near Infrared Spectrum." In: *ApJ* 823, 14, p. 14. DOI: 10.3847/0004-637X/823/1/14. arXiv: 1504.00217 [astro-ph.EP].

van Leeuwen, F. (2007). „Validation of the new Hipparcos reduction." In: *A&A* 474, pp. 653–664. DOI: 10.1051/0004-6361:20078357. arXiv: 0708.1752.

Wang, J. J. et al. (2016). „The Orbit and Transit Prospects for β Pictoris b Constrained with One Milliarcsecond Astrometry." In: *AJ* 152, 97, p. 97. DOI: 10.3847/0004-6256/152/4/97. arXiv: 1607.05272 [astro-ph.EP].

Wang, J. et al. (2017). „Observing Exoplanets with High Dispersion Coronagraphy. I. The Scientific Potential of Current and Next-generation Large Ground and Space Telescopes." In: *AJ* 153, 183, p. 183. DOI: 10.3847/1538-3881/aa6474. arXiv: 1703.00582 [astro-ph.EP].

Zahnle, K. J. and M. S. Marley (2014). „Methane, Carbon Monoxide, and Ammonia in Brown Dwarfs and Self-Luminous Giant Planets." In: *ApJ* 797, 41, p. 41. DOI: 10.1088/0004-637X/797/1/41. arXiv: 1408.6283 [astro-ph.EP].

NEDERLANDSE SAMENVATTING

HET BESTAAN VAN EXOPLANETEN

Het zonnestelsel herbergt acht planeten, waarvan er vier rotsachtig zijn die zich in de binnenste delen van het zonnestelsel bevinden, en vier grotere planeten bestaande uit voornamelijk gas en ijs, verder weg van de Zon. Speculaties over het bestaan van soortgelijke planetenselsels rond andere sterren worden al vele honderden jaren gedaan, al ver voor het tijdperk van de moderne sterrenkunde. Het heeft echter tot 1995 geduurd voordat de eerste zogeheten *exoplaneet* daadwerkelijk werd ontdekt. Deze planeet draait rond de ster 51 Pegasi, een met het blote oog nauwelijks waarneembare ster in het sterrenbeeld Pegasus. 51 Pegasi b bleek een gasreus te zijn in een zeer korte baan om zijn ster, op een afstand die 20 keer kleiner is dan de afstand tussen de Aarde en de Zon. Op deze geringe afstand tot de ster ontvangt de planeet extreme hoeveelheden sterlicht, waardoor de temperatuur oploopt tot meer dan 1000 graden Celcius. Een dergelijke planeet komt in ons eigen zonnestelsel niet voor, en dus kwam de ontdekking van deze zgn. *hete Jupiter* erg onverwacht. In de jaren na 1995 werden al snel meerdere van dit soort planeten ontdekt, en de vraag rees of de configuratie van ons zonnestelsel (met rotsachtige planeten dichtbij de zon en gasreuzen verder weg) misschien eerder uitzondering dan regel is. De theorieën over de vorming van ons zonnestelsel waren evenmin toereikend om het bestaan van dit type planeet te verklaren, en er moest naar nieuwe mechanismen voor planeetvorming worden gezocht. Zodoende had de ontdekking van 51 Pegasi b onmiddelijk een enorme wetenschappelijke impact.

RADIËLE SNELHEDEN EN TRANSITS

Exoplaneten zijn moeilijk waar te nemen omdat ze veelal te dicht bij hun moederster staan om ze direct te kunnen onderscheiden, daar de ster vele malen meer licht uitzendt dan de planeet. Het grootste deel van de tot nu toe bekende exoplaneten zijn daarom ontdekt door hun indirecte effecten op het licht van de ster.

Doordat de planeet en de ster zwaartekracht op elkaar uitoefenen draaien beiden om het gemeenschappelijke zwaartepunt. Hierdoor beweegt de ster periodiek heen en weer, en de radiële component van deze beweging (langs de kijklijn zoals gezien vanaf de Aarde) is te meten via het Doppler effect in het spectrum van de ster. Omdat dit effect wordt veroorzaakt door de

zwaartekracht, is het groter voor planeten die zwaar zijn en dicht bij hun ster staan. Bovendien kunnen de massa en de baan van de planeet worden afgeleid.

In een klein deel van de gevallen ligt de kijklijn vanaf Aarde precies in het baanvlak van de planeet. Vanaf Aarde gezien gaat zo'n planeet eens per omwenteling (dus eens per exoplaneet-jaar) voor de moederster langs. Wanneer dit gebeurt blokkeert deze een deel van het sterlicht, waardoor de ster een fractie minder helder lijkt te worden. Dit effect heet een planeetovergang ofwel *transit*, en komt eens per omwenteling voor.

Evenals de radiële snelheidsmethode is ook de transitmethode vooral gevoelig voor grote planeten die dicht bij hun ster staan. Een grote planeet zorgt namelijk voor een groter helderheidsverschil, en wanneer hij dichtbij staat komt de transit vaker voor, waardoor deze makkelijker te herkennen is. Bovendien is de kans dat het baanvlak precies gunstig ligt hoger als de planeet dicht bij de ster staat. De kans dat de baan van een willekeurig gekozen hete Jupiter voor de ster langs gaat kan oplopen tot $\sim$ 10%, terwijl dit voor een planeet zoals de Aarde minder dan 0.5% is. Door deze selectie-effecten is het niet verwonderlijk dat hete Jupiters de eerste exoplaneten zijn die met deze methoden zijn gevonden.

DE POPULATIE VAN EXOPLANETEN

Sinds de ontdekking van de eerste hete Jupiters zijn er middels beide detectiemethoden meer dan 3000 exoplaneten ontdekt. Veel van deze planeten zijn kleiner en koeler dan hete Jupiters. Hierdoor is duidelijk geworden dat hete Jupiters relatief zeldzame planeten zijn en dat de populatie van exoplaneten erg divers is. Ook blijkt uit de statistiek dat een groot deel van de sterren een planetenstelsel herbergt, en dat de configuratie van ons eigen zonnestelsel niet per sé bijzonder, noch typisch is. Dit doet vermoeden dat er vele planeten bestaan die lijken op de Aarde: Rotsachtige planeten met een atmosfeer waarin leven mogelijkerwijs kan bestaan. Aard-achtige planeten zijn relatief klein en koel, en zijn daardoor nog moeilijker waar te nemen dan de veel zwaardere hete Jupiters. De zoektocht naar dit soort planeten is daarom in volle gang, en er worden regelmatig veelbelovende kandidaten gevonden. Zo is er in augustus 2016 middels de radiële snelheidsmethode een rots-achtige planeet gevonden rond de ster Proxima Centauri b. Deze ster staat van alle sterren het dichst bij ons zonnestelsel, en de planeet draait op een zodanige afstand dat de temperatuur waarschijnlijk laag genoeg is voor het bestaan van vloeibaar water op het planeetoppervlak. Vloeibaar water wordt als een van de belangrijkste voorwaarden voor biologische processen beschouwd, en het gebied rond de ster waarin de temperatuur zodanig is dat water in vloeibare vorm kan bestaan wordt aangeduid als de *leefbare zone*. De vondst van

een planeet in de leefbare zone rond de dichstbijzijnde ster was terecht wereldnieuws.

Niet veel later, in februari 2017 werd het TRAPPIST-1 systeem ontdekt, vernoemd naar het Belgische instrument waarmee deze is via de transit methode ontdekt. Dit systeem herbergt minstens zeven planeten, waarvan er tenminste drie in de leefbare zone om hun ster draaien. Naar verwachting worden er in de nabije toekomst meerdere nieuwe instrumenten opgeleverd ten behoeve van nog gevoeligere transit en radiële snelheids surveys, en zodoende zullen er in de toekomst waarschijnlijk nog veel meer van dit soort Aard-achtige planeten worden gevonden.

SPECTROSCOPISCHE KARAKTERISATIE

Om vast te stellen of een Aard-achtige planeet daadwerkelijk leefbaar is, moeten fundamentele eigenschappen van de atmosfeer zoals de temperatuur, de chemische samenstelling en dynamica nauwkeurig worden gemeten. Dit is mogelijk door het sterlicht wat op de planeet valt (of het licht wat de planeet intrinsiek uitzendt) te analyseren met behulp van een spectrograaf: De temperatuur is af te leiden uit de verdeling van straling op korte en langere golflengtes (een koele planeet straalt relatief meer rood licht uit dan blauw). Afhankelijk van de chemische samenstelling zal het spectrum van de planeet op bepaalde golflengtes straling absorberen of uitzenden. Dit vormt een patroon van absorptie (c.q. emissie) lijnen wat uniek is voor elk atoom en molecuul. Atmosferische dynamica is in beginsel te meten m.b.v. het Doppler effect, daar het gas in de atmosfeer op verschillende plekken een andere radiële snelheid kan hebben.

Een dergelijke analyse is ook van toepassing op sterren, en wordt al ± 100 jaar succesvol toegepast. Hierdoor is het relatief eenvoudig om de eigenschappen van een ster nauwkeurig te bepalen, maar voor een exoplaneet is dit veel moeilijker omdat het licht van de planeet vele malen zwakker is dan de ster en doordat fysische processen in planeetatmosferen doorgaans minder bekend zijn dan die in sterren. Om deze reden worden er steeds grotere en geavanceerdere telescopen en instrumenten gebouwd, en worden er steeds uitgebreidere en precieze modellen ontwikkeld waarmee de atmosferen van planeten kunnen worden gesimuleerd.

HOGE RESOLUTIE SPECTROSCOPIE VANAF DE GROND

Het meten van het spectrum van een exoplaneet wordt niet alleen bemoeilijkt door het overheersende sterlicht, maar ook door instabiliteit van de instrumentatie en de effecten van de Aard-atmosfeer, welke zich tussen de telescoop op de grond en het exoplaneetsysteem bevindt. Om aan dit soort

instabiliteit te ontkomen wordt voor de spectroscopische karakterisatie van exoplaneten veelal gebruik gemaakt van ruimte telescopen, met name de Hubble en Spitzer telescopen. Het nadeel van een spectrograaf aan boord van een ruimte-telescoop is dat deze over het algemeen een relatief lage spectrale resolutie heeft. Dat wil zeggen dat het instrument niet in staat is om absorptielijnen van elkaar te onderscheiden als deze bijna dezelfde golflengte hebben. Een instrument met hoge spectrale resolutie kan individuele absorptielijnen wel van elkaar onderscheiden, maar is groter en zwaarder en daarom duurder om in de ruimte te plaatsen.

In de exoplaneet groep in Leiden is een techniek ontwikkeld die gebruik maakt van de hoge resolutie van dit soort spectrografen om de spectraallijnen van een planeet te onderscheiden van die van de ster en de Aard-atmosfeer. Door de hoge spectrale resolutie is de spectrograaf namelijk gevoelig voor het Doppler effect als gevolg van de baansnelheid van de planeet. De radiële component van de planeet verandert terwijl de planeet zijn baan aflegt, en als de baan van de planeet bekend is, is precies uit te rekenen wat de radiële snelheid van de planeet op elk tijdstip is. Deze snelheidsvariatie is uniek voor de planeet, en zorgt ervoor dat de zwakke planeetlijnen van de veel helderdere sterlijnen en de Aardse atmosfeer te onderscheiden zijn.

DIT PROEFSCHRIFT

Met de huidige telescopen en instrumenten zijn we nog niet in staat om Aardachtige planeten spectroscopisch te karakteriseren, aangezien het signaal van deze planeten te zwak is. Deze techniek is daarom voornamelijk succesvol toegepast met infra-rood spectrografen en absorptielijnen van CO en water moleculen in de atmosferen van hete Jupiters. Hete Jupiters zijn groot en warm, waardoor deze signalen relatief sterk zijn en karakterisatie makkelijker is. Het tweede hoofdstuk van dit proefschrift beschrijft hoe deze techniek ook op visuele golflengtes kan worden toegepast, alwaar de absorptiespectra van hete Jupiters naar verwachting vele duizenden lijnen van gasvormig titanium en vanadium-oxide bevatten. Deze moleculen absorberen sterlicht efficient in het visuele deel van het spectrum en kunnen daarmee een belangrijke bron van energie zijn die de atmosfeer van de planeet op bepaalde plekken sterk verhit. Deze gassen kunnen daarom een belangrijke rol spelen in het klimaat van de planeet. Waarnemingen op lage spectrale resolutie suggereren dat TiO en VO daadwerkelijk in sommige hete Jupiters aanwezig zijn, maar zijn vaak niet in staat om deze moleculen eenduidig te identificeren omdat de individuele absorptielijnen niet kunnen worden opgelost. Op hogere spectrale resolutie is het wel mogelijk om het unieke absorptiepatroon van deze moleculen op te lossen, en in dit hoofdstuk tonen wij aan dat transit waarnemingen op hoge resolutie erg gevoelig zijn voor lage concentraties TiO en VO

in hete Jupiters. Echter, om de absorptielijnen te kunnen identificeren is een nauwkeurige blauwdruk nodig van de absorptiespectra van deze moleculen. Wij tonen aan dat de gangbare model spectra niet overeenkomen met TiO en VO absorptie in de atmosferen van koele sterren (welke veel TiO en VO bevatten), waardoor tot op heden niet vast te stellen is of de absorptielijnen van deze moleculen in de transit spectra van hete Jupiters voorkomen, en we concluderen dat de TiO en VO spectra nauwkeurig gemeten of berekend moeten worden voordat dit soort moleculen in de atmosferen van exoplaneten met behulp van hoge resolutie spectroscopie gevonden kunnen worden.

In hoofdstuk 3 passen we dezelfde techniek toe, maar ditmaal om het optische gereflecteerde licht van de hete Jupiter τ Boötis b te detecteren. Het licht wat direct door een planeet wordt gereflecteerd bevat waardevolle informatie over de reflectieve eigenschappen van de planeet. Zo laat het bijvoorbeeld zien of de planeet bedekt is door een reflectief wolkendek, of dat de atmosfeer helder is, in welk geval de planeet donkerder is. Deze planeet werd al in 1997 ontdekt rond de heldere ster τ Boötis. Doordat dit systeem zo helder is, zijn er in de loop der jaren meerdere pogingen gedaan om het sterlicht wat door deze planeet gereflecteerd wordt waar te nemen, maar zonder succes. In dit hoofdstuk combineren we meer dan 2100 hoge-resolutie spectra van dit systeem die tussen 1998 en 2013 met verschillende telescopen en instrumenten zijn waargenomen. Zelfs met deze hoeveelheid data blijkt het niet mogelijk om het gereflecteerde licht van de τ Boötis b waar te nemen, hetgeen betekent dat de planeet donker is, en geen reflecterend wolkendek heeft. In dit opzicht komt τ Bootis b overeen met andere hete Jupiters, welke typisch weinig reflectief zijn. Dit is echter gebaseerd op langdurige waarnemingen van de fase-veranderingen van deze planeten met behulp van ruimte-telescopen. Door ruim 2100 hoge resolutiespectra van Aardse telescopen te combineren, zijn wij in staat om soortgelijke limieten te halen.

In hoofdstuk 4 verschuiven we onze aandacht naar de Aarde. De Aarde is voor zover bekend de enige leefbare, en levende planeet. Daarom is de zoektocht naar leefbare exoplaneten gericht op planeten die "Aard-achtig" zijn. Maar om vast te stellen of een planeet daadwerkelijk op de Aarde lijkt is het allereerst noodzakelijk om te weten hoe de Aarde er uit zou zien als het een exoplaneet was geweest. Hiertoe zijn Aard-observaties vanuit de ruimte nodig. In de context van klimaatwetenschap en meteorologie wordt de Aarde continu door satellieten van buitenaf geobserveerd, maar deze stallieten staan relatief dicht bij de Aarde en nemen de Aarde in detail waar. Het is lastig om hieruit de globale eigenschappen van de Aarde af te leiden, en daarom zijn observaties vanaf grotere afstand noodzakelijk. Hoofdstuk 4 presenteert daarom een prototype voor LOUPE, wat staat voor *Lunar Observatory for Unresolved Polarimetry of Earth* (Onopgeloste, d.w.z. globale polarimetrische Aard-observaties vanaf het oppervlak van de Maan). Dit apparaat meet zowel de lichtintensiteit als de polarisatie als functie van golflengte, en

karakteriseert zodoende het polarisatiespectrum van de Aarde. Polarisatiemetingen van exoplaneten zijn op dit moment nog niet mogelijk, maar zullen in de toekomst belangrijk zijn om de oppervlakte eigenschappen van exoplaneten vast te stellen. Zo heeft verstrooiing van zonlicht door waterdruppeltjes unieke polarisatie-eigenschappen, waardoor polarisatiespectra van exoplaneten in de toekomst van groot belang zullen zijn in de zoektocht naar leefbare planeten. In dit hoofdstuk tonen we aan dat LOUPE zodanig klein en licht kan zijn dat het mogelijk is om aan bestaande maanmissies toe te voegen, zonder een grote impact op het budget of de complexiteit van een dergelijke missie.

In hoofdstuk 5 combineren we de spectroscopische methoden uit hoofdstukken 2 en 3 met hoge-contrast waarnemingen van β Pictoris b, genomen met behulp van de SINFONI spectrogaaf. β Pictoris b staat, evenals sommige andere exoplaneten namelijk zo ver van zijn ster af dat hij direct waarneembaar is in ruimtelijke afbeeldingen van het systeem, vlak naast de veel helderdere moederster. Omdat dit soort planeten ver van hun ster verwijderd zijn ontvangen ze weinig sterlicht en bevinden ze zich in een zeer koude omgeving. Deze planeten zijn echter zichtbaar omdat ze relatief kort geleden gevormd zijn. Een planeet verzamelt tijdens zijn vorming gas en stof uit de protoplanetaire schijf die om de jonge ster heen draait, en kan hierbij temperaturen van meer dan 1000 graden Celcius bereiken. Wanneer de ster volgroeid is en de schijf van gas en stof is verdwenen, gloeit een jonge planeet nog gedurende miljoenen jaren na. Dit schijnsel zorgt ervoor dat jonge planeten direct waarneembaar zijn ondanks dat ze ver van hun ster verwijderd zijn. β Pictoris b is zo'n jonge planeet, met een geschatte leeftijd van 24 miljoen jaar. Naast β Pictoris b zijn er maar enkele soortgelijke jonge exoplaneten bekend, en om ook planeten dichterbij de ster te kunnen waarnemen moeten instrumenten in staat zijn om diepere contrasten te bereiken. De SINFONI spectrograaf is in staat om tegelijkertijd ruimtelijke en spectrale informatie waar te nemen. Op deze spectrale dimensie kunnen de technieken uit hoofdstukken 2 en 3 worden toegepast, om zo het contrast tussen de ster en de planeet te verhogen. Hierdoor zijn we in staat om water en CO waar te nemen in de atmosfeer van deze planeet en stellen we vast dat toekomstige instrumenten die evenals SINFONI zowel ruimtelijke als spectrale informatie waarnemen en op dit moment in ontwikkeling zijn, uitermate goed in staat zijn om middels deze methoden jonge gasplaneten te vinden en de karakteriseren.

LIST OF PUBLICATIONS

REFEREED PUBLICATIONS

1. **Hoeijmakers, H. J.**; de Kok, R. J.; Snellen, I. A. G.; Brogi, M.; Birkby, J. L.; Schwarz, H. *A search for TiO in the optical high-resolution transmission spectrum of HD 209458b: Hindrance due to inaccuracies in the line database.* A&A, 575A, 20H (2015)

2. Ridden-Harper, A. R.; Snellen, I. A. G.; Keller, C. U.; de Kok, R. J.; Di Gloria, E.; **Hoeijmakers, H. J.**; Brogi, M.; Fridlund, M.; Vermeersen, B. L. A.; van Westrenen, W. *Search for an exosphere in sodium and calcium in the transmission spectrum of exoplanet 55 Cancri e.* A&A, 593A, 129R (2016)

3. **Hoeijmakers, H.J.**; Arts, M. L. J.; Snik, F.; Keller, C. U.; Stam, D. M.; Kuiper, J. M. *Design Trade-Off and Proof of Concept for LOUPE, the Lunar Observatory for Unresolved Polarimetry of Earth.* Optics Express, 24, 21435-21453 (2016)

4. Khalafinejad, S.; von Essen, C.; **Hoeijmakers, H. J.**; Zhou, G.; Klocová, T.; Schmitt, J. H. M. M.; Dreizler, S.; Lopez-Morales, M.; Husser, T.-O.; Schmidt, T. O. B.; Collet, R. *Exoplanetary atmospheric sodium revealed by orbital motion. Narrow-band transmission spectroscopy of HD 189733b with UVES.* A&A, 598A, 131K (2017)

5. **Hoeijmakers, H.J.**; Snellen, I. A. G.; van Terwisga, S. E. *Searching for reflected light from τ Boötis b with high-resolution ground-based spectroscopy: Approaching the 10^{-5} contrast barrier.* Accepted for publication in A&A (2017)

CONFERENCE PROCEEDINGS

1. **Hoeijmakers, H. J.**; Snik, F.; Stam, D. M.; Keller, C. U. *LOUPE: Spectropolarimetry of the Earth from the surface of the Moon.* European Planetary Science Congress 2014, EPSC Abstracts, Vol. 9, id. EPSC2014-574

2. Khalafinejad, S.; Hoeijmakers, H.J. *Searching for exo-planetary atmospheric sodium around the active star, HD 189733 with UVES.* IAU General Assembly, Meeting #29, id.2255364 (2015)

CURRICULUM VITAE

I was born on the 8th of July of the year 1990, in the city of Zwolle, the Netherlands. In 1992, my parents moved (me) to the rural town of Zonnemaire (which incidentally is the birthplace of Prof. Pieter Zeeman, known for winning the Nobel Prize in Physics together with Hendrik Lorentz in 1902 for his discovery of spectral line splitting in the presence of a magnetic field), where I attended elementary school. Growing up in the 1990's, I witnessed the development of new technologies such as personal computing, the internet and mobile communication which have fundamentally altered society. This also was a decade of discovery in astronomy and planetary science, which saw the continued robotic exploration of Mars, the thriving of the Hubble Space Telescope as well as the discovery of the first extra-solar planets. I remember being captivated by the promise of the Cassini/Huygens mission that was scheduled to arrive at Saturn in 2004. At the time of writing, this spacecraft is making its final plunge into Saturn's atmosphere, ending thirteen years of ground breaking discoveries that include the striking resemblance of Titan's cryogenic climate to the climate of Earth and the exciting potential for extraterrestrial life in warm water oceans below the frozen surface of Enceladus. Being at the receiving end of all this exciting progress, I attended high school at the Pontes Pieter Zeeman College where my interest in physics and astronomy was finally cemented.

In September 2008 I enrolled to the bachelor programme of astronomy at Leiden University, which I completed in 2011. During this time I became a member of the Rino foundation, who performs classroom physics demonstrations at high schools throughout the Netherlands. I was a member of the board for one year and performed demonstrations at over 40 schools. I continued my education by starting the instrumentation track of the astronomy master programme in 2011. This included regular visits to the Technical University of Delft where I attended courses related to planetary science, image analysis, signal processing and optics. I did both my research projects in Leiden, starting with the application of the cross-correlation technique at optical wavelengths to search for molecules in the atmosphere of a hot Jupiter in the group of Prof. dr. Ignas Snellen, followed by a project to prototype an instrument aboard a lunar lander to observe the Earth as if it were a living exoplanet, supervised by Dr. Frans Snik and Prof. dr. Christoph Keller. I graduated Cum Laude and was awarded the Huygens fellowship, allowing me to start a Ph.D. program in Leiden under the combined supervision of Dr. Frans Snik and Prof. dr. Ignas Snellen with the goal of interfacing between exoplanet observations and instrument development. During my Ph.D. I anal-

ysed optical, high-dispersion spectroscopic transit observations of two hot Jupiters to search for absorption by molecular species and reflected starlight. I developed and tested a prototype for the Lunar Observatory for Unresolved Polarimetry of Earth (LOUPE), demonstrating that spectropolarimatric characterization of Earth as a living exoplanet can be performed using a small, robust instrument from the lunar surface. Finally, I applied the new Molecule Mapping technique on integral-field spectroscopy observations of the β Pictoris system by the SINFONI spectrograph and showed that high-contrast integral field spectroscopy can be used at medium spectral resolution to confidently detect molecules in hot young gas giants and that it can be used to constrain their fundamental parameters.

As of November 2017 I will be working as a post-doctoral researcher in the groups of David Ehrenreich, Christophe Lovis and Kevin Heng at the University of Geneva and the University of Bern, Switzerland. I will continue to use spectroscopic observations to characterize exoplanets, and make use of the many new and exciting instruments that are due to be deployed over the course of the coming years.

ACKNOWLEDGEMENTS

A Ph.D. thesis is the direct result of multiple years of hard work, in which the way forward is often unclear, the lessons that need to be learned are abstract and ill defined, and the rewards of which are uncertain. The ability to do a Ph.D. depends on many more years of preparation during which you need to gather enough knowledge, evolve your understanding, acquire inspiration and most of all cultivate your motivation. It is therefore highly contingent on the people around you, and I would like to thank everyone who has contributed in making this possible.

In the first place I would like to thank my colleagues: Andrew, Emanuele, Geert-Jan, Henriette, Jayne, Javi, Matteo, Remco, Sara, Sebastiaan and so many others (exoplanets is a growing field) with whom I had the pleasure to work together. I have seen all of you face up to the realities of academic life in your own ways and circumstances and I have drawn a lot of inspiration from all of you. Thanks for the productive, collaborative and inspiring times together, and I wish you the best of success in all your works.

Ricardo, Vincent and Steven, I have greatly enjoyed our contribution to the demise of so many bachelor students while TAing the planetary systems course (remember that double FOR-loop?). Thanks for a great time and especially for teaching me a thing or two about Python.

Emanuele, thanks for the often hilarious times we had together. Your departure from 434 caused a steep decline in the gezelligheid of our office (but also its messy-ness, everyone knows that I keep my desk absolutely spotless). I wish you the best of luck in your new career and I am sure that you will do great stuff. At least you will drive a larger car than what Andy and I will drive, combined. Be sure to lock it well.

Sara, we go way back and you have been one of my closest friends even though we have done our Ph.D.'s in different countries. Thanks for inviting me to your wedding and for making me part of your family. During these years you have experienced the sometimes chilling realities of national borders and life abroad. The meanings of privilege and belonging become clear only when they are absent, but I have always seen you beat back and succeed where others don't. I wish you and your family all the happiness, wisdom, health and success, and I hope that we will get the opportunity to work together more in the future.

Paula, you have been able to withstand a lot of adversity over the past years and arguably you are the most motivated person I know. Now after facing up to pretty much every form of barrier a student can be faced with, I am so happy to see that you are approaching the level of productivity that you have

been striving for. I'd like to thank you for the many reflective conversations that we have had and for being a great friend during this entire process. I hope that your success will take flight and bring you where you want to go.

Ainil, thank you for the great literary input that you have given me over the years. I hope that we can continue our literary exchanges so please remember to keep an eye on your pigeon hole on occasion. I wish you the best of luck with the final stages of your Ph.D., and also a lot of joy with Tofan and Faiz. Both Faiz and you two are totally awesome, so I am confident that this should not be a problem.

Nazreen, we met by chance when organising a dinner party. I am so grateful that this was a success, but sad that circumstances prevented us from doing more. I have always enjoyed our Wednesday teas, dinners and the lectures that we attended together. I wish you and Tahar the best of health, wisdom and peace in your marriage; you deserve no less. Do try to finish your thesis. If you can stand by your work and shed a little light on an age-old enigma, however little, it will be rewarded in the end.

Fadwa, thanks for the many LUMC meet-ups and for introducing me to a lot of great Sudanese tastes.

My Iranian friends: Afsaneh, Behrooz, Elham, Faezeh, Yazdan, Mina, Rokhsareh, Sara and many others (and yes, also Hendrik and Thomas, you are Iranians too now, like it or not). Before meeting you I barely appreciated the international and multi-cultural environment that surrounds a university like that of Leiden. I would deeply like to thank you for your endless friendliness and hospitality and overall payeh-ness for dragging me into this amazing network and for being a part of it. Not in the least I would like to thank you for preparing me for, and hosting me during my visits to your allegedly dangerous and hostile homeland. As far as I could tell, in reality it is quite the opposite. You have a truly amazing heritage. Be sure to keep it with you whether you end up in the Netherlands (I'm totally rooting for you) or wherever else you may settle.

Thomas and Elham, I am still regularly amazed by the circumstances of how our friendship came into being. I'm sure that even Hafez would find it difficult to put into words your bravery and perseverance. Thanks for letting me be part of your adventure, not in the least the part that takes place in the kitchen. Finding Earth-like exoplanets is almost as hard as making tahchin, but I am sure that I will be successful one day, without burning down anybody's house.

In this context I would also like to mention the Damavand Fellowship. Doing a Ph.D. is a bit like climbing a mountain for the first time. You reach the summit blinded by snow and fog, only to realize that the hard part is just about to begin. Even though I spent only a short time with most of you, this adventure was exhilarating and inspiring in so many ways, and I do hope to repeat it some time.

Also thanks to my friends from Rino and beyond: Erik, Rick, Rick, Yorick (you see? that's confusing), Hiske, Inge, Jasper, Kari, Noelia, Rosa, Timmy, Willem and everyone else who has phased in and out of filmhuis over the years. Though our parting of ways and the tragic loss of our headquarters at the Hooigracht, Rijnsburgerweg and Oude Vest have somewhat decreased the frequency at which we watch movies nowadays, I have always loved our get-togethers and I hope that we can keep doing them in the future.

Erik, I distinctly recall the many late night therapy sessions that we treated ourselves to. These occasionally ended in throwing household objects through the room in agony as well as countless hours not spent on sleep. However it seems that we are each finding our respective ways, and I wish you the best of luck and happiness. I would also like to thank you for recently -after 9 years of my mockery and refusal- making clear the beauty of mathematics. Apparently it allows one to understand the meaning of complex physical equations without understanding neither the notation nor the meaning of a single variable (these things had indices and curly brackets all over the place, mind you). That was really impressive. It is indicative of your intelligence and I am pretty sure that you will turn anything in your future career into spicy, thinly sliced grilled meat.

René, a scientific career has many similarities with a career in the music industry: You always need to be passionate, you always need to search for opportunities and collaborations and you are always in the trenches, convincing people of the value of your work and relying on their willingness to help you move forward. You can struggle for years with what seems little progress, trying to achieve that big success which may never come. We have always been in a friendly competition of who of us will conquer the world first. Although this thesis is a big step forward, I can't help but feel that all bets are still off. In any case, make sure to make that début happen, as I am really looking forward to it. And if all our endeavours turn out fruitless in the end, we can still go back to building aeroplanes, or perhaps to running an orchestra in a rural town.

This brings me to the folks at Nut en Uitspanning. Ik heb vaak duidelijk gemaakt in de reservetijd te zitten, aangezien de rit van en naar Leiden aanzienlijk is en dat werkdruk alsmede sociale verplichtingen in de jaren niets dan toenemen. Desalniettemin was ik in staat om regelmatig te genieten van de repetities en onze vele optredens. Een waardevolle uitlaat voor het stadse, studenten, en academische leven. Ook jullie wens ik veel speel plezier en alle goeds toe in de toekomst.

I estimate that I have lived with over 50 housemates during my 9 years here in Leiden, and trying to name you all would result in awkward omissions, so I will not. Thanks for making Klik 23a a happy, quiet, easy-going and for the most part tidy place to live. I have always enjoyed our house as a place where interesting, diverse and nuanced ideas come together, mixed with a

healthy dose of humour, good cooking (for most of you, that is) and a lot of gezelligheid. I have none but good memories and will miss this aspect of student life dearly.

Next, I would like to thank my two promoters: Frans, many thanks for spicing up my time here with insane space-faring hyperspectral polarimetry projects. I loved the way in which we could inter(re)act promptly and flexibly under ever so exciting and ~~unpredictable~~ dynamic circumstances. If there's anything that I've learned, it's that enthusiasm and pragmatism are key to the success of any project. That's why LOUPE is not going to die any time soon, unless perhaps it actually gets to fly to the Moon.

Ignas, you did not lose patience even when I spent six full months scrolling through thousands of aperture traces in IRAF. You taught me how to look pragmatically at raw data. Without this skill, a student could spend months on a troublesome dataset without real progress, while the raw data tells you all you need to know. You spent many hours going over plots, papers, proposals and presentations and have taught me how important it is to not only do good science, but also how to present it well. Thanks for bringing me to this point, and I am very excited to carry these foundations with me to my new colleagues in Switzerland.

These pages would not be complete without thanking the countless organizations and institutions who made, and continue to make this research possible. Especially Leiden Observatory, on whose efficient management I and so many other students and researchers rely on on a daily basis. Also ESO, whose instruments, facilities and archives are at the cradle of much of this research, and the Dutch and European governments and society at large, who have created the climate and provided the financial means that are needed for fundamental research to take place. Science can only be done by a few people, while so many others are working hard to create the necessary boundary conditions. This always needs to be acknowledged.

Finally, I would dearly like to thank my parents and family for supporting me throughout my education and work in Leiden as well as before. You encouraged me to learn and work hard, and always made sure that I had the means and the space to follow my dreams. Hence you supported me even when I decided that it was a great idea to spend my life chasing rocks floating around distant stars (instead of a real job that actually has tangible use), and even if it meant that I should go to a distant country to get even better at it. We are a close family that pulls together in good times as well as in bad times when it is most important. I will miss you, but I know that you will make Switzerland feel less far away than it actually is.